Universitat Rovira i Virgili

Departament d'Història i Història de l'Art

Màster en Arqueologia del Quaternari i Evolució Humana

International Master in

QUATERNARY AND PREHISTORY

Master's Thesis:

Revisiting Ndutu

A new virtual reconstruction of the Ndutu cranium

Gustavo Daniel Montiel Hernández

Advisors:

Carlos Lorenzo Merino

Florent Détroit

Academic course 2020/2021

A Peta, Dona, mamá y papá.

Acknowledgements

Firstly, I would like to thank Donaji Catalina Alejandra Esparza Arredondo, my partner in life. Her love, encouragement, advice and motivation carried me throughout the vicissitudes of this work. *Across the distance or at my side, in the darkest moments, you were the light in my path.*

I would also like extend thanks to my parents for lovingly and patiently raising me, listening to me, feeding my curiosity and determination, and, above all, for never stopping to believe in me.

I also thank my advisors, Carlos Lorenzo Merino, Ph. D., researcher at the Institut Català de Paleoecología Humana y Evolució Social, teacher, and coordinator of the Màster en Arqueologia del Quaternari i Evolució Humana at the Universitat Rovira i Virgili, and Florent Détroit, lecturer at the Muséum National d'Histoire Naturelle and UMR *Histoire Naturelle de l'Homme Préhistorique* researcher, for their invaluable help and guidance despite the global pandemic.

Finally, I would like to express my gratitude to the entire International Master in Quaternary and Prehistory consortium for selecting me and for supporting the development of research careers in this field worldwide. This project was developed with funding of the Erasmus + programme of the European Union through an Erasmus Mundus Joint Master scholarship.

Contents

Abstract

The Ndutu cranium is a partial, fragmented fossil hominin specimen from the Upper Acheulean of the Lake Ndutu site in Tanzania. Prior to its recovery, the exemplar suffered brittle deformation. Hence, it was reconstructed in 1976 and then again in 1990 by R. Clarke, following a now outdated approach to position the disarticulated fragments of the preserved facial skeleton and left supra-orbital. As a consequence, several traits like post-orbital constriction, supra-orbital projection, facial projection, prognatism/orthognathism, and cranial flexion are uncertain. Here I propose a new virtual reconstruction of this cranium produced by executing the Digital Alignment tool developed by A. Profico in 2019 in the R statistical system. By firstly comparing the effects of the use of a sample specimen-based or consensus shape-based template, symmetrization, and use of sliding surface semi-landmarks, I determine the best strategy to perform this reconstruction. Subsequently, I describe and ponder the consequences of the chosen procedure in terms of said traits by comparing the overall shape of the specimen, alongside two alternatives, with a sample of well-preserved Pleistocene hominin crania following a geometric morphometric approach. The results of the methodological comparison reveal that performance varies by fragment. Compared to previous works, the use of a template specimen chosen from the sample to align landmark subsets of hominin crania offered unexpectedly poor results, implying that the conclusions drawn from diverse multiple genera samples cannot be extended to collections of closely related specimens. They also demonstrate that the alignment of near continuous fragments can be improved by the use of semi-landmarks but not distant complex fragment clusters. Furthermore, all alternative reconstructions (including the non-template based one) result closest to the sapient lineage. These results lend support to the notion endorsed by previous authors that the Ndutu cranium is a representative of early *Homo sapiens*. They also suggest that a morphology relatively close in shape space to that of the more recent Djebel Irhoud specimens may have been present in Tanzania *circa* 450 Ka ago.

Chapter 1

Introduction

The Ndutu cranium is a partial hominin specimen from the Lake Ndutu site in northeastern Tanzania. As a result of a troubled taphonomic history, most of the face and the cranial vault of this specimen is missing, along with the anterior part of the cranial base (Clarke, 1976). Hence it has not been possible to determine the extent of the development of its facial traits. Given this specimen's fragmentary nature, its taxonomic affinities have constituted a matter of content since the time of its discovery. This work aspires to approximate a recovery of this specimen's lost morphology by setting forth a statistically-based reconstruction hypothesis.

In particular, the purpose of this chapter is, first, to contextualize this specimen's current reconstruction. Subsequently, as a means to justify the revision of that work, I present the differing morphological and (consequently) taxonomic interpretations that have been posited by various authors, as well as their relevance in the midst of the greater debates regarding the origin of the evolutionary lineages leading to *Homo* (henceforth, *H.*) *sapiens* and *H. neanderthalensis*. Finally, I review the available techniques that make the venture of a new reconstruction a feasible task.

1.1 Archaeological and Taphonomic Context

The story of the Ndutu cranium starts in 1973, when Amini Mturi, Director of Antiquities for Tanzania investigated the stratigraphic origin of a collection of Early Stone Age artifacts and fossil fragments in the western shore of a seasonal soda lake called Lake Ndutu (Figure 1.1). Back then, the shore of this lake was littered with stone artifacts of uncertain provenance that would be exposed during the months of September to November as the water markedly retreated for the dry season. It was this time of the year when Mturi stumbled upon a fragmented hominin cranium resting alongside faunal bone fragments (Mturi, 1976).

The remains were embedded in a silty clay sub-unit in the most superficial of two archaeological horizons within a 15 to 45 cm thick greenish sandy clay unit of a claystone member (ibid.). The sandy clay unit is overlain by a re-worked tuff that has been correlated to the Norkilili Member of the Upper Masek Beds (formerly known as "Bed IV B") of Olduvai Gorge, which lays around 30 Km to the North East. This originally supposed an age of *circa* 400 Ka BP (G. P. Rightmire, 1983; Clarke, 1990) or perhaps 500 Ka BP (Bada, 1987). Yet, in 1993, P. C. Manega posited a lower age limit for the overlaying Ndutu sediments of Olduvai of 450 ± 40 Ka BP.

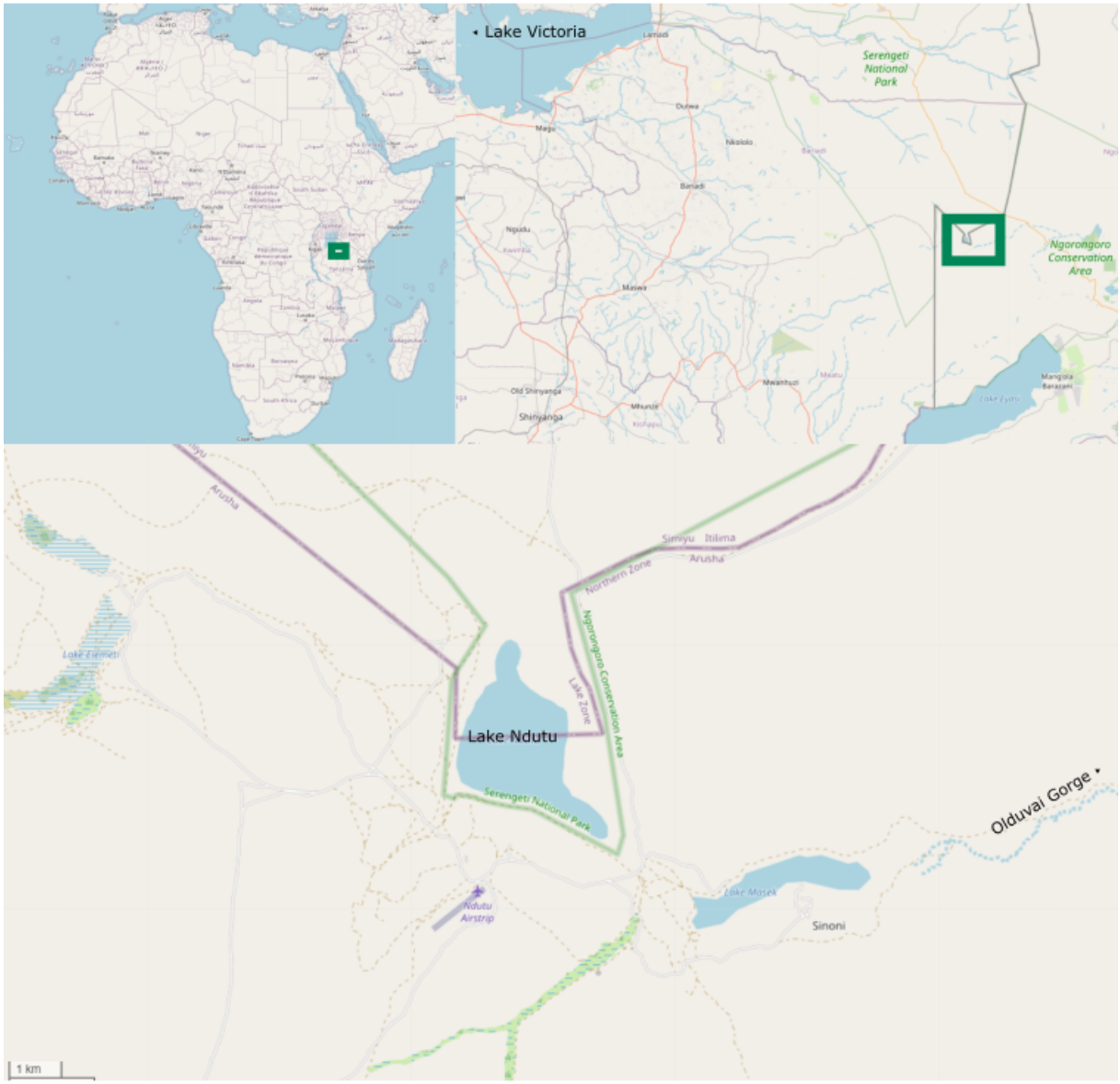

Figure 1.1: Location of Lake Ndutu. Composed from OpenStreetMap contributors, 2017.

According to Mturi, the industry associated with the Ndutu cranium was dominated by quartz and quartzite spheroids and hammerstones, but also included some flakes and cores. Yet, after a five-year period when the Ndutu lake remained flooded, the subsequently eroded stratum revealed eight quartzite handaxes. Upon typological examination of these artifacts, Mturi related them with the Upper Acheulean of the Masek Beds of Olduvai.

The sandy clay sub-unit, upon which the hominin skull laid, was labeled occupational floor No. 1; beneath it, occupational floor No. 2, consisted on largely *in-situ* lithic and faunal remains

resting upon a sand-free, green clay unit. There is a clear discomformity between both the unit bearing occupational floor No. 1. and the one over which occupational floor No. 2 is found. Several 30 cm-deep channels bearing lithic and faunal remains cut into the deeper green clay unit. Bellow this, no other remains were to be found during the 1974 excavations. Mturi's interpretation was that the hominins possibly used this location as a butchering site while hunting or camping near the shore of lake Ndutu (although he accepted that finding a hominin cranium in this context was odd). Evidence of rolling appeared to correspond to the effects of the expansion and retrieval of this shoreline across time (Mturi, 1976).

After millennia of being subject to the cycles affecting the lacustrine sediments that enclosed it, the Ndutu cranium was left heavily fragmented and deformed. Increasing sediment loads and varying humidity compromised the integrity of the remains causing what is known as taphonomic distortion. In time the cranium spent under the sediments, salt within the diplöe dissolved and recrystallized during the wet and dry periods, in many cases separating both tables of compact bone. This process left the parietals either dilated (exaggeratedly thick) or missing the inner or outer tables (Clarke, 1976).

Most of the cranium has been affected by a kind of distortion called brittle deformation. This is a common preservation artifact that occurs when the structure and arrangement of a bone is lost, provided that it has been devoid of at least part of its constituting moist and organic compounds. In brittle deformation, dry bones are broken into pieces without changing their shape, as opposed to plastic deformation, where the shape of collagen-rich bone (Di Vincenzo et al., 2017) is distorted, but the arrangement of its parts is preserved given the lack of breakage (Lautenschlager, 2016). However, it is noteworthy that a noticeable degree of plastic deformation is also evident in the anterior and lateral portion of the cranium's parietals, close to the coronal suture and the *lambda* end of the sagittal one, as well as in the central region of the right parietal (Clarke, 1990).

1.2 Previous Restorations

Upon its extraction from the site, the entire specimen was held in one piece by its surrounding matrix, which had been impregnated with a consolidant known as Bedacryl (Clarke, 1976, 1990). While still enclosed in sandy clay, it was delivered to Ronald J. Clarke at Nairobi in February 1974, where he started working on the reconstruction (Figure 1.2).

The Bedacryl was dissolved with thinner and the matrix was stripped away using a dental probe. Straightforwardly, aided by their retained approximate anatomical position, Clarke matched the fractured surfaces of the fragments to reassemble most of the preserved portions of the cranium (Clarke, 1990).

He found that plastic deformation had caused the parietals to become exaggeratedly bossed, as he later clarified in (1990). Nonetheless, he added a fair amount of plaster of Paris without correcting this distortion - this would lend support to the portions of the parietals where either of the tables of the diplöe had been lost. Considering the marked forward and outward curving of the right frontal bone fragment, he predicted the Ndutu individual might have possessed a protruding supraorbital torus, which he reconstructed by sculpting it in this same material alongside a forwardly projected face.

The facial fragments were held in place with plaster. They were preliminarily positioned considering the relation between the *crista galli* and the cribiform plate, still attached to the facial skeleton, and the preserved sphenoid, which could be seen through an opening left by

Clarke in the top of the cranial vault (Clarke, 1976). He published the result of his reconstruction along with the due morphological analysis, in Nature in 1976.

At that moment of the finding, it appeared that the only the surviving parts of the facial skeleton were the circumnasal area, the medial wall of the right orbit and the anterior part of the left maxilla. However, not too long afterwards, in August 1978, Clarke had to revisit his reconstruction. Three additional fragments had been found after sorting the faunal remains recovered in 1973 (Clarke, 1990). The fragments included the following:

- A left fronto-parietal fragment that articulated with the rest of that bone,
- An unarticulated left lateral supraorbital part of the frontal bone with a torus (as Clarke had predicted in (1976), and
- A weathered parietal fragment that did not clearly match anywhere in the calvarium.

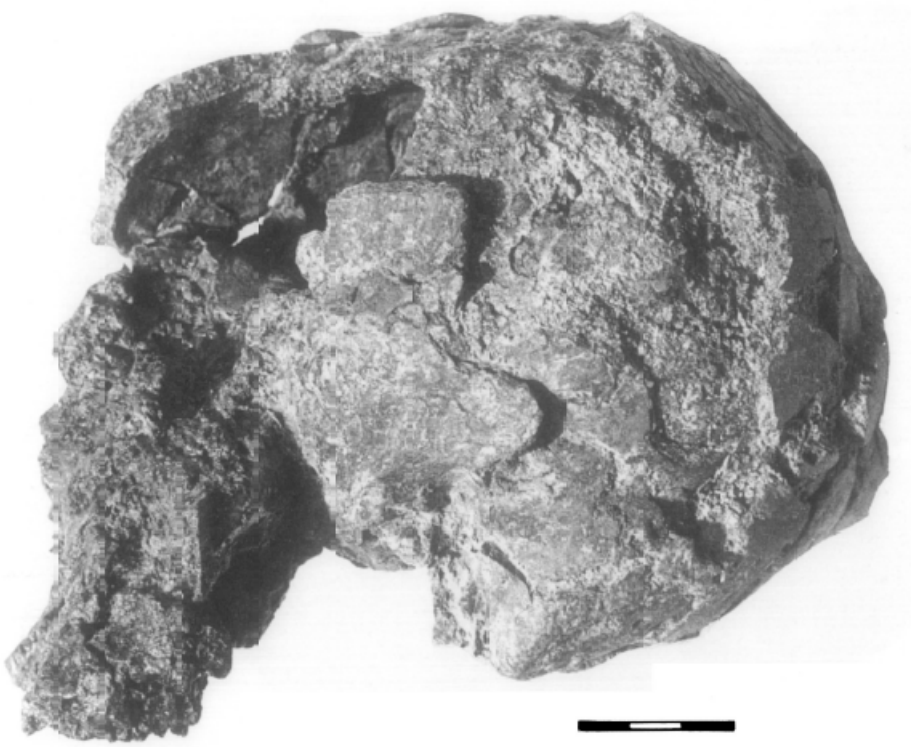

Figure 1.2: Ndutu Cranium as delivered to R. J. Clarke in 1974, before the first reconstruction. From Clarke, 1990. *3 cm scale.*

The newly found remains were added to the reconstruction (Figure 1.3). The facial skeleton, including the newly found supra-orbital fragment, was re-positioned. This time again taking into account the preserved endocranial anatomy. Nevertheless, Clarke reiterated the preliminary status of this alignment. In his own words: "[the position of the facial fragments] *should be regarded only as a reasonable approximation"* (Clarke, 1990, p. 707).

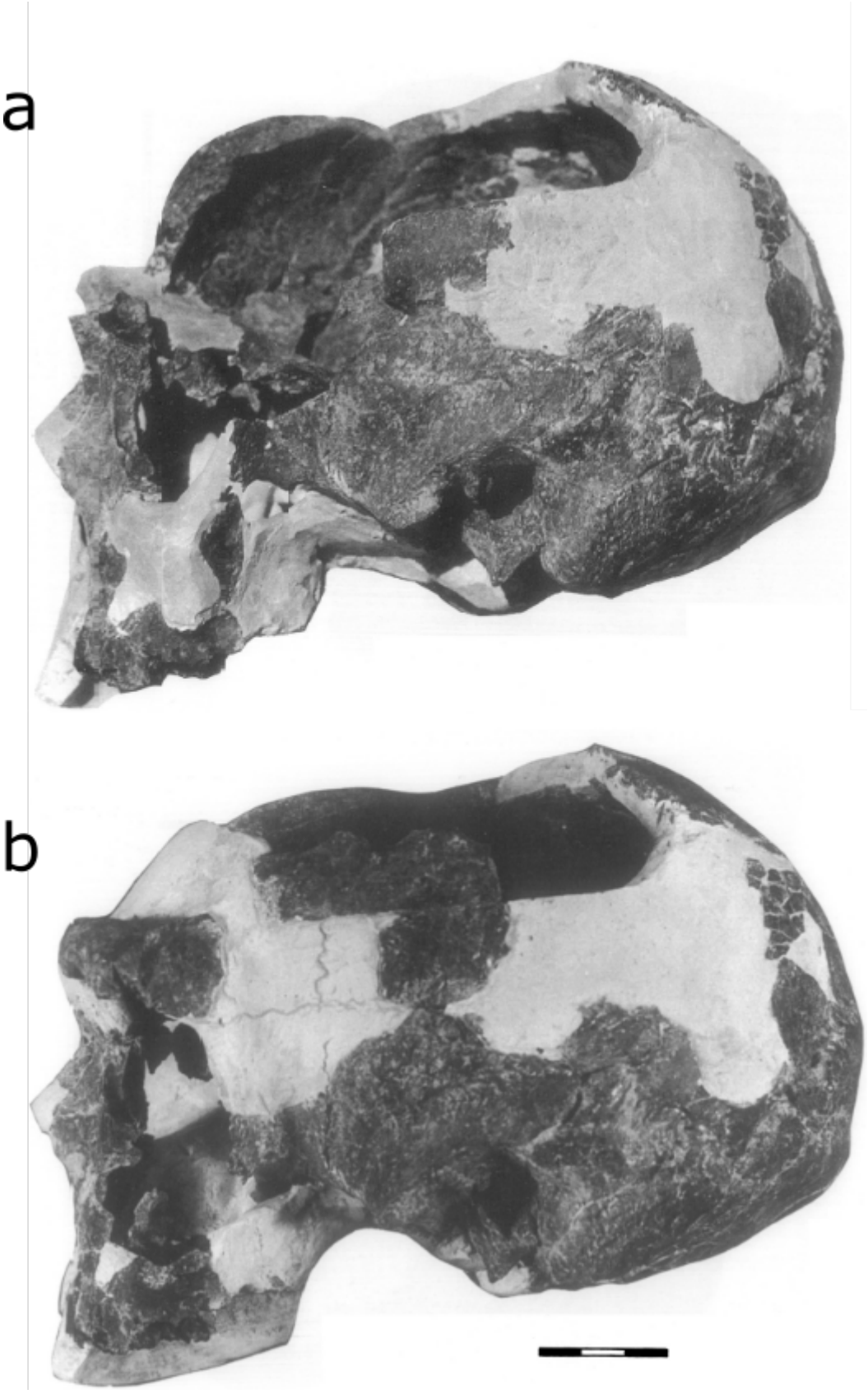

Figure 1.3: Previous reconstructions of the Ndutu Cranium. Composed from Clarke, 1990. *Cranium as reconstructed in 1976 (a), before adding the fragments found in 1978, and as in 1990 (b). 3 cm scale.*

1.2.1 Specimen Preservation

Clarke's 1990 reconstruction is the prevailing version of the Ndutu cranium. In its current state[1], the cranial vault is represented by fragments of both sides of the frontal, excepting the middle part, the eroded and distorted parietals, worn temporal squamae and a fragmented occipital squama. The vertical and bregmatic areas are missing and due to the distortion and scant preservation of the outer table of the parietals, few features apart from those who stem from Clarke's interpretations can be perceived. Most of the squamae and the mastoid portions of the temporals were in rather good condition, although their superior rim is mostly missing and the contour of the squamosal suture should be rather hard to discern, though an arched outline may be distinguished most easily on the right temporal squama. The petrous portion of the left temporal is also incomplete as reported by Clarke (1990).

The Ndutu cranium preserves most of the circum-nasal area and the inter-orbital pillar, this includes the infero-medial and medial rim of both orbits, a small immediately adjacent portion of the sub-orbital surface of the maxilla, and the inferior rim of the base of the zygomatic process. Small fragments of the nasal floor and palate are available, only a few documenting the palatal surface. A small section of the left side of the dental arcade is also present, documenting the position of the alveoli of the premolars and the first two molars. Nonetheless the alveolar process is quite eroded and only a few parts of it can delineate the outer and inner contours of the arcade. The excavation yielded only a few small dental fragments, including pieces of the roots of the canines, the first and second premolar and the first molar.

As mentioned before, a sizeable fragment corresponding to the upper and upper-external rim of the left orbit is available. This fragment records the supra-orbital torus on this section, as well as a brief segment of the temporal line behind the orbit from near the point where it intersects the fronto-zygomatic suture and on to where it appears to acquire a trajectory that is parallel to the midline.

Most of the bones in the entire cranium are crushed and fragmented, but have been reassembled. The best preserved part of this specimen is the occipital squama, albeit it is broken and damaged near the mid line, behind the foramen magnum. It is also missing parts of the basilar portion, including the left occipital condyle. The medial portion of the glenoid fossa of the right temporal bone, and the majority of the sphenoid bone, exempting some parts both greater wings and a piece of the left lesser one, are completely absent.

1.3 Morphological Interpretations

As early as in 1973, data obtained from the first reconstruction of the Ndutu cranium was used to compare it to a larger sample of hominid skulls by P. Andrews and D. Williams. In their publication in the American Journal of Physical Anthropology, they presented an early example of the use in bioanthropology of a Principal Component Analysis (PCA) - a now prevalent multivariate statistics summarizing and visualizing tool (for more, see Subsection 2.4). Apart from warning against the misinterpretation of this analysis, they concluded that the Ndutu individual was closest to the cranial specimens recovered from the Peking Man Site in China (Zhoukoudian) [2].

[1] For a summary of the preserved parts, see Table 2.1 in Section 2.1.1.

[2] Clarke refers to these as *H. erectus pekinensis*. Here I omitted these names as frequently as possible because controversies regarding taxonomic designations are commonplace.

In Clarke's own morphological study published in 1976, he noted various traits in the Ndutu cranium that he also considered that resembled the Zhoukoudian crania. Among these he cited, from the specimen's well-preserved occipital bone, a notoriously thick nuchal torus that became bulkier towards the limit between the lambdoid and the occipito-mastoid sutures (*asterion*).

From the mid-sagittal craniograms of the occipital he elaborated, he extracted that the posterior sagittal profile of this individual was rounder than that of the Ngandong specimens, but displayed a more acute angle than modern humans. He also noticed differences in terms of the occipital curvature with the cranial specimens of Swanscombe and Steinheim. This outline was ultimately closest to Zhoukoudian cranium III.

According to his 1976 publication, this trait was coupled with a small, triangular mastoid on the left temporal, which boasted a defined mastoid notch, whose flat rear lied in the nuchal plane. The mastoid region seemed only superficially close to that of O. H. 9 and different from that of the Steinheim cranium.

Despite the damage to the rest of the anatomy, he also listed evidences of a relatively vertical forehead, unlike that of the Ngandong and Kabwe specimens - the latter of which is much larger. This added to a thick cranial vault, well within the range of the thickness recorded in the skulls of Zhoukoudian by Weidenreich. As mentioned previously, he predicted a supra-orbital torus, which added to the observation that the cranium appeared to have a pear-shaped outline when viewed from atop (*norma verticalis*) that distinguished it from the Ngandong and Omo II specimens.

Unlike the Chinease crania, the Ndutu cranium exhibited an ossified styloid process and a supra-mastoid crest that was interrupted before branching over to the external acoustic meatus. On the left, the inferior margin of this orifice was noted thick and downward pointing. Nearby lied a deep, small and anteroposteriorly short glenoid fossa with a damaged entoglenoid process.

From the less pristine parts, Clarke (1976) deduced that the presence of a sagittal torus was unlikely. In fact, the better preserved parts of the parietals flaunted but faint temporal lines. In a criticized proposition (see G. P. Rightmire, 1983), he posited the vault's vertical sides and the parietal's boss as evidence of a relationship with *H. sapiens*. Concerning the preserved facial skeleton, Clarke advanced that the nasal aperture suggested a rather large nose.

Four years later, M. H. Wolpoff (1980) included the Ndutu cranium in a publication where he discussed the relevance of sexual dimorphism in the morphological diversity of Middle Pleistocene hominins. He posited that the differences between some specimens of that age could be explained by their attribution to distinct sexes of possibly a single taxon closely related to Neanderthals. Regarding Ndutu, he mentioned that its small size could imply that this individual was female - an assertion that would be subsequently criticized.

In (1983), G. P. Rightmire rendered a more detailed description and discussion of the Ndutu cranium's affinities. Firstly, he noted that Ndutu had a length similar to that of the Koobi Fora specimen KNM ER 3733 - this, considering an estimate of the *glabella-opisthocranion* length. He noted the specimen's pronounced post-orbital constriction. Having already had access to the revisited reconstruction (the one corresponding to Clarke's (1990) publication), he described the supra-orbital as round, thick, and similar to that of KNM ER 3733 and O. H. 12, but more gracile than the tori of the Kabwe and Bodo exemplars.

Like Clarke in (1976), Rightmire also made comments about the temporo-mandibular joint and the external acoustic meatus morphology. He noted a glenoid fossa shallower than that of the Kabwe cranium with a prominent articular tubercle and a small entoglenoid process. He also stated that the acoustic meatus appeared vertical and elliptical in shape, displaying, in its lower border, a tympanic plate that was particularly thin and sapient-like, as in Kabwe.

Most notably, Rightmire's (1983) publication denounced the overestimated fullness of the frontal bone in the reconstructed Ndutu cranium. Leaving the purported frontal and supra-orbital morphology aside, he reckoned the Kabwe and Omo II to be closer to Ndutu overall. He also criticized the exaggerated parietal bossing in Clarke's reconstruction. Nevertheless, the author acknowledged that the steepness of the lateral walls of Ndutu's cranial vault could be accurate.

In Rightmire's view, the cranium's vertical outline (broadest at the mastoids) was comparable to the Omo II, Elandsfontein, and Kabwe crania. However, he judged that, viewed from the rear, the Ndutu cranium had a general resemblance to the one from Elandsfontein, albeit with a noticeably weaker parietal keeling.

Like previous authors, Rightmire heeded the occipital bone's remarkable flexure and thickness. In his opinion, the preserved Ndutu occipital and temporals were closest to *H. sapiens*. Unlike the forward-sloping occipital plane of the fossils assigned to *H. erectus* and related taxa, the orientation of the distal end of the Ndutu occipital squama is vertical. According to him, the transverse torus under it was as faint as the boasted by the Omo II calvarium and unlike that of Kabwe or Elandsfontein.

From the occipital, he also noted that Ndutu held a modern looking long *lambda-inion* chord, although he cited the example of Omo II, an exemplar he deemed otherwise modern that displayed an extensive nuchal plane. He observed that, like Kabwe, the Ndutu cranium's nuchal area was relatively flat. Above it, he disclosed the presence of a supra-toral sulcus. He commented the absence of a supra-iniac fossa, such as the described in European Upper-Pleistocene crania.

Ndutu's juxta-mastoid complex was also not nearly as protruding as that of Neanderthals. In fact, the lack of a definite angular torus aside a wide supra-mastoid sulcus bounded by a weak supra-mastoid crest extending onto the parietal resembled that of the Kabwe cranium.

Furthermore, Clarke argued that the Ndutu specimen could be discriminated from the Zhoukoudian and Neanderthal crania by the absence of a distinctive ridge riding the occipito-mastoid suture. Based on a personal communication of R. Holloway, Rightmire put forth an estimation of Ndutu's endocranial volume of 1098 cm^3, falling within the range of specimens attributed to *H. erectus*. However, he admitted that Ndutu could not be distinguished from modern humans based upon this measurement.

Taking into consideration the observations made about the Ndutu cranium's occipital, temporomandibular joint and tympanic plate, Rightmire concluded that its morphology was consistent with *H. sapiens*. Withal, he posited an arising conundrum: that, if accepted within *sapiens*, it followed asking which of several proposed subspecies or evolutionary "grades" would it be best to allocate this seemingly transitional specimen to.

On one side, a grade-based designation - that is, an appointment conveying the attainment of a particular evolutionary stage that can be reached by different taxa (Conde & Ayala, 2014) - would render Ndutu within the scope of the *H. sapiens* grade 1 in Stringer's framework (1979 *in* G. P. Rightmire, 1983), alongside many of the aforementioned similar specimens and the European fossils from Petralona and Bilzingsleben. This conclusion would be supported by G. Bräuer in a publication in the following year, although excluding these last two European exemplars and adding a few others. To supporters of this arrangement, such as Bräuer (1984), the Ndutu cranium was nothing less than a proper representative of the early archaic *H. sapiens*.

On the other side stood the more rigid option of providing Ndutu with a trinomial designation. Regarding this possibility, Rightmire (1983) decried that the notion of grades neglected a crucial aspect from a phylogenetic stance: the relationships between the populations ascribed

to them. Therefore, in regard of its similitude to other Tanzanian fossils, such as the Kabwe, Elandsfontein and Bodo exemplars, he gathered that the taxon *H. sapiens rhodesiensis* would be fit.

It would not be until six years later that Clarke would publish a revised description of the Ndutu cranium addressing the issues raised by Rightmire, Bräuer, and others. A new and more extensive description and comparison featuring the updated reconstruction of the Ndutu cranium appeared in the Journal of Human Evolution in (1990).

This time, Clarke had the opportunity to compare the cranium with the one recovered from the site of Salé, Morocco in 1971 and the SK 847 cranium that he worked on before 1977. He also referenced the O. H. 9, KNM ER 3733, and the Steinheim specimens, and elaborated craniograms to compare the Ndutu cranium with Zhoukoudian skull XII, following Weidenreich (1943 *in* Clarke, 1990). Subsequently, he discussed the assessments of other researchers and considered the archeological context of the find. Finally, he extended his construal of the specimen's phylogeny.

Clarke's (1990) assessment found striking similarities between the Salé and Ndutu specimens both in size and shape, specially from behind, but also from above, due to its parietal bosses[3]. This likeness added to a possibly corresponding geological age of *circa* 400 Ka BP, according to J. J. Hublin (1985 *in* Clarke, 1990). Like Ndutu, Salé was a rather gracile specimen with a low cranial capacity ($\sim$ 930 cm^2). It also lacked a sagittal keel along the parietals, had a deep and short glenoid fossa, an ossified styloid process, a similar supra-mastoid region, a modern-looking rounded occipital, and *H. sapiens*-looking basilar proportions. Although also incomplete, the Moroccan specimen possessed a better preserved frontal bone displaying a sagittal keel and strong post-orbital constriction - all traits not observable in Ndutu.

Considering the morphology observed in O. H. 9, SK 847, and KNM ER 3733, Clarke retracted his claim that the absence of a sagittal torus and the presence of a short supra-mastoid crest linked the Ndutu cranium with *H. sapiens*. He found that the sole complex of sapient-like traits absent from *H. erectus pekinensis*, and *H. erectus* were the less pronounced occipital-nuchal plane angle (*occipital angulation*, coupled with a down facing occipital plane, and (again) parietal bosses.

In this publication, Clarke also responded to the criticism raised by Rightmire (1983) concerning his reconstruction by providing a more detailed explanation about the way the parietals were affected by taphonomic distortion and the effects on his reconstruction of the parietal fragments. He explained that the effects of plastic deformation particularly altered the shape of the right parietal, making it possible to approximate the left parietal's genuine configuration upon reconstruction. Moreover, he argued that it was the verticality of the temporal and parietal walls that Rightmire admitted to agree upon, added to the verticality of the occipital plane, what encouraged him to reconstruct the parietals with such a generous amount of boss. The Ndutu cranium's newly found likeness to the Salé specimen, who also boasted parietal bosses, only added to this hypothesis.

Thereupon, he debated that the presence of a strong post-glenoid process, a delicate inferior tympanic border, and the characteristics of the styloid process that Rightmire (1983) held as *H. sapiens*-like traits observed in the Ndutu individual were in fact traits that the Ndutu cranium retained from a primitive stock, provided that they were observable in some earlier specimens. For example, the fragments at that point attributed to SK 847 exhibited both an ossified styloid

[3]Unfortunately, the Salé specimen would later be revealed to display a morphology partly resulting from a pathology in a description published in (2002). Upon observation of the specimen's nuchal arches, Hublin concluded that their asymmetry could be due to a pathological condition.

process and a delicate tympanic plate, while a robust post-glenoid process was also recorded in O. H. 9.

Clarke, nevertheless, agreed with many of the arguments exposed by Rightmire, as well as with some of the statements of Bräuer ((1984)). For instance, he noted that the raised articular tubercule, forming almost a distinct entity in the Ndutu pre-glenoid plane, was completely unlike the morphology displayed by SK 847, KNM ER 3733, O. H. 9, and the Ngandong and Zhoukoudian crania. Furthermore, he admitted that their disagreement was essentially a matter of deciding to allocate the Ndutu specimen, which stands somewhere in between *H. erectus* and *H. sapiens*, to either an evolved version of the former or an archaic form of the latter.

This assertion (that the Ndutu individual indeed belonged to a population that could be viewed as transitional) was further supported by Clarke's observation of the endocranial surface of the occipital squama. Here, the cruciate eminence - the meeting point of the internal occipital crest and the sagittal and transverse sulci bordering the cerebral and cerebellar fossae (White, Black, & Folkens, 2012) - lied lower than in the specimens attributed to *H. erectus*, implying that the depressions left by the cerebrum were larger than in these fossils.

Although he had defended the first arrangement in his (1976) publication, by (1990) Clarke had opted for the second one, that is, that the Ndutu cranium belonged to a *"representative of archaic* Homo sapiens" (Clarke, 1990, p. 727). Yet, he admitted that it fell within the range of the same cranial morphotype as the Salé and Steinheim crania. Clarke suggested that this morphotype might represent a collection of hominins that, even when they did not necessarily belong to the same taxonomic group, were distinct from a contemporaneous one formed by the Bodo, Kabwe, Saldanha and Petralona specimens (albeit without specifying whether that distinction could be stablished at the sexual, racial or subspecific level). Both these groups roamed between *circa* 400 to 200 Ka BP, and were distinguishable from a more recent group including the Florisbad, Omo 2 and Ngaloba individuals who inhabited the planet around 200 to 100 Ka BP.

Interestingly, he ventured that such morphotype might indeed derive from an early African lineage unrelated to the one leading to Asian *H. erectus* populations. Furthermore, he posited that this ancestral lineage, for which he proposed the name *H. leakeyi*, developed a distinct technological repertoire – i.e., the Acheulean – and remained west of the Movius line. In Clarke's view, specimens like SK 847 and KNM ER 3733 could have constituted representatives of this *"ancestral stock from which archaic* H. sapiens *populations as represented by Ndutu* [...] *and Steinheim could have evolved passing through the* [...] H. erectus *morphotype displayed by* [the Ngandong and Zhoukoudian crania]" (Clarke, 1990, p. 728).

1.4 Ndutu and the origins of *H. sapiens*

Clarke's detailed recount of the Ndutu cranium's morphology was late and extensive enough to quench other researcher's desire to dedicate further publications exclusively to this specimen. It, nevertheless did not settle the argument surrounding it's taxonomical attribution or phylogenetic relationships. As explained by Clarke (1990) himself, the reason for this was that, beyond the presence of the readily distinguishable features, the assignment of the suite of traits exhibited by Ndutu to one or another taxon, firstly demanded the settlement of the debate surrounding the amount of species that exist within the genus *Homo*.

If restricted to *habilis*, *erectus*, and *sapiens*, an early grade within *H. sapiens* would suffice. If more species or subspecies (such as *heidelbergensis* and *rhodesiensis*) were made available,

this would depend on which and how many of them the rest of the Middle Pleistocene hominin fossils worldwide would be sorted into. Furthermore, what relationship would the Ndutu individual's population hold with regards to our own kind? And what about the Neanderthals? Because of these interrogations were still unresolved, Clarke's interpretations about the Ndutu cranium's place among Middle and Late Pleistocene hominin diversity and its role in the evolution of the *H. sapiens* lineage were continuously discussed in many citing publications.

In 1996, Rightmire published a report on the Bodo fossils where he took into consideration evidences from African, European and Asian Middle Pleistocene sites (including Lake Ndutu) to advocate in favor of an Afro-European *H. heidelbergensis*. The Bodo specimen from the Middle Awash region of Ethiopia displayed a number of interesting features, including a notably robust morphology, cut marks in the facial portion, and an age of 0.64 Ma.

The partial cranium, consisting of most of the facial skeleton, an almost complete frontal bone, and various portions of the parietals and the left temporal, displayed prominent, thick and rounded glabella, a massive inter-orbital pillar, a nasal aperture with a vertical profile, and a vertical sub-orbital surface, but lacks a canine fossa and boasts no malar tubercule. The post-orbital region appeared slightly constricted and there is a midline keel behind the frontal squama. It boasted a parietal tuber marking the maximum breadth of the cranial vault. A second individual demonstrated that a supra-mastoid crest extending onto the parietal surface and an elongated angular torus was present in the Bodo population.

The cranium shared many features with *H. erectus* fossils like Sangiran 17, yet its endocranial volume was considerably larger. Most importantly, the Bodo individual's size and overall robusticity resembled Middle Pleistocene specimens like Kabwe and Petralona. To Rightmire, this indicated that Bodo and similarly large brained individuals from both Africa and Europe, encompassing the Mauer mandible, Petralona, Arago, Kabwe, Elandsfontein, and Ndutu, manifested a rapid episode of encephalic enlargement in human evolution. This was indicated the evincement of parietal bossing and an arched squamosal suture, which manifested alonside a vertical nasal aperture profile, mid-orbit divided brows, and the position of the incisive canal. In his view, these exemplars were best classified in the taxon *H. heidelbergensis*. This species, could not be satisfactorily grouped with the more derived European and West Asian fossils displaying Neanderthal-like features.

Given that the taxon would have originated in the early Middle Pleistocene, there was some temporal overlap with later *H. erectus* representatives in Java and China, which disclosed a problem regarding their relation to these populations. To resolve their connections, Rightmire proposed four scenarios, from which he favoured the first two: either the Asian specimens had parted ways with *H. heidelbergensis* who in return gave rise to the Neanderthals and modern humans, or they were was ancestral to all three groups. The remaining scenarios suggested that *H. heidelbergensis* was ancestral only to Neanderthals. While one posited that Asian *H. erectus* was ancestral to *H. heidelbergensis*, the other implied that they shared a common ancestor with modern humans.

The following year, J. L. Arsuaga and colleagues published a lengthy article concerning the affinities a collection of recently discovered early European hominin crania. The group of specimens recovered by the team lead by Arsuaga, Bermúdez de Castro, and E. Carbonell from the Sima de los Huesos deep vertical shaft in the Sierra de Atapuerca at the Burgos municipality of Castile and Leon (Northern Spain), have been interpreted as akin to an ancestor of the Neanderthal lineage. The sample shared many features with later Neanderthals but retained many

other primitive traits (Arsuaga, Martınez, Gracia, & Lorenzo, 1997).[4]

A metric study among the long series of comparative analyses put forth to justify their conclusions featured the Ndutu cranium. Arsuaga and colleagues considered eight metric variables from the occipitals of a sample of Middle and Late Pleistocene hominins. These variables described a considerable portion of the occipital morphology, including the occipital curvature, the occipital angle, and the *inion-opisthion* chord. In a PCA of these variables, the Ndutu cranium also proved to be similar to the very complete Sima de los Huesos 5 cranium, but was closer to the Steinheim, Tabun 1 and Zhoukoudian XI fossils.

In a more recent development, and in light of new emerging data (such as evidence of gene flow between Neanderthal, sapient and Denisovan populations, mutation rate estimates, the dating and affinities of the Sima de los Huesos sample, and mtDNA coalescence data) Chris Stringer (2016) reviewed the state of the relationships between the specimens in the Middle to Late Pleistocene human fossil record, including the Ndutu specimen.

Regarding Ndutu, Stringer settled on an arrangement similar to the one endorsed by Clarke. Despite lacking some information, he uttered that specimens like the Ndutu cranium, alongside the Thomas Quarry mandible represented an archaic morph of *H. sapiens*. Notably, by the time of this publication, Stringer had settled on a working definition of *H. sapiens*. In it, he also viewed the presence of parietal bosses as tell-tale sings of our species, yet the similitude stopped there.

He complemented this delineation with traits that Clarke did not consider pertinent in (1990), or did not possess the data to discuss. Apart from a high and globular cranial vault, Stringer's definition included a *retrocessive* face (tucked under the neurocranium) with a gracile and double-arched supra-orbital torus, a flexed basicranium - i.e., *cranial flexion*, the antero-inferior migration of the posterior half of the cranium (Skelton & McHenry, 1992) - , a "true" chin or *mental osseum*, a dental micro-structure suggestive of an extended post-natal growth period, and a pelvic shape characterized by short superior pubic rami. Additionally, unlike Clarke, he regarded the Steinheim cranium as closer to the Neanderthal lineage than Ndutu.

In his work, Stringer aimed to answer three questions regarding modern human origins. The first concerned the species diagnosis of *H. sapiens*. Beyond the aforementioned demarcation of our species, he pondered the variation admitted in his list of traits and the need to fulfill these criteria.

In close relationship, the second inquiry was the *tempo* and *mode* of Middle to Late Pleistocene hominin evolution. Regarding the mode, the question contemplated whether the evolution of the sapient and Neanderthal lineages could be best described by gradual or punctuational evolution. On this matter, Stringer cited the previous works of T. Weaver (2012 *in* Stringer, 2016) where he argued the evidence favoring the punctuational model - namely, the uniqueness of modern human morphology, the stemming (coalescence) of mtDNA lineages at $\sim$ 200 Ka BP in Africa coupled with the date of the earliest modern-looking remains. Following a quantitative approach, Weaver showed that gradual process models could also account for the purported observations. On the other hand, E. Trinkaus' work (2006 *in* Stringer, 2016) manifested the dis-equality between the Neanderthal and sapient lineages in terms of the rate of evolutionary change.

The third question cogitated about the identity of last common ancestor (LCA) between these evolutionary branches. Stringer cited A. Mournier and M. Lahr's virtual reconstruction

[4] As recently as 2019, a team lead by M. Demuro dated the LU-6 layer from where they were recovered using thermally-transferred optically stimulated luminescence. The resulting mean date of 448 $\pm$ 15 made these the earliest hominins displaying Neanderthal traits in Europe.

of the appearance of the Neanderthal-sapient LCA. This simulation best resembled *H. heidelbergensis*, considering an Afro-European wide-range definition. Alternatively, the modern-looking maxillary morphology of the ATD6-69 specimen from Gran Dolina, as described by J. Bermúdez de Castro, M. Martinón-Torres, E. Carbonell, S. Sarmiento, A. Rosas, J. van der Made and M. Lozano (2004 *in* Stringer, 2016), presented another LCA candidate, present as early as 850 Ka BP.

To answer these questions, Stringer (2016) presented three possible schemes (Figure 1.4). In the first one, he considered a strict definition of *H. sapiens* and *H. neanderthalensis* - that is assigning specimens displaying only some of the diagnostic features to another species, thus limiting the member specimens to post-MIS 8 fossils. This hypothesis presented the taxon *H. heidelbergensis* as the common ancestor between both lineages, given the inclusion of the Mauer mandible in the same group, or *rhodesiensis* if not. Here, *H. helmei* is placed as a step prior to the attainment of full-blown *H. sapiens* morphology, while the Steinheim population precedes the Neanderthals.

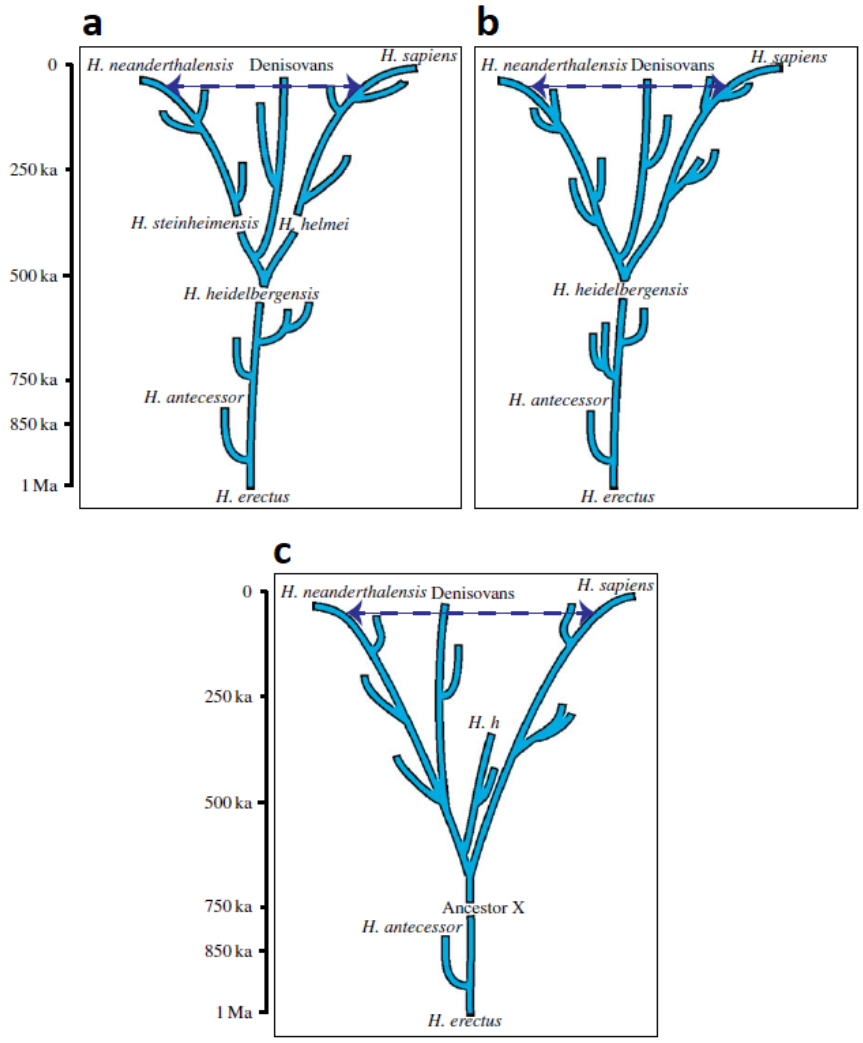

Figure 1.4: Schemes presented in Stringer, 2016. (a) H. steinheimensis *and* H. helmei *are ancestral to Neanderthals and* H. sapiens*, respectively.*, (b) H. heidelbergensis *is ancestral to both, and* (c) *both* H. sapiens *and* H. neanderthalensis *lineages diverge from "Ancestor X" before 500 Ka BP.*

The second scheme allowed for a broader definition of both terminal taxa, which subsumed the hominins approaching the modern human morphology to the informal term "archaic *H. sapiens*" (favored by Stringer). Although this scenario also bestowed the title of LCA on *H. heidelbergensis*, it suggested that the relationship between that taxon and *H. sapiens* is complex, proposing an "African multi-regional" origin for the latter.

In the third setting, the position LCA between Neanderthals and extant humans is given to "Ancestor X", a hominin already displaying the derived maxillary morphology observed in the *H. antecessor* holotype specimen ATD6-69 - a trait lost in *H. neanderthalensis*, but present in *H. sapiens*. In regards to this trait, he contended that *evolutionary reversals* were indispensable to derive the Neanderthal maxillary anatomy from ATD6-69.

Furthermore, from Stringer's perspective, disputable African fossils could be divided among those more closely resembling Neanderthals (dubbed *H. heidelbergensis*) and those approaching *H. sapiens* based on the presence or absence of this trait. This would thus set fossils like Bodo and Kabwe (or even Petralona and Arago) from the Ndutu and Thomas Quarry crania. In this scenario, *H. heidelbergensis* could constitute a European offshoot of the Neanderthal descent, unrelated to the fossils leading to *H. sapiens*.

The author also commmented on the date and affinities of the Sima de los Huesos hominins, effectively pushing the occurrence of fully Neanderthal characteristics to (at least) 400 Ka BP and the divergence of their lineage even further back in time, considering mutation rates (to 550 to 765 Ka BP, in which case they could be consistent with scheme two). Citing R Lacruz and colleagues (2015 *in* Stringer, 2016) and Bermúdez de Castro and Martinón-Torres (2014 *in ibid.*), Stringer argued that perhaps *H. antecessor* constituted the most likely candidate for the Neanderthal-sapient LCA.

On the sapient side of both the second and third schemes, the African crania associated with early Middle Stone Age technology - i.e. the Florisbad, Djebel Irhoud, Ngaloba and Herto specimens - instantiated a complicated road to modern *H. sapiens*. As mentioned previously, in Stringer's view the evolutionary mechanics making it possible for anatomical modernity to stem from such a variable collection of specimens (to which, like many, he adds the Skhul and Qafzeh crania) are best described by the African multi-regional model. In this framework, a collection of morphologically distinct populations (sampled by the available morphologically disparate fossils) coexisted in Africa during the late Middle Pleistocene. These populations living in temporal proximity, traversed their evolutionary tracks independently, at times separated by biogeographic barriers, until they eventually coalesced in the full suite of *H. sapiens* traits.

The following year, Rightmire published his own take on the evolution of *H. sapiens*. In this work, he discussed the morphological changes in the skulls of Middle to Late Pleistocene hominins, reflecting on the temporal and regional differences among them and their taxonomic relevance. Concomitantly, he arrived at different conclusions regarding the Ndutu cranium's place among them.

The author employed craniometric data revealing relative brain size, cranial vault shape (globularity), supraorbital torus thickness, postorbital constriction, parietal expansion, occipital angulation, occipital squama shape, and facial proportions. He then pondered the variation of these measurements within and among groups of hominins constructed based on temporality and geography, but emphasizing morphological similarities, which he deemed indicative of their affiliation to paleo-demes (*p*-demes in G. P. Rightmire, 2017; that is, *ancient* local alele-interchanging populations (Wood & Lonergan, 2008)) or grades.

In his rendition of the evolutionary road toward anatomical modernity, Rightmire (2017) presents two alternative schemes. On one hand, he considers Bräuer's (2008 *in ibid.*) proposal

– an arrangement closer to Stringer's (2016) second scheme in the sense that it advocates for a complex, gradual, and multi-regional path with *H. heidelbergensis* on one end and fully modern *H. sapiens* on the other. On the other hand, he envisages Tattersall and Schwartz's (2008 *in* G. P. Rightmire, 2017) hypothesis, where the sapient trait complex emerges in a distinctive point in time through a speciation process (punctuationally).

To solve this conundrum, Rightmire groups Middle and Late Pleistocene specimens into *p*-demes and compares them to the more recent Dar es Soltane specimen, a mean of the Nazlet Khater, Hofmeyr and Border Cave specimens and modern Zulu crania. He then attempts to identify trends in hominin evolution toward *H. sapiens*.

To Rightmire, the Ndutu cranium, alongside the Bodo, Kabwe, Saldanha, Zuttiyeh, and Omo 2 specimens, exist outside the sapient range, in a group that he deemes equivalent to Bräuer's *"early archaic grade"*. The exemplars in this group are characterized by lower and broader cranial vaults than those of the Florisbad, LH 18, KNM ER 3884, Omo 1, Djebel Irhoud, Herto, Singa, and Aduma specimens (although not later Levantine fossils, like Skhul V). They also exhibit a relatively low endocranial volume (within the range of *H. erectus*) and high postorbital constriction. Finally, they have massive supraorbital tori along with a correspondingly high degree of facial projection.

A second ancient *p*-deme includes the Florisbad, LH-18, KNM ER 3884, Omo 1, and Irhoud 1 and 2 crania. This grouping captures very broad skulls, of which Irhoud 2 is the most notable. A flat frontal, constricted behind the orbits is also characteristic of this group, yet the parietal bossing is no longer within the range of *H. erectus*. Both in this group as in some of the later specimens, the occipital is more rounded than in the Bodo and Ndutu group. Although with the notable exception of the Hofmeyr cranium, the face in these and more recent specimens is also shorter.

Cranial globularity sets this group and the rest apart from the one where Ndutu is included (in G. P. Rightmire, 2017 this is defined metrically by $XCB \times BBH/GOL^2$, where XCB is the maximum cranial breadth, BBH is a chord between *basion* and *bregma* and GOL is the distance between *glabella* and *opistochranion*, indicating the maximum length of the cranial vault). This magnitude progresses throughout Rightmire's *p*-demes sequence but only comes close to modernity in the later Pleistocene exemplars.

The Florisbad group is followed by a deme encompassing the most complete of the Herto specimens (BOU-VP-16/1), the Singa exemplar and the Aduma ADU-VP-1/3 partial vault. Here, the length and height of the skull and the roundness of the occipital are greater than in the last two, approaching modernity.

The most recent group is represented by the Skhul IV, V and IX crania, as well as Qafzeh 3, 6 and 9. Skull height and length in this group is comparable to Hofmeyr and the modern Zulu people. Post-orbital constriction in this group is near-modern and so is their dome-like frontal squama. However, the occipital angle in this group is notably variable, for which Rightmire argues that it is of little use to distinguish between Middle and Late Pleistocene hominins. Similarly, when comparing the size of the nuchal and occipital planes, much variation is observed, for which it seems hard to discern any trends.

In the end, although he recognizes that some traits like cranial globularity and postorbital constriction appear to proceed gradually, Rightmire favors a punctuational scenario. According to Rightmire's work, examples of gradual progression can be seen in cranial globularity and post-orbital constriction, while punctuated changes include cranial breadth, occipital angulation and supra-orbital torus thickness - the later of which albeit expressed variably across Middle to Late Pleistocene hominin populations, seems to be influenced by facial projection.

As a result, he allocates all of the specimen groups, except for the one comprising Ndutu, to a clade that includes *H. sapiens*. Similar to how he suggested in 1996, to Rightmire this *"suggests* [another] *speciation event"* (G. P. Rightmire, 2017, p. 16050). Although reticent in previous publications (see G. P. Rightmire, 1983), Righmire added that the appropriate designation for the Ndutu cranium and similar fossils should be *H. heidelbergensis*, or *"a closely related species restricted to Africa"* (G. P. Rightmire, 2017, p. 16048) – i.e., *H. rhodesiensis* (see G. P. Rightmire, 2008), provided that Zuttiyeh (the only non-African exemplar) is excluded from the group.

These conclusions stood in rather good agreement with a widely celebrated publication issued the same year. A few months after Rightmire's last publication, a breakthrough development regarding the Djebel Irhoud site (a mine 55 Km southeast of Safi Morocco, from where the Irhoud 1 and 2 specimens were recovered) appeared in Nature. In it, Hublin announced the discovery of additional hominin fossils (an adult skull (Irhoud 10), a mandible (Irhoud 11), a maxilla, and several dental and post-cranial remains) alongside a new date for the site's sediments. Stratigraphical information recompiled by himself and previous researchers, added to the morphological consistency of the skeletal remains, suggested that possibly all of the hominin remains accumulated in the site during a relatively short span of time which took place c. 300 to 350 Ka ago, following thermo-luminescence dating results. These results deposed the 195 Ka old Omo Kibish fossils from the position as the earliest representatives of our species.

Perhaps most notably, Hublin argued that the Djebel Irhoud sample's infra-orbital, zygomatic, and maxillary morphologies fall within the range of recent humans. This includes Irhoud 1, who (he adds) displays double-arched, albeit projecting supra-orbitals, unlike Irhoud 2 and 10 - a difference he attributes to sexual dimorphism. A mandible recovered earlier from the site (Irhoud 3) displays an inverted T-like protrusion, held by many (including Stringer) as diagnostic of *H. sapiens*, which is incipient in the newly found Irhoud 11 mandible. Opposing previous interpretations, an analysis of the abundant dental elements also revealed that the Djebel Irhoud remains lacked various of the apomorphies seen in *H. neanderthalensis* specimens. Additionally, Irhoud 3's dental eruption pattern was also similar to modern humans.

In a GM analysis of cranial shape, Hublin concurred with Rightmire's observation that the Djebel Irhoud specimens were close to the Laetoli Hominin 18. A subsequent analysis of the endocranium also supported the association with the Omo specimens. Yet his analyses also indicated an affinity with a broadly spatially and temporally distributed group encompasing the Skhul, Qafzeh, Mladeč, Předmosti, and (even) Zhoukoudian fossils.

From the literature reviewed in the past sections, one can extract that, in its current state, the Ndutu cranium has been compared to other Middle and Late Pleistocene hominins in terms of cranial heigth, length, and width, parietal bossing, occipital angulation, proportions of the glenoid fossa, zygomaxillary anatomy, supra-orbital torus expression and facial projection. Both the latest authors to reference this specimen expose contrasting hypotheses both regarding the relationships between the cranial remains constituting the diverse Middle and Late Pleistocene human fossil record, and the its place among them: while some would allocate Ndutu to the base of a line ultimately leading to *H. sapiens*, others argue in favor of lumping it along the Kabwe cranium in a separate species closer to the origin of the Neanderthal lineage – an alternative that unavoidably leads to the discussion about whether the nomen *heidelbergensis* or *rhodesiensis* is most appropriate.

Perhaps a broad balance of all these traits should help gain the insight needed to approximate a conciliation between these oposing views. Yet, unlike the exquisitely preserved Kabwe specimen that it has been recurrently compared to, the Ndutu cranium remains a fragmentary exem-

plar. Given its particular taphonomic history, the true configuration of a number of meaningful features, including the extent and angle (prognatism/orthognatism) of the forward projection of the facial skeleton and the overall cranial flexion have become uncertain.

1.5 Digital Restoration Resources

The lack of confidence surrounding the Ndutu cranium reconstruction is an artifact of the state of fossil reconstruction in the time when it was reconstructed. Up until recently, reconstructions were done manually. This amplified the chance for subjectivity and bias, while precluding the detailed documentation of all the steps undertaken, which ultimately prevented replicability. In the current state of the art, manual, assisted and automated virtual reconstruction methods, such as crack removal, reflection, element duplication, digital reassembly, feature estimation and retro-deformation are applied almost routinely. These informatic resources not only offer less invasive approaches, preventing the possible damage that the substances or missteps of traditional reconstruction can cause to fossils, but they also deliver replicable and amendable reconstructions (Lautenschlager, 2016).

Non-invasive reconstruction techniques are made possible through digitization – that is, the collection of digital data to produce a representation of the physical materials. A plethora of techniques, including laser scanning, photogrammetry, and Computerized Tomography (CT) are nowadays commonly employed to produce 3D models of all sorts of archaeological and paleontological materials (ibid.). In computer graphics, 3D models are mathematical portrayals of real-world objects. They consist of vectors of points in a 3D space (sometimes referred to as point clouds) and their connections. Because every three of these points are connected by edges forming a triangle, they are also known as vertices. The plane defined by these edges is called a face. Together, vertices, edges, and (sometimes) faces form polygonal meshes that match the geometric configuration of the real objects (Autodesk, 2010).

Virtual reconstruction has been amply in paleoanthropology in recent years. A notable example is Di Vincenzo et al.'s 2017 digital reconstruction of the Ceprano calvarium, a distorted Middle Pleistocene specimen from southern Latium, Italy once attributed to *H. cepranensis* (which provided the inspiration for this work). The team scanned the calvarium and digitally removed the plaster of a previous reconstruction, creating a 3D model of the fossil without altering the original. After digitally repositioning some of the constituting fragments, they carefully studied the deformation to come up with a proper retro-deformation algorithm. After the reconstruction, they provided a new alternative interpretation of the specimen, appointing it as a representative of *H. heidelbergensis*.

In non-virtual settings, reassembling broken objects such as fossils, but also pottery, lithics, and even walls, is a routinary, time-consuming, costly, and error-prone activity. Hence, the development of techniques to assist and even automatize this task has worried paleoanthropologists, forensic anthropologists, archeologists, conservators-restorers, and computer scientists alike for years (the latter usually due to their interest in the "2D-" and "3D-puzzle-solving" mathematical problem (Papaioannou et al., 2017)). Eslami, Di Angelo, Di Stefano and Pane (2020) notice three stages in the progress of these techniques during the past three decades.

Throughout the 1990s, most researchers in this field were interested on developing computer techniques designed to assist in the documentation of the shape of fragmentary archeological items and their archiving. However, the first fully automatic virtual reconstruction method was presented in 1998 by Sablating and colleagues.

Still, it was until the following decade that the automatic and semi-automatic virtual reassembly methods became central. By that time, a few methodologies had already incorporated novel approaches such as the use of other fragment features besides geometry, such as colored and textures surfaces (applied, for example, in the reconstruction of frescos) (Eslami et al., 2020).

This decade also witnessed the widespread implementation of advanced algorithmic approaches meant to select from the many generated matching fragment pair candidates, such as continuous function optimization, global optimization, genetic algorithms, Bayesian probability functions, and maximum likelihood estimation. In the 2010s, technological advances allowed the implementation of computer vision systems (a. k. a., machine learning) to integrate morphological data into the process of feature extraction and pair matching (ibid.).

Regardless, the success of many of these techniques was still amply reliant on awfully specific conditions. Given that pottery sherds are one of the most abundant finds in classical archeology, most methods have been developed for the reconstruction of pottery (ibid.). This carried various assumptions, for example, regarding the final shape of the reconstructed object and the way fragments are affected by taphonomy, such as the presence of symmetry or of simple geometric features in the fragments and the absence of wear (Papaioannou et al., 2017).

These same closely constrained approaches have been employed to restore objects other than pots with some success (ibid.), but with limited applicability. In 2011, Wei and colleagues presented a pipeline for the reassembly and completion (that is, the reconstruction of missing parts, in this case, by hole filling) of forensic case crania. This included both automatic feature extraction and reassembly procedures that were guided by a modern human skull template. Feature extraction was performed by implementing an algorithm meant to detect "slippage features", which are invariant surfaces within a defined local geometry that can be segmented from the rest of the shape (Gelfand & Guibas, 2004). These key points are found in the template and the alignment transformation is computed. To solve for overlapping fragments, a global optimization algorithm that penalizes the intersection between matched fragment meshes is applied.

Wei and colleages (2011) tested their template-based reconstruction pipeline in three crania in varying conditions. Although they obtained promising results, they admitted that the results are significantly dependent on the prior choice of an appropriate template, and that fragments that are too small, featureless, or smoothed down cannot be properly aligned. To my knowledge, there are no further developments on this venue [5] and no software or code is currently available.

Nonetheless, as recently as 2019, Profico and colleagues published another template-based reconstruction method for human/hominin crania, this time in the presence of missing information. It however is notable that it clearly diverges from Wei et al's approach in the sense that feature extraction is landmark-based and that it lacks mesh intersection penalization. The reassembly of adjacent fragments is, in any case, beyond its purpose.

This approach, dubbed the "Digital Alignment Tool" (*dta()*), was released as a function in the Arothron R package (Profico et al., 2018), which runs in the R statistical computing software environment. The program finds the best alignment between two portions of a disarticulated model (DM), represented by two different 3D meshes corresponding to two non-adjacent fragments of the same individual, and a template – i.e., a reference model (RM) that is selected from a sample. For this to occur, the cartesian coordinates a common set of key points is selected and moved to the nearest vertex in the corresponding 3D mesh to represent a subset of the model's constituting points.

[5]The principal author's ResearchGate (Wei Li) profile lists no related research items, although none prior to 2013 appear. The author also does not appear in Google Scholar or the Web of Science.

Unlike Wei and colleague's approach, these points are collected by an expert operator on both the DM and a reference sample (Profico et al., 2019). In the field of Geometric Morphometrics (GM), upon which Profico and collegues' technique is based, point collection is done through landmark digitization. GM is a straightforward method that contributes to ease the use and representation of data and bears the potential to distinguish information that is strictly geometrical in nature (termed shape) from the influence of other factors, such as size, rotation, and translation (Zelditch, Swiderski, Sheets, & Fink, 2004).

The single individual to become the RM is selected from the sample based on how similar its geometry is to that of the DM. A measurement of this dissimilarity is, by default, given by Procrustes distance (Profico et al., 2019). Procrustes distance is defined as the linear distance between two landmark configurations in shape space. Shape space is the space occupied by landmark configurations when they have been transformed to represent object shapes. Shapes constitute an object's pure geometric information as represented by a landmark configuration encoded in a matrix whose values have been transformed to eliminate rotation, translation, and (when computing a full Procrustes superimposition) size (Zelditch et al., 2004).

The matrix transformation necessary to rigidly rotate and translate both fragments' landmark matrices (that is, without skewing or deforming the matrix (Palmas, Pietroni, Cignoni, & Scopigno, 2013)) are computed by means of a Generalized Procrustes Analysis (GPA). A GPA is a statistical procedure frequently used in GM that allows for the contrast of object shapes through Procrustes superimposition. The *dta()* tool superimposes both portions of the DM with the equivalent regions of the RM. To avoid errors introduced by asymmetry, both halves of the landmark sets in each fragment are symmetrized and the matrices are scaled independently.

In the Arothron package version 2.0.2 (Profico et al., 2018), Antonio Profico and colleagues' ((2019)) *dta()* tool requires a command syntax with at least nine arguments with which it makes it possible to compute the alignment of two disarticulated fragments. The following list provides a brief explanation of their use and the data supplied for every one of them to further explain the alignment procedure.

- *RM_sample* This argument introduces the reference sample data to the algorithm. The RM sample consists of an array whose elements are the matrices that list the 3D coordinates.

- *mod_1 and mod_2* The data structure assigned to the mod_1 and mod_2 variables typically consists of two separate numeric vectors that listed the numbers of the landmarks of that are present in one of the disarticulated fragments. These structures can be created by introducing an interval of sequenced values using the *c()* function in the R environment, provided that these landmarks are listed continuously in the DM matrix or matrices.

- *pairs_1* and *pairs_2* These arguments can optionally be filled with two separate two-column matrices listing left and right bilateral landmarks. Their use triggers an *"optional symmetrization process"* that can alter the results of the alignment (Profico et al., 2019). Should the user choose not to consider symmetry during the alignment of the fragments, these arguments can be declared *null* in the R system.

- *DM_mesh_1* and *DM_mesh_2* These arguments introduce the two separate 3D models of the DM to the function. These models are normally imported to the R environment at the beginning of the script.

- *DM_set_1* and *DM_set_2* These sets correspond to the elements in the DM array that store the coordinates of the landmark sets of each fragment.

Profico and colleagues' (2019) *dta()* software was tested by measuring the Procrustes distance between specimens (that is, the linear distance in shape space between two landmark configurations when, to minimize the sum of squares of the distance between corresponding landmarks, they are centered, rotated, and, when speaking of full Procrustes distance, scaled (Zelditch et al., 2004). The specimens under comparison were those where fragmentation was simulated and their "original", un-modified selves.

This was performed on three data sets. The first of these was a large cranium data set consisting of 313 sexed primate skulls from various genera, with which they analyzed the impact of sex and taxonomic status in the tool's performance. The second included 51 modern human individuals. In this case, all 51 of them were compared with their digitally aligned selves, while 11 were contrasted with manually reconstructed versions of themselves.

Finally, the authors created four digitally aligned versions of the incomplete Amud 1 *H. neanderthalensis* cranium. Like the Ndutu cranium, Amud 1 is missing a large portion of the facial skeleton, for which the distance between the preserved lower end of the maxilla and the rest of the fossil is uncertain. Its position was estimated by H. Suzuki and F. Takai in (1970). Profico and colleagues presented four alternative digital alignments using two different templates, namely the La Ferrasie 1 and Shanidar 1 crania, and using both fixed landmarks and *sliding surface semi-landmarks*.

Unlike fixed landmarks, surface semi-landmarks are evenly spaced points lying over a plane that are often sampled in tens or hundreds. Their employment is a widely used discretization procedure that allows to sample complex surfaces and curves which, although otherwise featureless, hold valuable morphological information. The reasoning behind their use follows the notion that, by definition, collecting the coordinates of discrete points on fossil specimens bares the loss of information in the spaces between such points (Bardua, Felice, Watanabe, Fabre, & Goswami, 2019).

In the case of Amud 1 their deployment allowed Profico *et al* to easily capture the curved surface of the frontal, parietal, occipital or temporal squamae, which in turn further informed their digital alignments. This approach is often regarded as a more convenient alternative to placing the few traditional instrumentally-defined fixed landmarks referencing these surfaces. For example, *euryon* is a fixed landmark found using an outside spreading caliper to locate the point where the cranial vault is widest on the surface of the parietals (White et al., 2012), a task that cannot be comfortably performed in a virtual setting, even when linear measurement tools are available, since the necessary manipulation of the 3D model often results tedious. The intended procedure for this purpose has thus become the application of said semi-landmarks.

Semi-landmark points are automatically placed and repositioned across specimens not only to save the examiner from an extenuating and error-prone task, but to ensure comparability and remove the arbitrariness from the decision of placing a measurement point that is only indirectly defined by its relationship with concomitant structures - a type III landmark in Bookstein's classification (1991 in Zelditch et al., 2004).

Nevertheless, it is notable that Profico and colleagues did not settle for a semi-landmark based reconstruction. Instead, they compared their four alternative reconstructions of Amud 1 with Suzuki and Takai's reconstruction. The authors concluded that the *dta()*-based Amud 1 reconstructions resulted only 3 mm different from the 1970 reconstruction, a result they were confident on since, when considering the results of the comparison between manual and digital alignments, the tool outperformed an anonymous expert's manual reconstruction.

However, perhaps the most interesting ramification of their work was what they extracted from the first of their tests, according to which using an RM of the same sex and taxonomic sta-

tus for the alignment of a given DM greatly improved the performance of the *dta()*. Nonetheless, a template of the corresponding sex and taxon may not always be available. In fact, the authors accept that selecting a proper template specimen can be problematic. Furthermore, it is notable that the did not test their software on other hominin skulls, among which taxonomical attribution may be contentious and morphological differences are expected to be different from primate and modern human samples. Fortunately, just like the authors selected the La Ferrasie and Shanidar exemplars for their alignment, the R environment offers the possibility of manipulating the tool to use any sort of template for this procedure, including a mean.

Avoiding the use of a template altogether brings its own set of problems. Within the field of the resolution of the reassembly problems, the alignment of fragments of an object of unknown or arbitrary shape, which is to say, without prior assumptions about its original geometry, is a category of its own. Venues in this class can be divided into those that avoid global registration problem by resorting to multiple constrains and those that contain optimization algorithms. While the first often resort to human input to enforce fragment matches, the latter are often fully automatic (Papaioannou et al., 2017).

An accessible option in the first of these is the one presented by Palmas, Pietroni, Cignoni and Scopigno at the IEEE Digital Heritage 2013 Exposition, which has been made available online as the Fragment Reassembler software (Palmas et al., 2013). In this software, an expert operator matches fragment pairs by inputting corresponding points along their broken surfaces. The software then reduces the square distance between corresponding points by computing the appropriate rotation and translation of the fragment 3D model via a global energy minimization function extensible to any given number of constraints, which is given by:

$$E = \sum (s_i^A - s_{i'}^B)^2 \cdot k_{(i,i')} \forall constraints (s_i^A, s_{i'}^B) \epsilon [1, n] \tag{1.1}$$

Where E stands for the energy term, $k_{(i,i')}$ is a user-definable stiffness factor determining the resistance of adjacency constrain $(s_i^A, s_{i'}^B)$ (the union between the corresponding points). The rigid transformation is thus calculated by:

$$E = \sum (R^A \cdot s_i^A + T^A - R^B \cdot s_{i'}^B + T^B)^2 \cdot k_{(i,i')} \tag{1.2}$$

Where R is a 3×3 transformation matrix and T is the translation vector. However, given the properties of the rotation matrices, the actual rigid transformation is only found after an iterative process. Error tolerance can also be adjusted by the user. Once the 3D model has been rotated and translated to its final position, the software can store the aligned model so that the operator can match it with subsequent fragments following a hierarchical strategy.

In 2016, Eleni Kotoula analyzed the ease of use of this method for aligning fragments along with other semi-automatic point-based alignment methodologies accessible through other popular softwares, such as MeshLab and 3ds Max. She concluded that the Fragment Reassembler presented the most efficient and straightforward option to reassemble late medieval coarse-worn archeological pottery (Kotoula, 2016; Eslami et al., 2020).

Fully automatic approaches to the alignment of adjacent fragments of arbitrarily shaped objects have also seen progress in recent years. However, their efficacy has been repeatedly antagonized by fragment wear. Since 2016, few works have been aimed at developing a wear-resistant matching criterion including some approaches assuming constant thickness (Eslami et al., 2020).

In 2017, Papaioannou and colleagues proposed a robust pipeline for the reconstruction and completion of arbitrarily sized and shaped 3D objects, which has been released as the Virtual

Repair and Measurement Workspace (VRMW) reassembly system software, part of the PRESIOUS European Union-funded project. The procedure's base is one of two mesh segmentation algorithms that discriminate between the irregular surface of fractures and the smoother external surfaces of the object. Unfortunately, heavily damaged fragments and fracture surfaces that have been smoothed down have resulted problematic. Being not a fully automatic method, the software allows the user to define certain parameters and even feature curves when the segments are not properly classified into external and fractured surfaces. Unfortunately, that approach is not applicable in this project due to bone surface deterioration suffered by the Ndutu cranium fragments.

1.6 Aims of this work

In light of the available tools reviewed on the past section, the production of an alternative digital reconstruction of the Ndutu cranium that, unlike Clarke's, has an explicit statistical basis is at hand. Based on its similitude with the case of the Amud 1 as treated by Profico and colleagues in (2019), the most appropriate resource for the estimation of the position of the disarticulated facial fragments of the Ndutu cranium relative to the preserved portions of the cranial vault and base is the *dta()* tool.

Reducing the uncertainty in the spatial relationships between the fragments that make up the Ndutu specimen, especially that of the disarticulated facial skeleton is key to improve our current interpretation of it. Such task can also contribute to approach a settlement of the argument regarding the Ndutu specimen's position among the Middle and Late Pleistocene hominins because it directly affects traits that have been discussed in the relevant literature, namely the magnitude and angle of the projection of the preserved elements of the facial skeleton and the cranial flexion.

In light of the versatility of the tool contemplated for this reconstruction (exposed in the previous section), the queries that hold the interest of this work are: *What would be the most accurate way to implement the* dta() *tool to estimate the position of the disarticulated fragments of the Ndutu cranium?*, and *What place would this statistically-based reconstruction bestow to it among the hominins of the Middle and Late Pleistocene?* Based on these open questions, I distinguish two main objectives in this proposal:

Objective 1

To determine the data and/or constrains that reduce the error in simulated reconstructions of each fragment in a sample of well preserved Pleistocene hominin crania using said digital alignment tool.

Objective 2

To ponder the consequences of this statistically informed reconstruction in terms of shape in comparison to a sample of well preserved Pleistocene hominin crania.

For the first of these aims I posit that the use of surface semi-landmarks alongside a mean shape based template in the landmark-based digital alignment of the fragments constituting the supra-orbital and facial skeleton of the specimens in a sample of well preserved Pleistocene hominin crania reduces the reconstruction error, thus providing the most accurate data and con-

strain combination. For the second objective I hypothesize that, considering the estimated magnitude and angle of the projection of the preserved elements of the facial skeleton and the cranial flexion, this procedure places the reconstructed Ndutu cranium among the specimens akin to the early sapient lineage in terms of shape.

Chapter 2

Materials and Methods

As mentioned on the first chapter of this work, the Ndutu cranium is composed of numerous fragments. Some of these are adjacent and articulate with each other along a specific fracture line or joint, and others do not. From the latter, most constitute individual fragments, while others, like the circum-nasal area and the left palate form continuous clusters of pieces that lack anatomical continuity with respect to other matched fragments. I henceforth call all of these *disarticulated fragments*.

Using a straightforward criterion, Clarke glued most adjacent fragments to each other along their matching fracture surfaces in 1990. However, a frequently omitted fact about the Ndutu cranium is that, even in its current reconstructed form, it is made up of eight different *parts*. Strikingly, in the pictures and illustrations of many publications (see Clarke, 1976; G. P. Rightmire, 1983; Clarke, 1990; Klein, 2009),the specimen is represented whole. In fact, none of the references consulted for this project addresses this fact directly. To the best of my knowledge, pictures of the Ndutu cranium in its disassembled form only appear in the second volume of Schwartz and Tattersall's (2005) "The Human Fossil Record" and in the University of Vienna Institute of Anthropology's Fossil Hominoid Digital Archive CD-ROM.

From the perspective of this project, this situation could not be further from trivial because it means that, before solving the alignment of the disarticulated fragments, there is another challenge to overcome: reassembling the adjacent cranium parts. Such a task is particularly challenging because these parts are separated by worn and unworn fractures and sutures. The procedures undertaken to reconstruct the Ndutu cranium are described in the following subsections. However, the acquisition of all of the 3D models is addressed first.

Only once these adjacent parts were reassembled, I was able to employ Profico and colleagues' (2019) *dta()* to solve the alignment of the unarticulated fragments of the Ndutu cranium, which is the main concern of this work. The procedure required the use of a sample of hominin crania whose morphological data was stored in an assortment of landmark matrices (dubbed the *RM sample* in the software's own lingo). As explained in Chapter 1, it was through the management of this data prior to the tool's actual deployment that alternative reconstruction candidates were generated. In the following subsections I detail the procedure that I followed to obtain and refine these data. Subsequently, I describe the conditions in which the *dta()* function was deployed.

2.1 Disarticulated Model Preparation

2.1.1 Digital Asset Acquisition

To produce a 3D model of the constituting parts of the Ndutu cranium I employed the *.TIFF format images found in the "Ndutu" CD-ROM of the University of Vienna Institute of Anthropology's Fossil Hominoid Digital Archive purchased by the Institut Català de Paleoecologia Humana i Evolució Social (IPHES). These images correspond to the independent CT scans of the each of the eight parts into which the Ndutu specimen is split. They were obtained by the institute under collaboration with the Tanzanian Department of Antiquities and members of the INDABA group (Weber et al., 2005). The use CT scans allowed me to digitally free the constituting fragments in each part from the plaster added by Clarke by means of an image processing software. The chosen software was Materialise Mimics Medical version 20.0.0.691 (Materialise NV, 2017).

Once imported through the New Project Wizard, I adjusted the scan resolution to match the original pixel size as reported in the fourth column of the "TIFF files in this CD-ROM:" table of the "CT slices in TIFF-format" page of the "start-here.htm" file stored in the "Ndutu" CD-ROM. I entered the reported voxel size values in the X and Y input boxes and selected millimeters as the measurement unit. After visually examining the CT slices, I adjusted the orientation in the Change Orientation dialog box. Once the CT scans were fully loaded in the software, I proceeded to segment them (i.e., to partition the image data using a parameter (Mah & Caldwell, 2008), in this case, one related to density). This was conducted using the Threshold function and the product was a mask (a 3D mesh of the structures that fit the density parameter). Minimum and maximum threshold values were also adjusted manually on each part to remove the plaster. The resulting 3D models were exported in Optimal quality in Stanford's Triangle (PLY) format. Regardless, even when the procedure followed to generate each fragment's 3D model was essentially the same, models with differing vertex counts were exported due to the different voxel sizes used during the CT scanning process.

After the plaster had been removed, the disarticulated fragments of the Ndutu cranium's facial skeleton, were further separated into distinct 3D models. The separation was performed using the MeshLab version 2020.12 3D mesh processing software (Cignoni et al., 2008). Discontinuous parts of the 3D model were split from each other by using the Split in Connected Components option found in the context menu that can be opened by right clicking a layer in MeshLab's Layer Dialog.

This action resulted in the production of several layers, each containing from a single, small, disarticulated fragment to a large cluster of them. To isolate each fragment cluster, all other layers were deleted from the MeshLab project using the Delete current mesh option of the same context menu. When necessary, I merged the isolated cluster back together with any small featureless adjacent fragments by right clicking and selecting Flatten visible layers. The resulting 3D mesh was then exported in *.PLY format. This process was repeated until all disarticulated fragments had been put into separate files. However, for comparison purposes, a copy the 3D model of CT-scan 1 (the joint Ndutu facial skeleton and frontal bone fragments as reconstructed by Clarke) was kept and labeled "Ndutu_C". Table 2.1 lists the continuous fragment clusters comprised in the digital specimen of the Ndutu cranium as employed in this project's reconstructions, along with the part that they were originally attached to in the "Ndutu" CD-ROM, their identification, and adjacent fragment clusters.

Table 2.1: Number, disarticulated model part, identification, and adjacent clusters of the fragments or fragment clusters of the Ndutu cranium. [1] As in Clarke, 1990, nomenclature as in White, Black and Folkens, 2012. [2] In Clarke, 1990.

No.	CT-scan	Identification [1]	Adjacent to clusters [2]
1	1	Left circum-nasal area, medial wall of the right orbit, and anterior portion of the left palate, with a disarticulated fragment of the right upper lateral border of the nasal aperture.	Disarticulated
2	1	Left lateral supraorbital.	Disarticulated
3	1	Right lateral frontal squama and fused lower anterior right parietal, right greater wing of the sphenoid, lower anterior temporal, and a disarticulated fragment of the left lesser wing of the sphenoid.	5, 9
4	1	Left lateral frontal squama fragments of the upper posterior and (disarticulated) lower posterior lateral surface of the left greater wing of the sphenoid, squamous and mastoid portions of the right temporal.	5, 8
5	2	Left and right parietals (excluding the anterior third of the left one and the antero-medial portion of the right one), including several disarticulated inner and outer tabula fragments.	3, 4, 8, 9
6	3	Upper medial occipital squama, including the lambdoid angle.	5, 7, 8
7	4	Single fragment of the left upper lateral occipital squama.	5, 6, 8
8	5	Restored occipital bone including the nuchal plane, the base of the occipital planum, and the posterior and right lateral borders of the foramen magnum, fused to the mastoid portion of the right temporal.	4, 5, 6, 7, 9, 10
9	6	Right temporal squama	3, 5, 8
10	7	Anterior and left lateral borders of the foramen magnum.	8
11	8	*Unmatched* parietal fragment cluster.	Disarticulated

2.1.2 Articulated Fragment Reassembly

As clarified in the previous section, before reconstructing the position of the Ndutu cranium's facial skeleton, the first problem that needed to be addressed was the reassembly of articulating fragments of the cranial vault and base. Attending to the purpose of comparing this project's reconstruction with the previous one, this crucial preliminary step had to be carried out twice, once with fragments 3 to 10, and again using fragments 5 to 10 along the Ndutu_C 3D model. This second iteration would allow to produce a full, plaster-free 3D model of the Ndutu cranium recreating Clarke's reconstruction.

To resolve both reassembly problems an important consideration was that, as mentioned before, the Ndutu cranium's adjacent fragments are split from each other along complex fractures and sutures. This confers the frontier between each pair of clusters a distinctive morphology. Unlike potsherds, the surfaces of some fractured bones may have become rugous due to erosion, while others possess smoother profiles. Other parts of a disarticulated cranium, however, may be sinuous, like the conspicuously irregular articular surface of a suture joint. Such scenarios are admittedly challenging (to say the least) for most of the automated reassembly software available, even (or perhaps specially) for those employing state of the art *machine learning* methods (Papaioannou et al., 2017).

Therefore, considering its proven ease of use (Kotoula, 2016), which adds to its accessibility and convenient lack of assumptions, I deemed Palmas and colleagues' (2013) Fragment Reassembler software version 1.0 the most adequate tool for the assembly of the adjacent fragments of the Ndutu cranial vault and base. This software allowed to match the fragment fragment clusters following a hierarchical strategy. Using the default values for the stiffness factor and error tolerance (1 and 0.001, respectively), adjacent fragment clusters were matched considering the following criteria:

1. Fracture surface correspondence

2. Part position as reported by the photographs in Clarke (1990).

These matches were enforced by applying a several point pairs on the surface of sutures and fractures. Priority was given to fragment clusters with more match candidates. Consequentially, I selected fragment cluster No. 8 as the base for the reconstruction, given that it constituted the cluster with the largest number of adjacent fractured fragments according to the images in Clarke (1990).

For each fragment, I produced a preliminary alignment by distributing a minimum of four pairs of points along each of the fracture surfaces. I later corrected this using the software's many tools. Once the alignment appeared correct, I grouped the fragment pair and proceeded to assemble another one. Following this procedure, I constructed an assembly hierarchy. Following (Palmas et al., 2013), to better illustrate this method, a constrains graph is presented in Figure 2.1.

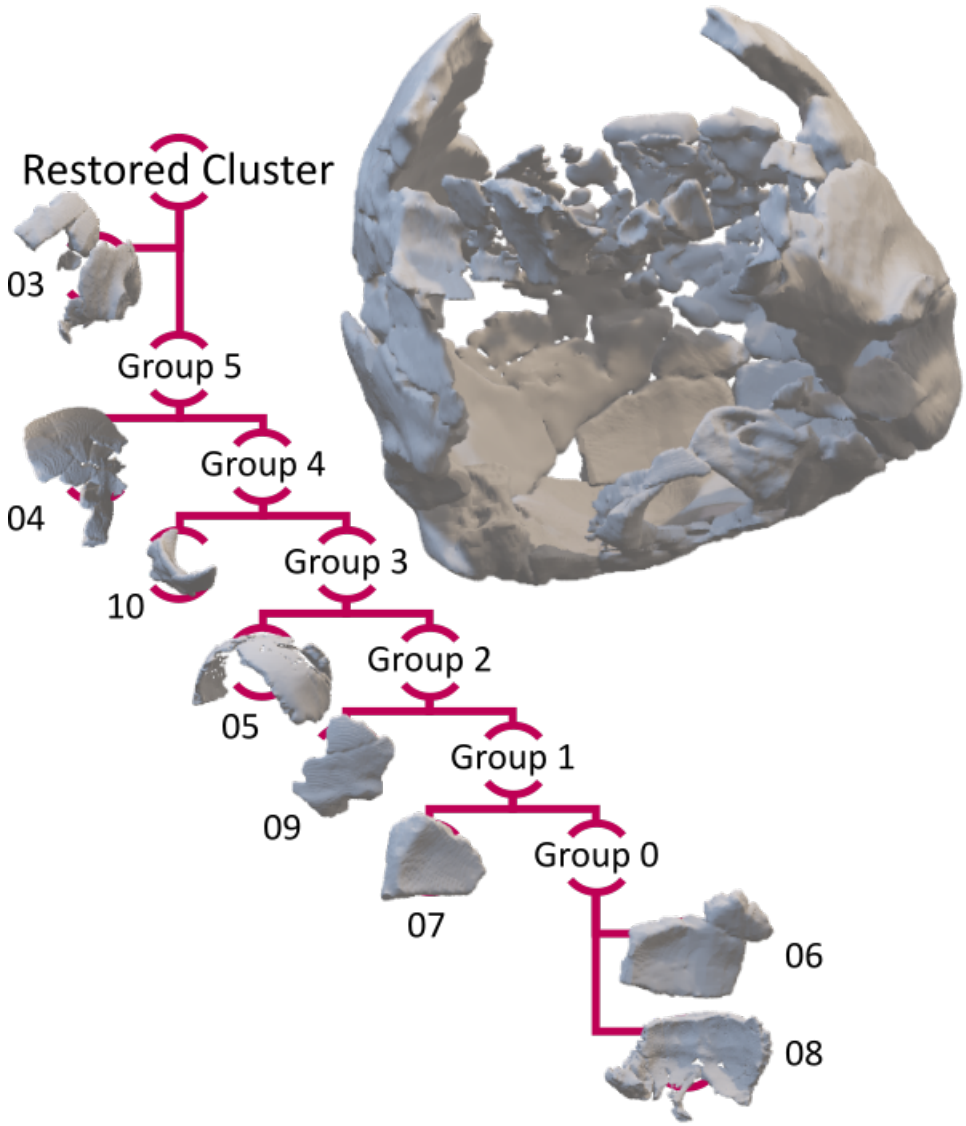

Figure 2.1: Constrains graph for the reassembly of the Ndutu cranial vault and base fragment cluster.

The Fragment Reassembler software allows to assess fragment alignments in various ways. On one part, overlapping faces are colored red to indicate 3D mesh penetration. On the other, the color of the point pairs and the lines (edges) connecting them, which ranges from blue to green, to yellow, red and dark red, indicates the proportion of the residual energy resulting from the global energy minimization function that remains (Figure 2.2). It is noteworthy that the software assumes an initial state of 100% before the alignment is solved (therefore the software may sometimes report more than 100%). This percentage is reported in the Graph modification area of the user interface. Therefore, while a blue colored edge or point indicates that the alignment optimally favors that connection between point pairs, too many dark red edges with percentages over 100% denote an improper alignment. Additionally, similarly colored bands covering some larger regions of the 3D mesh indicate varying degrees of deformation caused less than perfectly rigid transformation (Palmas et al., 2013).

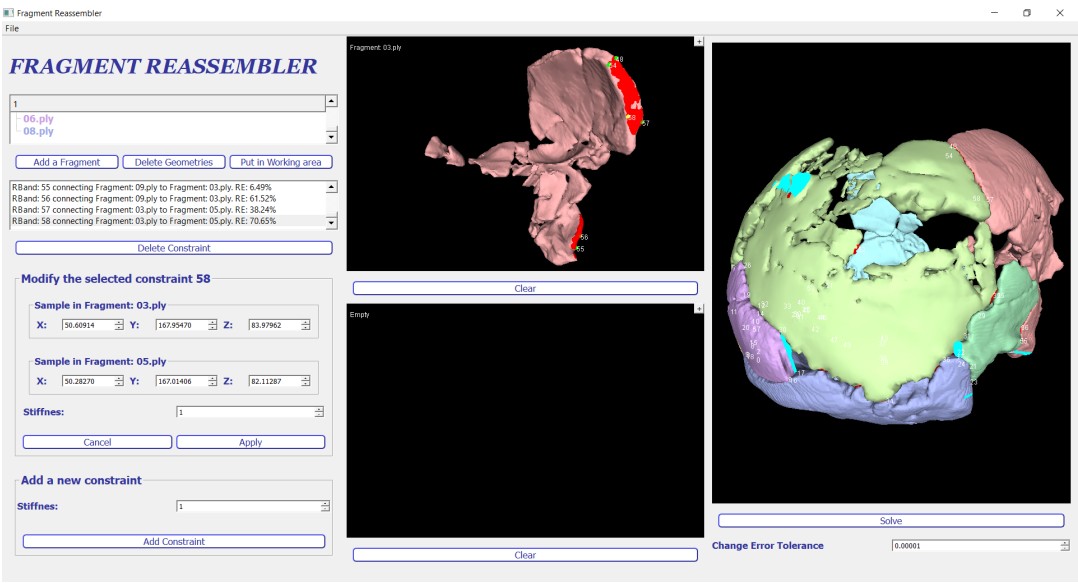

Figure 2.2: Reassembly of the adjacent cranial fragments of Ndutu in the Fragment Reassembler software.

According to Palmas and colleagues (ibid.), many of these issues can be amended by adding more point pairs and replacing others with better located ones. It is also unnecessary to be absolutely accurate when placing point pairs, since a single alignment does not depend on one particular pair of points. In practice, this means that the user may add as many points and distribute them as widely as he or she desires and the software will attempt to find a rigid transformation that satisfies them.

The selection of points may be refined whenever necessary, throughout the entire process. In consequence, pair by pair, I added points on the surfaces of the fragments. Whenever the software's interface indicated no improvement in terms of mesh penetration and residual energy, improperly placed point pairs were deleted.

During the hierarchical reassembly process, when a fragment is matched with a group, energy minimization is not performed across all fragments, but only between the group (taken as if it were a whole) and the new fragment. This means that as groups that include other subgroups are formed, each subgroup inherits the residual energy values that resulted from aligning its constituting fragments. Thus, if left grouped, the energy minimization function would never be applied across all the fragments and the alignment would not be optimized. Consequentially, I deleted the hierarchy and solved the alignment globally. This is an expected step explained by Palmas and colleagues in their (2013) publication. The software allows to delete the groups formed by matched pairs of fragments by selecting Split in the group context menu.

I performed an initial global energy minimization after which any constraint accumulating a percentage of residual energy greater than 100%, was deleted from the final reconstruction. Once the most problematic point pairs were eliminated, I ran the energy minimization algorithm again to produce a final reassembled fragment cluster.

2.2 Reference Model Sample

The reference sample comprised 26 hominin crania from the Early, Middle and Late Pleistocene epochs that were obtained from various sources. Eleven of them, consist of 3D models of

hominin fossil specimens, which were generated through photogrammetry (ten of them were processed by me, while the Zhoukoudian III specimen was processed by Carlos Lorenzo, PhD (IPHES, URV) during a personal demonstration session; for more details see Subsection 2.2.1).

Ten of these replicas are housed at the IPHES Paleoanthropology Laboratory and one (a high-resolution replica of D2700) was a personal communication of Jordi Agustí, PhD. (IPHES, URV). Six other models were downloaded from two online repositories, namely AfricanFossils.org and Morphosource.org. The remainder were delivered personally by both Carlos Lorenzo, PhD., and Florent Détroit, PhD. (Histoire naturelle de l'Homme préhistorique UMR 7194, MNHN). The data of three of these were supplied in the form Mimics project files and their corresponding data. Masks were exported following the same procedure reported in Subsection 2.1.1. Specific information of the specimens in the reference sample is summarized in Table 2.2.

Table 2.2: Specimen name, archaeological site of recovery, data and source of the specimen 3D models in the reference sample. [1] *From Klein, 2009, unless otherwise noted.*

Specimen name	Site [1]	Data	Source / Copyright holder
Amud 1	Amud, Israel	Still images (Photogrammetry)	Replica at IPHES
D2282	Dmanisi, Georgia	Still images (Photogrammetry)	Replica at IPHES
D2700	Dmanisi, Georgia	Still images (Photogrammetry)	Personal communication, Jordi Agustí
D4500	Dmanisi, Georgia	Still images (Photogrammetry)	Replica at IPHES
Dali	Dali, Shaanxi, China	3D model	Personal communication, Florent Détroit; ©MNHN
Gibraltar 1	Forbes' Quarry, Gibraltar, UK	CT scan	Personal communication, Carlos Lorenzo; ©NESPOS
BOU-VP-16/1 (Herto)	Bouri Fm., Middle Awash, Ethiopia	Still images (Photogrammetry)	Replica at IPHES
Irhoud 1	Djebel Irhoud, Morocco	Still images (Photogrammetry)	Replica at IPHES
Kabwe	Kabwe, Zambia	3D model	Morphosource.org, ©Duke University
KNM ER 1470	Koobi Fora, Kenya	3D model	AfricanFossils.org
KNM ER 1813	Koobi Fora, Kenya	3D model	AfricanFossils.org
KNM ER 3733	Koobi Fora, Kenya	3D model	AfricanFossils.org
La Chapelle-aux-Saints	La Chapelle-aux-Saints, France	3D model	Personal communication, Florent Détroit; ©MNHN
LF1	La Ferrassie, France	3D model	Personal communication, Florent Détroit; ©MNHN
LB1	Liang Bua, Flores, Indonesia	3D model	Personal communication, Florent Détroit; ©Pusat Arkenas

Lesedi 1	Rising Star, Cradle of Humankind, South Africa (Hawks et al., 2017)	3D model	Morphosource.org; ©University of the Witswatersrand
Sima de los Huesos 5 (Miguelón)	Atapuerca, Spain	Still images (Photogrammetry)	Replica at IPHES
Mladeč 1	Mladeč caves, Czech Republic	CT scan	Personal communication, Carlos Lorenzo; ©University of Vienna
Circeo 1	Monte Circeo, Italy	3D model	Personal communication, Florent Détroit
Petralona 1	Petralona cave, Greece	Still images (Photogrammetry)	Replica at IPHES
Qafzeh 9	Qafzeh cave, Israel	Still images (Photogrammetry)	Replica at IPHES
Sangiran 17	Sangiran, Java, Indonesia	3D model	Morphosource.org, ©Duke University
Shanidar 1	Shanidar, Iraq	Still images (Photogrammetry)	Replica at IPHES
Skhul 5	Skhul cave, Israel	3D model	Personal communication, Carlos Lorenzo; ©Peabody Museum
Steinheim	Steinheim an der Murr, Germany	CT scan	Personal communication, Carlos Lorenzo
Zhoukoudian III	Zhoukoudian Locality 1, Beijing, China	Still images (Photogrammetry)	Replica at IPHES

2.2.1 Digitization

Photogrammetry is a technique that allows to produce measurements, including distances, heights, coordinates, areas, and volumes, from still images. With the appropriate equipment and software, one can generate 3D point clouds that can be used to create surface or object models (Aber, Marzolff, Ries, & Aber, 2019). Agisoft Photoscan is an image-based 3D modeling software that uses this principle to produce a 3D model of the outer surface of a given object. We followed this software's User Manual's isolated object capturing scenario recommendations to capture the images of the hominin cranial specimen replicas.

The replicas were placed on a low table over a white cloth with a 5cm scale in front of them at the IPHES Paleoanthropology Laboratory. Pictures were taken with a Canon EOS 2000D reflex camera at 50 mm focal length, at 1"6 shutter speed, with an indirect light source (the laboratory's left side lights) during the day. The exposure (ISO) was adjusted between 200 and 400 as necessary to compensate for daylight intensity changes in between specimens. A tripod was used for camera stabilization and positioning.

I captured 34 to 36 images of the upside and the underside (70/72 in total) of each specimen following a three-step per side capturing strategy. By moving the tripod and camera around the specimen, I first took 16 pictures every 22.5° at table level. 16 more were taken with the legs of the tripod partially extended, and the camera at approximately 1.5m from the floor. Finally,

two to four more pictures were taken with the tripod legs fully extended and the camera almost directly over the specimen. The replica was then flipped upside down and a plasticine support was placed under it for stabilization. The image capturing process was then repeated. Figure 2.3 depicts Agisoft Photoscan's rendering of the specimen point cloud along with the estimated positions of the cameras, which in a way illustrates this image capturing strategy.

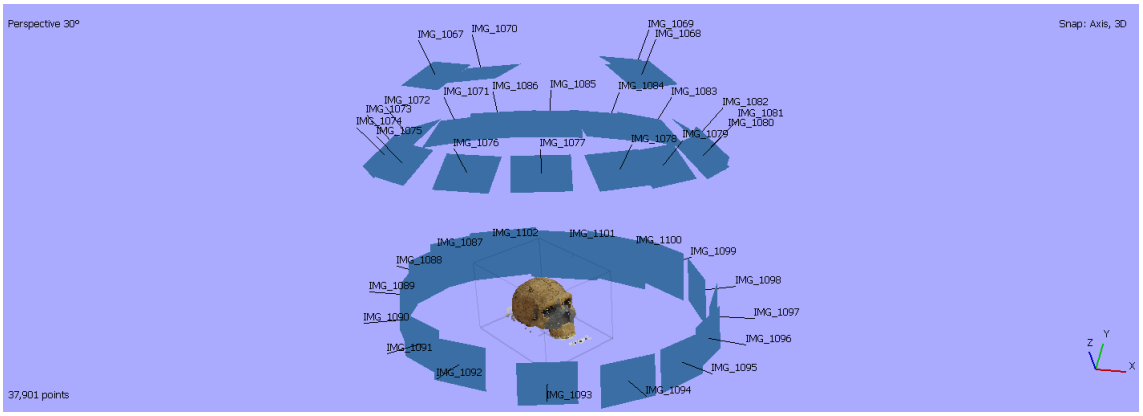

Figure 2.3: Model View of the Agisoft Photoscan Professional software version 1.40 build 5076 during the creation of the Amud 1 replica 3D model.

The images were processed in Agisoft Photoscan Professional version 1.40 build 5076 (Agisoft LLC, 2017). In this software, most of the functions needed to generate a 3D model are conveniently found under the *Workflow* menu. The pictures were loaded into a new project using the *Add Photos...* function. Pictures from the upside and from the underside of the replica were loaded into different chunks.

For each chunk, the images were aligned, and a point cloud was created using the *Align Photos...* and *Build Dense Cloud...* functions, respectively. The dense cloud was built using *High* quality settings. Undesired points, including artifacts and anything other than the replica, were removed manually from this point cloud using the *Free-Form Selection* tool found in the main toolbar.

Once both dense clouds were clean, three common markers were defined by right-clicking on three separate points visible in both point clouds in the *Model View* and selecting *Add Marker* in the context menu. The scale of the 3D model was also defined following a similar process. Beginning with one of the images of one of the chunks, I added two more markers on both ends of the scale. Then I placed the same markers in the same order on another of the images of the same chunk using the Place Marker option in the context menu. Afterwards, I selected those points in the *Workspace Panel*, right clicked on them to display the context menu, selected *Create Scale Bar* and then entered the real distance (0.05 m) in the *Distance (m)* column of the *Scale Bars* subpanel of the *Reference* panel.

Once a total of 8 markers had been added on both chunks, the dense clouds were aligned using the *Align Chunks...* function based on the first three common markers, and later merged with the *Merge Chunks...* function. The merged dense cloud was then used as a base for the 3D mesh by using the *Build Mesh...* function. The surface type was set to *Arbitrary (3D)* following the User Manual recommendations and the face count to *High* in the *Build Mesh* dialog box. When necessary, the mesh was cleaned further using the same *Free-Form Selection* tool. Finally, I constructed a texture using the *Build Texture...* option. The mapping mode was set to *Generic* and the blending mode to *Mosaic* in the corresponding dialog. The *.PLY

3D model file and a *.JPEG texture image file were created with the *Export Model...* function found under *File > Export*.

Additional 3D Model Preparation

The 3D models in this project had varying complexities. Because CT scan slices carry data about the internal structures of specimens, those resulting from CT scans contained more information than those generated from photographs. Although as it has been mentioned in Chapter 1, some endocranial structures have been shown to be correlated with the facial skeleton position relative to the cranial vault and base, hominin crania CT scans are unfortunately hard to come by. Thus, simplifying the 3D models – that is, removing the parts of the mesh that represented the endocranial anatomy and other internal structures – was a necessary step prior to using them.

This removal was performed in MeshLab 2020.12 (Cignoni et al., 2008). By using the *Z-painting* tool, I colored the outer surface of the 3D meshes generated from CT scans. Then, I opened the *Select Faces by Color* dialog box to select the colored surface by clicking *Filters > Selection > Select Faces by Color*. Once in this dialog box, I selected the corresponding color in the *Pick a Color* box that displayed after clicking on the colored bar next to *Color to Select*. After hitting *Apply*, I moved the newly selected surface to another layer by means of the *Move selected faces to another layer* option found in the context menu that opens when right clicking a layer in *Layer Dialog*. Subsequently, I deleted the original mesh with the *Delete current mesh* function of this same context menu. The resulting 3D model was exported in *.PLY format following the same procedure as in Section 2.1.1.

Another previous step was adjusting the scale. One of the downsides of 3D models generated through photogrammetry is that once exported and used in another software scale information is often lost. Therefore, all these 3D models had to be re-scaled before performing any part of the analysis – that is, picking any landmarks, for example. For this, I again resorted to the Agisoft Photoscan project file where the 3D model had already been put to scale to obtain a reliable measurement between two constantly preserved landmark points: *lambda* and the right *asterion*. The distance between these same points was then measured in MeshLab and the obtained value was divided by the one reported by Photoscan. Through this simple calculation, I obtained a scalar value to introduce in any of the axis input fields of the *Transform: Scale, Normalize* dialog box found under *Filters > Normals, Curves and Orientation > Transform: Scale, Normalize* in MeshLab.

Distances in the resulting meshes were thus reported in centimeters, as they are in the Photoscan software. Although this complicated scaling procedure was only undertaken in the 3D models obtained through photogrammetry, I also adjusted the scale of some of the other 3D models, whose dimensions were usually expressed in mm. A 0.1 scalar factor was used in these cases.

Finally, to compensate for unpreserved morphology, a few of the specimens were mirrored. Mirroring is straightforward reconstructive procedure that uses bilateral symmetry to approximate missing elements by creating a reflected image of their counterpart (Lautenschlager, 2016). For Gibraltar 1, which is missing most of the left neurocranium, I exported from Agisoft Photoscan a mask consisting of a merge of two parts: a smoothed version of the original specimen and a midline mirror projection of it – together these parts form a symmetrical reconstruction of the Gibraltar 1 cranium as reconstructed by Carlos Lorenzo.

2.2.2 Landmark Registration

To capture the morphology of the specimens in the sample and that of the fragments of the Ndutu cranium, a total of 37 craniometric landmarks were collected using the *Pick Points* tool in the MeshLab version 2020.12 software (Cignoni et al., 2008). The employment of this program allowed to secure the appropriate display of the textures generated in Agisoft Photoscan (Agisoft LLC, 2017), so that they could be used as a visual aid during the collection of the landmarks.

In MeshLab, while in *PickPoints* mode, each specimen was moved and oriented by pressing the [Esc] key and then using the left mouse button to drag the mesh. When necessary, double-clicking was used to focus the camera in a more convenient position. Once the desired landmarks were visible, I pressed the [Esc] key again and right clicked on their position to register their 3D coordinates. Landmark data was saved to a MeshLab Picked Points (*.PP) file by clicking on the Save button in the Form dialog once all the coordinates had been registered.

The 37 landmarks in this study were selected based both on their presence in the Ndutu cranium's fragments and in most of the sample. To ease the handling of the information regarding the presence or absence of the landmarks in the sample a short computer program (an R script; see Appendix A) was composed in RStudio 1.4.1717 and executed in the R statistical system version 4.0.5 (R Core Team, 2020). This allowed to produce the final set of landmarks presented in Table 2.3.

The landmarks in a larger preliminary set were picked in MeshLab using the method detailed previously. The lines in the script allowed to import this data into the R environment. They also made it possible to count the number of specimens where each landmark was missing and print this information in the screen. By introducing a decimal threshold value, the program eliminated all landmarks missing from more than four specimens. The final output of the script was a list of landmarks that were guaranteed to be present on most of the specimens in the sample.

Most of the landmarks both in the preliminary and final set were founded on the definitions in White, Black and Folkens' (2012) "Human Osteology" book, which themselves are built on those in Martin and Saller's (1957) "Lehrbuch der Anthropologie". Still, one of the shortcomings of White, Black and Folken's extensive landmark list is the lack of points that record dental arcade shape and supraorbital margin curvature. Therefore, additional landmarks were taken from Stelzer and colleagues' (2019) study on the evolution of the dental arcade shape and size in Middle Pleistocene hominins, as well as from McNulty's (2005) work on the variability of the supraorbital regions of Eurasian Miocene hominoids. Considering Rightmire's (1983) arguments, I also replaced and supplemented the few landmarks recording the temporo-mandibular joint morphology in White, Black and Folkens' list with the more numerous of Smith et al's (2013) publication dealing with the ontogenetic variation of this surface in modern *H. sapiens*.

Table 2.3: Number, code , name and definition of the landmarks in this study. [1] From White, Black and Folkens, 2012, unless otherwise noted.

No.	Code	Name	Definition[1]
1.	BM2_L	Left buccal M2	Left most buccal point in the upper second molar alveolus cervical) margin (Stelzer et al., 2019)
2.	BM1_L	Left buccal M1	Left most buccal point in the upper first molar alveolus cervical) margin (Stelzer et al., 2019)

3.	BP4_L	Left buccal P4	Left most buccal point in the upper second premolar alveolus cervical) margin (Stelzer et al., 2019)
4.	BP3_L	Left buccal P3	Left most buccal point in the upper first premolar alveolus cervical) margin (Stelzer et al., 2019)
5.	LM1_L	Left lingual M1	Left most lingual point in the upper first molar alveolus cervical) margin (Stelzer et al., 2019)
6.	LP4_L	Left lingual P4	Left most lingual point in the upper second premolar alveolus cervical) margin (Stelzer et al., 2019)
7.	LP3_L	Left lingual P3	Left most lingual point in the upper first premolar alveolus cervical) margin (Stelzer et al., 2019)
8./9.	ALA_L/R	Left/right *alare*	Most lateral points along the margin of the nasal aperture
10./11.	CGO_L/R	Left/right *zygoorbitale*	Points of intersection between the zygomatico-maxillary suture and the lower orbital rim
12.	MSO_L	Mid-torus inferior	Point in the middle of the inferior margin of the left supra-orbital torus (McNulty, 2005)
13./14.	MXF_L/R	Left/right *maxillofrontale*	Points of intersection of the axis of the anterior lacrimal crest and the fronto-maxillary suture
15.	NAS	*Nasion*	Intersection between the inter-nasal and fronto-nasal sutures
16.	FMO_L	Left *frontomalare orbitale*	Intersection of the left lateral orbital rim and the fronto-zygomatic suture
17.	FMT_L	Left *frontomalare temporale*	Intersection of the left temporal line and the fronto-zygomatic suture
18.	FRT_L	Left *frontotemporale*	Most antero-medial point on the left temporal line
19./24.	SPH_L/R	Left/right *sphenion*	Point of intersection between the parieto-sphenoidal, parieto-temporal, and spheno-temporal sutures (Martin & Saller, 1957)
20./25.	FIS_L/R	Left/right superior infra-temporal fossa	Bilateral point where the infra-temporal crest is intersected by the spheno-squamosal suture (Smith et al., 2013)
21./26.	POR_L/R	Left/right *porion*	Upper- and outermost point on the margin of the external acoustic meatus
22./27	AST_L/R	Left/right *asterion*	Points of intersection between the lambdoid, parieto-mastoid and occipito-mastoid sutures

23.	STE_R	Right *stephanion*	Intersection between the right temporal line and the coronal suture
28.	LAM	*Lambda*	Intersection of the sagittal and lambdoid sutures
29.	INI	*Inion*	Midline point projected where the superior nuchal lines meet
30./34.	PGL_L/R	Posterior glenoid point	Inferior-most point of the post-glenoid process (Smith et al., 2013)
31./35.	LGL_L/R	Lateral glenoid point	Point on the lateral margin of the articular surface of the temporo-mandibular joint (point of inflection of the braincase) (modified from Smith et al., 2013)
32./36.	AGP_L/R	Anterior glenoid point	Anterior-most point in the articular surface of the temporo-mandibular joint (Smith et al., 2013)
33.	EGL_L	Left entoglenoid process	Inferior-most point on the left entoglenoid process (Smith et al., 2013)

The landmarks on this list were collected on each of the specimens in the RM sample, on each of the fragments of the DM, and on the Ndutu_C recreation. This was repeated five times on the DM and RM models to allow for the validation of the landmark registry process (see Section 2.3.4) needed for the alignment. The point coordinates were stored in MeshLab *.PP files as explained previously after each iteration. A total of five *.PP files were generated for each specimen and fragment. The data was stored in two separate folders (directories), one called "Reference" for the sample, and another called "Target" for the fragments. The naming of the files followed a strict naming protocol to facilitate their identification and classification within the environment of the statistical analysis software used. The iteration number, followed by a dash and the specimen number was used in the RM sample. In the DM, the specimen name (Ndutu) was followed by an underscore and two letters indicating the anatomy represented by each fragment.

In the case of this reconstruction, the order in which the landmarks were collected did not consider their representation on either fragment. Instead, ease of collection in the RM sample was prioritized, which resulted in them being numbered bottom to top, front to back, and left to right across the dental arcade, face, and cranial vault, while they are arranged back to front and left to right in the cranial base. The coordinates of the landmarks of each fragment were also stored in different *.PP files, since they were collected on different sessions. The landmarks not represented on each fragment were simply filled with zeros by the MeshLab software. This ensured the matrices resulting from these *.PP files would have the same length.

2.3 Digital Alignment

2.3.1 R system packages

R (R Core Team, 2020) is an Open-Source statistical computer system consisting of a programming language and run-time environment with several system functions and utilities that make

some arithmetic computations and statistical description, analysis, and graphing possible without the need of installing additional software. The functions, typically referred to as the R base, constitute a versatile resource for data processing.

However, the system's functionality can be extended by the installation of software add-ons composed (coded) in the system's language, known as packages (Hornik, 2020). Conventionally, the packages needed to run the functions in a script are listed at the beginning. In the following paragraphs, I follow this convenient arrangement to introduce the packages that the scripts resort to.

As explained briefly in Chapter 1, the *dta()* tool is a function that is part of Arothron R package composed by Antonio Profico, Costantino Buzi, Silvia Castiglione, Marina Melchionna, Paolo Piras, Pasquale Raia, and Alessio Veneziano (2018). Besides Arothron, the functions in two more packages were fundamental for the realization of this reconstruction.Such packages consist of GM toolsets, most of which perform analogous tasks. One of them is Schlager's (2017) Morpho package version 2.8, which is a code that allows to analyze 3D mesh and landmark data through a large collection of functions. A remarkably similar one is Adams and colleagues' (2021) Geomorph package, which makes it possible to carry out various tasks related to the digitization, manipulation, analysis and graphing of 2D and 3D landmark data with functions that, in some cases, require a shorter command syntax. These packages import functions from many other R packages, including each other.

Additionally, prior data management also resorted to functions in extensions such as plyr (Wickham, 2011), a package dedicated to data partitioning and function deployment, readr (Wickham, Hester, & Francois, 2017), a package designed to read rectangular data (like *.CSV files), and rgl (Murdoch & Adler, 2021), a 3D interactive graphics package. The analysis of method variable effects and interactions additionally required the use of the tidyverse (Wickham et al., 2019), and rstatix (Kassambara, 2021) packages.

The entire data processing and function implementation steps needed for the reconstruction were coded in an R script in RStudio titled "Blue.R". This script (which should allow for the data processing for the unarticulated fragment reconstruction procedure to be replicated or implemented on another reconstruction problem interactively) can be found in Appendix B. Prior testing was performed using the lines in the "Bottlenose.R" script, which is a modification of "Blue.R", and can be found in Appendix C.

2.3.2 Data import

To load the data into the R system, I entered the location of the directory where the DM and RM sample landmark data was stored to create a list of files to be imported. I also provided information regarding the number of repeated measurements contained in the folders to allow the script to distinguish between different landmark data sets of the same individual.

The import was achieved by implementing Morpho's *read.mpp()* function. This function reads the lines in the *.PP file and stores it in a matrix (one of many available R data structures) that preserved landmark names. When applied to a list containing file locations through the *lapply()* function, *read.mpp()* stores the data of each file in a matrix within a list of matrices. Four file lists and four data structures were created in this way. The fifth measurements of each specimen in the RM sample and fragment in the DM were saved in two lists of matrices, while the entire collection of repeatedly measured specimens and fragments were saved in a second pair.

Several functions, conditions and loops were coded to create an intelligible raw landmark

data structure that could be used as a guide before the data were further manipulated. For instance, the *names()* function used the information in the file list to name each of the matrices after each specimen in the RM sample. The columns in the matrices were also named x, y an z all at once using the *colnames()* function. Subsequently, all missing values, denoted in the MeshLab *.PP as 0.00000 values were replaced with NA, which allowed the functions in the loaded packages to accurately recognize them as unknowns. A condition (*if ()*) was created to detect values replaced with NA to allow R to print out a recount of the few landmarks still missing from some of the specimens. Finally, considering that some functions demand that the data is stored in array form (a $k \times l \times m$ data structure composed of a vector whose listed elements have $k \times l$ dimension attributes, very much like a list of matrices (R Core Team, 2020)), the information in each row of each matrix was copied to each row in the array. To mend that landmark names were lost in this process, the *rownames()* function was used to store the landmark names in the original data in a list called *varname*.

2.3.3 Missing landmark estimation

As explained in the previous section, the first lines in the "Blue" R script allowed to detect missing landmarks based in the value assigned to them by the MeshLab software ("0.00000"). Substituting this value with NA, made it possible to count and output the number of specimens missing each particular landmark as follows:

```
[1] "Warning: Landmark BM2_L (No. 1) is missing from 1 specimens."
[1] "Warning: Landmark BM1_L (No. 2) is missing from 1 specimens."
[1] "Warning: Landmark BP4_L (No. 3) is missing from 0 specimens."
[1] "Warning: Landmark BP3_L (No. 4) is missing from 1 specimens."
[1] "Warning: Landmark LM1_L (No. 5) is missing from 1 specimens."
[1] "Warning: Landmark LP4_L (No. 6) is missing from 1 specimens."
[1] "Warning: Landmark LP3_L (No. 7) is missing from 1 specimens."
[1] "Warning: Landmark ALA_L (No. 8) is missing from 0 specimens."
[1] "Warning: Landmark ALA_R (No. 9) is missing from 1 specimens."
[1] "Warning: Landmark CGO_L (No. 10) is missing from 1 specimens."
[1] "Warning: Landmark CGO_R (No. 11) is missing from 1 specimens."
[1] "Warning: Landmark MSO_L (No. 12) is missing from 0 specimens."
[1] "Warning: Landmark MXF_L (No. 13) is missing from 1 specimens."
[1] "Warning: Landmark MXF_R (No. 14) is missing from 1 specimens."
[1] "Warning: Landmark NAS (No. 15) is missing from 2 specimens."
[1] "Warning: Landmark FMO_L (No. 16) is missing from 1 specimens."
[1] "Warning: Landmark FMT_L (No. 17) is missing from 0 specimens."
[1] "Warning: Landmark FRT_L (No. 18) is missing from 0 specimens."
[1] "Warning: Landmark SPH_L (No. 19) is missing from 0 specimens."
[1] "Warning: Landmark FIS_L (No. 20) is missing from 0 specimens."
[1] "Warning: Landmark POR_L (No. 21) is missing from 0 specimens."
[1] "Warning: Landmark AST_L (No. 22) is missing from 0 specimens."
[1] "Warning: Landmark STE_R (No. 23) is missing from 1 specimens."
[1] "Warning: Landmark SPH_R (No. 24) is missing from 2 specimens."
[1] "Warning: Landmark FIS_R (No. 25) is missing from 3 specimens."
[1] "Warning: Landmark POR_R (No. 26) is missing from 2 specimens."
[1] "Warning: Landmark AST_R (No. 27) is missing from 1 specimens."
[1] "Warning: Landmark LAM (No. 28) is missing from 1 specimens."
```

```
[1] "Warning: Landmark INI (No. 29) is missing from 2 specimens."
[1] "Warning: Landmark PGL_L (No. 30) is missing from 0 specimens."
[1] "Warning: Landmark LGL_L (No. 31) is missing from 0 specimens."
[1] "Warning: Landmark AGP_L (No. 32) is missing from 0 specimens."
[1] "Warning: Landmark EGL_L (No. 33) is missing from 1 specimens."
[1] "Warning: Landmark PGL_R (No. 34) is missing from 0 specimens."
[1] "Warning: Landmark LGL_R (No. 35) is missing from 1 specimens."
[1] "Warning: Landmark AGP_R (No. 36) is missing from 1 specimens."
```

This small number of landmarks had to be estimated by means of Geomorph's *estimate.missing()* function before any further analysis. This tool allows to regress the coordinates of missing landmarks through two approaches from which the user can choose by introducing a specific value in the method argument. One is based on the thin plate spline (TPS) method, while the other implements a multivariate regression-based algorithm.

The first of these, the TPS method, has become a commonplace approach in GM (Godinho, O'Higgins, & Gonçalves, 2020). Its implementation in landmark estimation problems is based on Bookstein's TPS principle (1991 in Gunz, Mitteroecker, Neubauer, Weber, & Bookstein, 2009). This principle is best illustrated in Zelditch and colleagues, (2004): An idealized thin steel plate is held in place by several stalks in the position of each landmark point in a shape as described by a coordinate matrix. The length of these stalks is relative to the distance between the same points in this shape and the position of them in another one. If one would move these stalks to the reflect their position in this other shape, the steel plate would become bent, more so in the places where the recorded shapes are more distinct from one another. The TPS provides the algebraic basis to describe this deformation.

This principle is tied to the notion of bending energy. In the previous analogy, bending energy would measure the amount of local deformation as it is a function of the rate of change in the slope of the surface of the bent steel plate (Zelditch et al., 2004). As mentioned by Gunz and colleagues (2009), the TPS based interpolation of missing landmarks is based on its smoothness properties – i.e., the unabrupt transition between shapes that minimizes bending energy. To estimate the coordinates of a missing landmark, a TPS between the incomplete specimen and one where none of the landmarks are missing is computed. Then, an interpolation function is used to map the landmarks present in one shape onto the other.

This technique has been shown to work best with small samples with many landmarks by Gunz and colleagues (2009). It is also better than mean substitution and regression when sample variability is restricted to a single species or genus, as noted by Neeser, Rogers and Gain since 2009. However, it is greatly affected by the choice of an appropriate specimen as a template (Gunz et al., 2009).

More recently, the precision of TPS interpolation in the estimation of missing landmarks has been further tested in the last decade. In 2014, Arbour and Brown conducted a comparative study of four standard estimation techniques. In this publication, they simulated 2D incomplete specimens of various taxa and then compared the deviation between the original and simulated landmark data sets, along with the effect of estimation in the representation of the sample's variability.

Compared to least-squares regression-based estimation, Bayesian regression and mean substitution, TPS performed poorest when the number of incomplete specimens was lowest and highest. Euclidean distance between the estimated and the original landmarks also increased when the TPS was used to interpolate landmarks that were furthest away from the rest, such

as those located on the tip of highly variable bony extrusions. This method was also the least precise when the number of missing landmarks was increased, albeit less so when used to estimate missing landmarks in a *H. sapiens* sample. TPS was also worse when the sample was smallest and largest, especially when applied in a non-human primate sample (which included specimens from three genera - *Gorilla*, *Pan*, and *Pongo*) and in salmonids. From these results, Arbour and Brown ((2014)) warned that TPS was most susceptible to variation and performs best only when taxic diversity is low, landmark count is high, and there is a fair chance that an appropriate template is used. They also concluded that, overall, estimating landmarks with any method produced a more accurate portrayal of sample variability than simply excluding specimens.

Just last year, Godinho, O'Higgins and Gonçalves (2020) tested the reliability of the TPS method in the reconstruction of *H. sapiens* mandibles. Following a similar methodology, they confirmed Arbour and Brown's conclusions regarding the accuracy of this method to estimate landmarks in the far end of a given anatomy or when many landmarks are missing. However, they found that Procrustes distances resulting from estimation error were nearly always much smaller than those between specimens. In their words, *"reconstructed specimens are frequently closer to the original specimen* [...] *than to other individuals"* (Godinho et al., 2020, p. 727, 728).

Compared to most of the samples in Arbour and Brown's (2014) study, the RM sample used for the Ndutu cranium's reconstruction is rather homogenous. As explained before, it has also been tailored to reduce the amount of morphological unknowns. It's size (n = 26) is also slightly smaller than the smallest of their samples (*H. sapiens*, n = 28), yet also moderately larger than all of Godinho, O'Higgins and Gonçalves' (2020) mandible samples (n = 22). It is, however, conspicuously smaller than Neeser and colleagues' (2009) threshold sample size (n = 50 to 100), at which regression finally outperforms the TPS.

It also is noteworthy that the highest number of landmarks employed in Arbour and Brown's (2014) study was 25, far less than the amount used in this study. Additionally, the amount of missing landmarks in the most incomplete specimen in the RM sample (Lesedi 1) is also less (27%) than the proportion of missing landmarks after which mean substitution outperforms both regression and TPS interpolation (30%).

Taking this into consideration, I selected the widely employed TPS interpolation as the estimation method to be implemented through the *estimate.missing()* function.

2.3.4 Measurement Validation

The reliability of a landmark-based reconstruction procedure can be greatly affected by the precision in the registration of the coordinate data of these points. Random error can exacerbate variance, effectively obscuring the biological signal (Fruciano, 2016) that is the basis upon which the process approximates morphological unknowns. To assess the importance of this factor in the collection of landmarks, I used the repeated measurement data to assess random measurement error. For this purpose, I followed three strategies, namely a Procrustes Analysis of Variance (Procrustes ANOVA), the computation of an intra-class correlation coefficient (ICC) and the quantification of a mean measurement error.

The first of these, the Procrustes ANOVA, is a well-known method that was presented by Goodall (1991) as a means to test hypotheses regarding shape variation. Although it is usually resorted to when assessing the effect of asymmetry, its design can be exploited with other purposes (Adams et al., 2021). Like other analysis of variance tests, it is used to assess the

effect of one or more independent variables in the variation of a set of groups – in this case, the sole variable whose effect is tested is that of time, or the measurement iteration, and the groups are the repeated measurements. This analysis tests the null hypothesis that all means are equal by dividing the mean squares (MS) among groups by that within them. Such calculation is indeed an F statistic, alas the MS among and within groups result from the division of the sums of squares (SS) by the degrees of freedom (d.o.f) among and within groups respectively (Madrigal, 2012). Unlike a regular ANOVA, a Procrustes ANOVA will use "sum-of-squared" Procrustes distances among and within groups of specimens as the SS (Goodall, 1991; Adams et al., 2021).

For the sake of familiarity, this analysis was executed in the popular software MorphoJ, version 1.07a (Klingenberg, 2011). First, three *.TPS files were exported from the R environment via the *sink()* function. This allowed to append each one of the three Ndutu cranium fragments' repeated measurement landmark matrices at the end of these files. For each fragment, the code copied only the landmarks present in the corresponding fragment from each of the five repeated measurement matrices of each specimen. Then it pasted the five repeated measurement matrices of that fragment with these same landmarks.

To perform a Procrustes ANOVA, MorphoJ requires a classifier variables text file containing a table with the IDs (names) of each specimen and a specimen number. Such numbers are assumed to be listed under a column called "ind". This allows MorphoJ to identify the repeated measurements corresponding to the same individual. Using the *append()* and *cbind()* base functions in R, I constructed a simple two-column table as required and exported it via the *write.table()* function as a *.TXT file.

Once in the MorphoJ software, I created three new 3D, TPS-based datasets by going to *File* > *Create New Dataset* ..., setting the conditions, locating the corresponding *.TPS file, and then clicking *Create Dataset* in the *Select the appropriate options and the data file* dialog. For each of the three *.TPS files, I imported the classifier text file via the *File* > *Import Classifier Variables* ... function. I then performed a standard full Procrustes superimposition by clicking *Preliminaries* > *New Procrustes Fit* ... and selecting *Align by principal axes* in the emerging dialog box. Finally, I went to *Variation* > *Procrustes ANOVA* ... to compute the analysis. On the opened dialog box, I verified that "ind" had automatically been selected in the *Individual* list and clicked *Execute*.

In MorphoJ's results tab, the function outputted two tables. The tables reported among and within MS, an F statistic and a p-value for a number of dependent variables. In this case, this was reported only for centroid size and shape, given that only symmetrical series of data were considered. While the shape table is usually pondered when assessing the effect of asymmetry, the centroid size table allowed to interpret whether the null hypothesis could be supported or discarded.

The second of these tests, the ICC, is another common resource for the quantification of measurement error that is frequently used to ponder the repeatability of landmark collection (which is why it is represented by R). Despite being a univariate measurement applied to the multidimensional data of GM, higher ICC values indicate "good" repeatability in the measurement of the specimens' morphology. This coefficient is a direct comparison of the variation in the repeated measurements against the that among specimens (Fruciano, 2016) that is given by:

$$R = (S_A^2)/(S_W^2 + S_A^2) \tag{2.1}$$

Where S_A^2 is the variation among individuals and S_W^2 is that within them. S_A^2 and S_W^2 are themselves given by:

$$S_A^2 = (MS_A - MS_W)/n \tag{2.2}$$

$$S_W^2 = MS_W \tag{2.3}$$

MS_A being the among groups ANOVA mean squares and MS_W the withing groups *MS*, while n is the number of measurement iterations.

A common alternative to the ICC that takes into consideration the number of repeated measurements performed is presented in Fleiss (1977 *in* Fruciano, 2016), and Amqvist and Mårtensson (1998 *in* Fruciano, 2016). An average *repeatability* (R_n) value resulting from the mean of the repeated measurements is obtained using the ICC in the following formula:

$$R_n = n \times R/(1 + (n - 1) \times R) \tag{2.4}$$

To compute these values, I introduced these formulas in the R system. Then, I created an interactive dialog using the *readline()* base function prompting for the required MS's.

Finally, I obtained the mean measurement error per iteration following the methodology in Daboul and colleagues (2018). Using the raw coordinates mapped in each 3D model, I computed the mean of the Euclidean distance between each pair of corresponding landmarks in a mean specimen shape and in each repeated measurement. To find this mean shape I constructed an array containing all the repeated measurements of the same specimen and then used the *mshape()* function of the Geomorph package. Then, for every landmark in each measurement I calculated said distance and appended it to a list. I used the values in this list to compute a mean that was saved in another one. Finally, I computed a mean of means per nth measurement.

2.3.5 The *dta()* Tool

As advanced in Section 1.6 of Chapter 1, A. Profico and colleagues' *dta()* tool constitutes the most suitable method to approximate the location of the disarticulated facial fragments of the Ndutu cranium in 3D space. However, as mentioned before, the simple execution of the tool in the R system only allows the alignment of two disarticulated 3D models.

With the appropriate preparation the *dta()* tool's functionality can be extended to align any number of disarticulated fragments by iterating its deployment in a loop. A single loop is enough to alternate between pairs of fragments. It is, however, uncapable of accumulating the results to align one pair and then add a third fragment to it. This requires the nesting of said loop within another one.

As shown in the script in Appendix B, to align the three disarticulated fragments of the Ndutu cranium, several lines were composed which allowed the *dta()* function to run for every element in the DM array and present alternative alignments using different portions of the original data set. Via a combination of the *which()* and complete.cases() base functions, where the data of the corresponding fragments (or aligned pair of fragments) that filled in on every iteration. The loop made it possible to alter between these elements.

To reduce the number of presented alternatives, I made it so that a prompt allowed to first choose a particular disarticulated fragment (for this reconstruction, the reassembled neurocranium) as a starting point. Thereafter, two alternatives were presented, from which a few lines of code also allowed to choose from. Once the preferred alignment was chosen, the aligned landmark set (AM_set) was stored and used as the DM_set_1 for the subsequent iteration. The

contents of the mod_1 vector also changed accordingly. These lines permitted to change the data introduced through them in each iteration until all fragments had been aligned hierarchically.

2.3.6 Performance Assessment and Improval

The *dta()* tool is a versatile resource sensible to the nature of the data that it processes. To measure the precision of the digital alignment of hominin cranial fragments and to compare its performance using different data and constrains I tested the *dta()* function on the entire RM_sample with a smaller R script named "Bottlenose.R" (see Appendix C).

For the first of these purposes, I substituted the landmark coordinates in the DM array with those of each one of the matrices in the sample and deleted that given specimen's matrix from the RM_sample array within a loop. This distributed the landmarks of each specimen among the matrices of each fragment, as if each specimen had been broken apart in the same way as the Ndutu cranium. Using the largest fragment landmark set (the cranial vault and base) I then executed the *dta()* to produce a "re-aligned" version of the each specimen in the sample. In the last lines of the loop, the original RM_sample array was restored from a back-up so that a new specimen could be picked out from the sample in the following iteration.

The precision in the *dta()* tool's performance was measured using the Euclidean distance between corresponding landmarks as described in Subsection 2.3.4. While for the purposes of the validation process detailed in that Subsection, this distance corresponded to the absolute measurement error, in this case it is used to measure the displacement of landmarks with respect to their known position due to the effect of the digital alignment procedure - what I henceforth will dub the *reconstruction error*.

The lines in this last section also saved the alignment along with the original matrix to a small array with the intent of computing this value. However, to prevent these data from being distorted by the translation or rotation caused by the Procrustes superimposition performed during the execution of the *dta()*, I executed a General Procrustes Analysis on this tiny array via the *gpagen()* command. This allowed to reduce the effect of said transformations and thus better distinguish the landmark displacement caused by the procedure. Following similar steps as in 2.3.4, I computed a mean for the re-alignment of the landmarks in the first fragment and then in the second one for each specimen and plotted them. These plots were exported using RStudio's tools to be inserted in this document.

Subsequently, I investigated whether the distance between the original and re-aligned versions of the specimens in the RM_sample could be reduced by altering the data that was used to perform the digital alignment. The nature of these alterations was two-fold: On one side, I changed the amount of landmarks in the data processed by the tool by adding surface semi-landmarks to sample the specimens' relevant-trait-bearing cranial vault and base surfaces; on the other, I adjusted the way the tool used this data by forcing it to use a sample consensus as the template and by adding the necessary information so that the tool would automatically apply symmetry constraints.

Addressing this question required a $2 \times 2 \times 2$ factorial experimental design given that it ponders presence of simple and combined effects of three independent variables (factors) with two levels (applied, not applied) (Feys, 2016). Thus, for each of the fragments, I performed seven additional tests:

- Using the sample consensus shape instead of a template specimen from the RM_sample.

- Implementing symmetrization constraints as exemplified in the *dta()* documentation (Profico et al., 2018).
- Applying surface semi-landmarks on all of the sample 3D models while using a specimen in the sample as a template.
- Using a surface semi-landmark-based consensus instead of a template specimen (combination of the first and third items in this list).
- Applying surface semi-landmarks on the sample and then enforcing symmetrization on a template specimen-based alignment (combination of the second and third).
- Using the optional symmetrization procedure on a consensus-based alignment (combination of the first and second).
- Applying surface semi-landmarks, enforcing symmetrization and using a consensus shape as a template for the alignment (combination of all the first three items in this list).

The lines containing the code for these sub-processes were added to the "Blue.R" script to make it possible to decide whether to implement them or not based on the results of these tests during the Ndutu cranium reconstruction process. Interactive lines made it possible to activate or deactivate them via prompts from the *readline()* function.

Test No. 2: Using the Sample Consensus

As explained in 1.5, Profico and colleagues (2019) have suggested that the *dta()* function offered more accurate results if allowed to select a template specimen from the RM_sample. However, as detailed in 1.3, the affinities of the Ndutu cranium are a matter of controversy. Therefore, allowing the tool to select a specimen upon which to base the alignment may entail an implicit assumption that contradicts our current knowledge of the affinities of the specimen that this work has been dedicated to: that a good template for the Ndutu cranium necessarily exists among the specimens of the sample. Therefore, I investigated how forcing the *dta()* to use a consensus shape would affect landmark displacement.

For this purpose, I added a total of eight short lines to the "Bottlenose.R" script. These commands allowed R to replace all of the landmark coordinates of every single specimen in the RM_sample with the contents of a matrix that represented the sample's consensus landmark configuration, which is one of the outputs of the *gpagen()* function (**$consensus*). By executing the "Bottlenose.R" script for a second time, I re-aligned each specimen based on this consensus and plotted the mean landmark displacement for each fragment for the entire sample.

Test No. 3: Using Symmetrization

A larger section was added to the script to trigger the optional symmetrization process detailed in the Arothron package documentation (Profico et al., 2018) by filling the *pairs_1* and *pairs_2* with the appropriate data. The lines in this section allowed R to construct matrices automatically by exploiting the landmark naming protocol using the landmark names stored in the *varname* object (see Subsection 2.3.2).

Left and right landmarks with names ending in "_L" and "_R", respectively, were detected through the *grep()* base function and their indexes were recorded via *which()*. The list was

refined by excluding unpaired bilateral landmarks, like the right stephanion (STE_R) and the left entoglenoid process (EGL_L) by comparing both lists and selecting only those starting with the same characters using *grep()* again.

Once this process was run iteratively on the entire sample, the test results were printed and the pair of plots that appear in Section 3.2.1 were exported from RStudio.

Test No. 4: Using Surface Semi-landmarks

Ultimately, this test is meant to measure how large the reconstruction error would be if the landmarks in the set also sampled the surface of the parietals and the occipital squama, where three traits amply discussed in the literature, such as parietal bossing, cranial globularity and occipital roundness, are observed (see Section 1.3). Therefore, for this test, I applied 100 evenly-spaced sliding surface semi-landmarks on the cranial vault and base of each specimen in the sample.

An important consideration was the fact that not all of the specimens could be included in the tests where sliding surface semi-landmarks were applied, since they were incomplete or heavily reconstructed. This signified the exclusion of the Gibraltar 1, Herto, La Chapelle aux Saints, Lesedi 1, Sangiran 17 and Steinheim crania, a situation that rendered the tests uneven. In the tests involving this sampling procedure the sample size was reduced to only 20 individuals (this process was not automatized, the corresponding *.PP files were removed from the source directory).

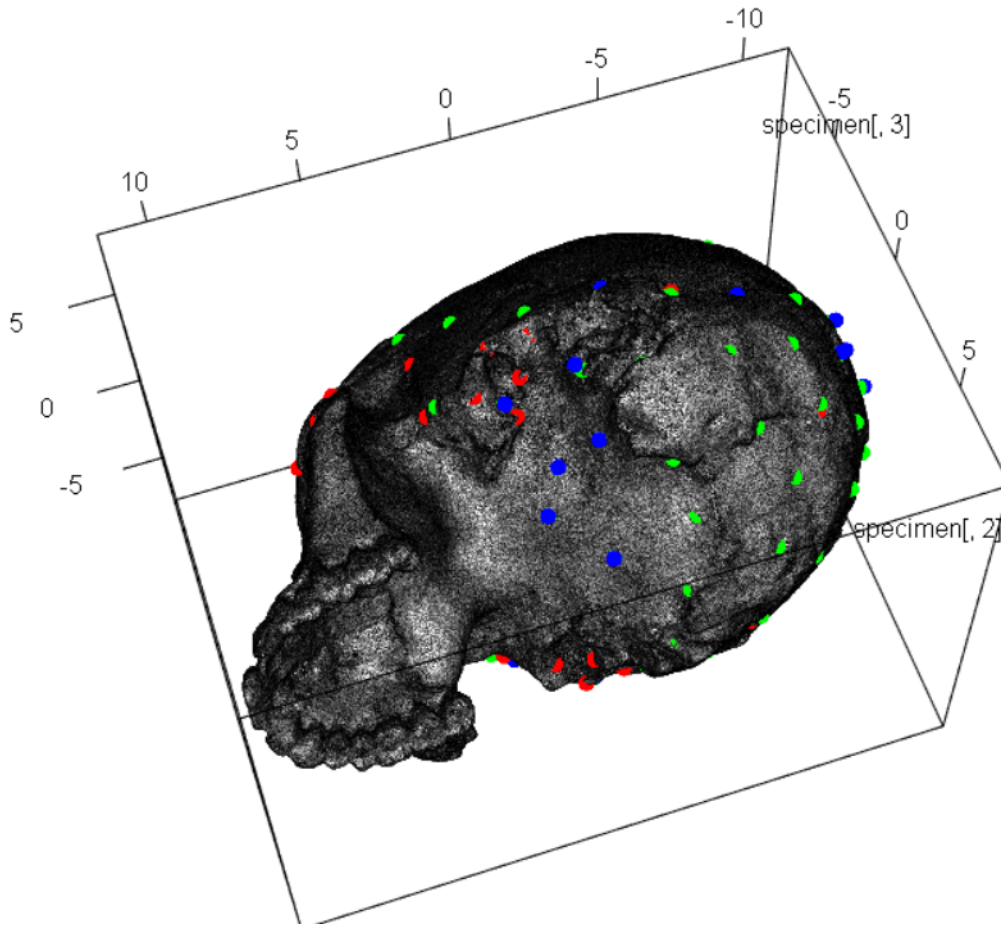

Figure 2.4: RGL device display during sliding-semilandmark application.

To perform this sampling procedure the *geomorph* package requires using surface-only 3D models. These were prepared almost exactly as described in Subsubsection 2.2.1 (Figure 2.5) and brought into the system. However, in this case, only the surface of the cranial vault and base was painted. Afterwards, I prepared a directory that contained the newly produced .PLY files of the entire RM_sample and created a list to import them via a combination of the *list.files()*, *lapply()*, and *file2mesh()* functions. Once loaded, the *buildtemplate()* and *digitsurface()* functions of the Geomorph package made sampling these surfaces with semi-landmarks within a *for()* loop possible without much effort (Figure 2.4).

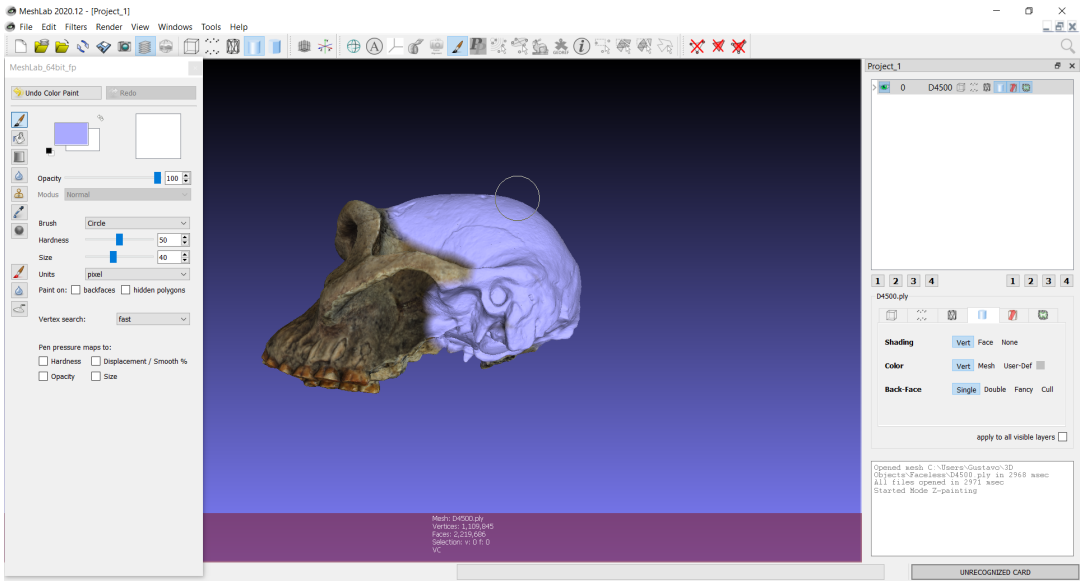

Figure 2.5: Coloring procedure for the selection of colored faces during the production of a surface-only 3D mesh of the D4500 cranium.

I extended the "Bottlenose.R" script to include lines that would make it possible to pick the corresponding specimen's 3D mesh from this list to use it to produce the semi-landmark template and delete it, just to later reconstruct it and pick another one in a subsequent iteration of the loop. A fourth execution of this script outputted two new mean landmark displacement plots (see Section 3.2.1).

Tests No. 5, 6, 7 and 8

Four more tests were achieved by combining the adjustments on each of the first three tests, thus allowing me to measure the reconstruction error produced by combining the effects of using a consensus shape as the template while applying symmetrization constrains, of symmetrization coupled with semi-landmark use, using a semi-landmark based consensus shape, and considering symmetry on the fixed landmarks of a semi-landmark based shape consensus[1]. These combinations were made possible by arranging the lines of code in the "Bottlenose.R" scrip in such way that R would only execute the commands responsible for adjusting the data when an *if()* condition was met and the exact value was entered by the user via a *readline()* prompt.

[1] All procedures employing semi-landmarks used the same $n = 20$ sample as in test No. 3.

2.3.7 Analysis of Test Variable Interactions

I assessed the simple and combined effects of each of the independent variables (the use of a consensus based template, the implementation of the optional symmetrization procedure, and the incorporation of surface semi-landmarks in the data set). Following the procedure outlined by Kassambara (2019), I performed a pair of three-way between-subjects ANOVAs and a collection of preliminary and post-hoc tests.

Three-way ANOVAs are extensions of the ANOVA design (Kassambara, 2019) that allow to evaluate if each independent variable affects the test outcome (in this case, the reconstruction error), as well as whether they interact with each other (for example, in synergy or interference). As with other ANOVAs, the results of the analysis are only reliable when the data meets certain assumptions, namely that the sampling is random, that observations are independent from one another, that the data is normally distributed and that the variances are homogenous across samples (homoscedasticity) - only the last two require preliminary testing (Madrigal, 2012).

For these purposes, the test results were imported manually to the R system by using a combination of the *c()*, *cbind()*, *rbind()*, and *sample_n_by()* functions to produce a data *tibble* (that is, a data frame-like object from the *tidyverse* package). Subsequently, a linear model stating that the reconstruction error is a function of the effects of the three independent variables was introduced by entering *"resterror meanshape*symmetry*semilmks"*, the *aliases* of the dependent and independent variables, as the arguments inside the parenthesis of the base *lm()* function.

Normality both of the ANOVA model residuals and of the sorted data was then tested using the Shapiro-Wilk test via the *shapiro_test()* function (the *tidyverse*-compatible equivalent of the base *shapiro.test()* function (Kassambara, 2019)). When necessary, a quantile-quantile (QQ) plot was produced to visually verify that test data sets had a common distribution (Heckert et al., 2002) by means of the *ggqqplot()* command (*ggplot* package). As recommended by Madrigal (2012), whenever this assumption was not met, logarithmic transformation was applied by means of the base *log()* function on the reconstruction error data of each test instead of attempting a non-parametric analysis.

Homoscedasticity was tested using Levene's test for the equality of variances via the *levene_test()* function. By using single factor models as arguments (for example *resterror meanshape*), equality of variances was tested for the groups exposed to each factor (this included both their single and combined reconstruction error data).

A first ANOVA was computed by executing the *anova_test()* command with a three factor model (*resterror meanshape*symmetry*semilmks*) as the argument. In sight of the significativity of the interactions, a series of follow-up tests were performed. Two-way ANOVAs were conducted to examine two factor interactions at the two different levels (*"y"* for using a consensus shape template, *"n"* for not using it) of the *meanshape* variable and simple simple main effects along the levels of the implementation of surface semi-landmarks. This was achieved by filtering the data using the *filter()* function, as well as adequate two factor and single factor models.

Given the unbalanced nature of this design, the final step consisted on obtaining estimated marginal means to better observe the effect each single or combined variable which may have been obscured by this condition. Unlike the observed means reported in the past subsections, estimated marginal means[2] are adjusted to compensate for varying sample sizes, for which they may differ from them (Lenth, 2016). This was made possible by the implementation of the

[2]Estimated marginal means are also known as "least-squares" means (Lenth, 2021).

emmeans_test() function, to first assess whether there were statistically significant differences between them, and the *get_emmeans()* command to visualize the marginal means (both found in the *emmeans* package (Lenth, 2021)). As recommended by Kassambara, statistical significance was Bonferroni-adjusted.

2.3.8 Production of Alternative Digital Restorations

As expected, no single approach bore the best results for both fragments. Therefore, a similar condition and prompt function combination was used to allow to create each of the final reconstructions in the "Blue.R" script. I chose the most appropriate adjustments to produce statistically informed reconstruction hypotheses for the Ndutu cranium. To explore the consequences of the choices made during the execution of the interactive reconstruction script as well as the demands of the process itself, three additional alternative versions were created.

The reconstruction required the employment of surface semi-landmarks. Given that sampling surfaces with semi-landmarks in R also demands arrays of equal length to properly orient a template, these could not be applied using any of the Ndutu fragments' incomplete matrices that were designed for the first implementation of the tool. Instead, they could only be implemented using a previously reconstructed version of the Ndutu cranium. Therefore, when performing the semi-landmark based reconstruction, I used the landmark data produced after having used the mean shape as a template to generate the (Ndutu_M) reconstruction in the *buildtemplate()* command.

As explained in Clarke, 1990, parietal bossing is only observable in the left parietal because the right one is deformed. To avoid feeding distorted information into the *dta()* by placing semi-landmarks in the right parietal, I created a surface-only 3D mesh in MeshLab following the same procedure as in 2.2.1 to select only the preserved outer layer of the left parietal (Figures 2.6 and **??**). This allowed me to sample the only the better preserved parts of the Ndutu cranial vault and base using 100 sliding surface semi-landmarks.

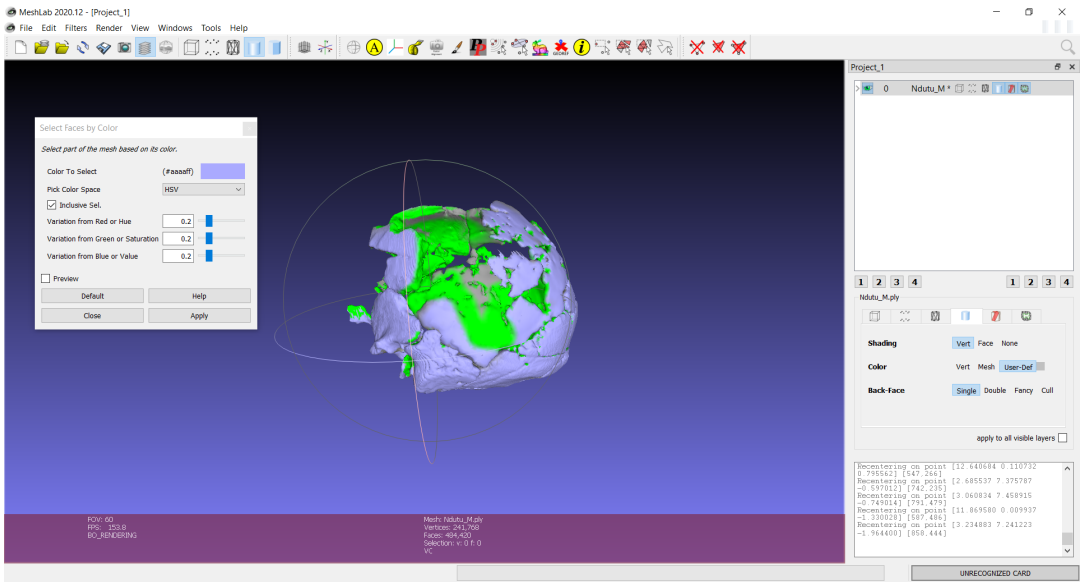

Figure 2.6: By color selection of faces during the production of a surface-only 3D mesh of the Ndutu cranial vault and base fragment cluster.

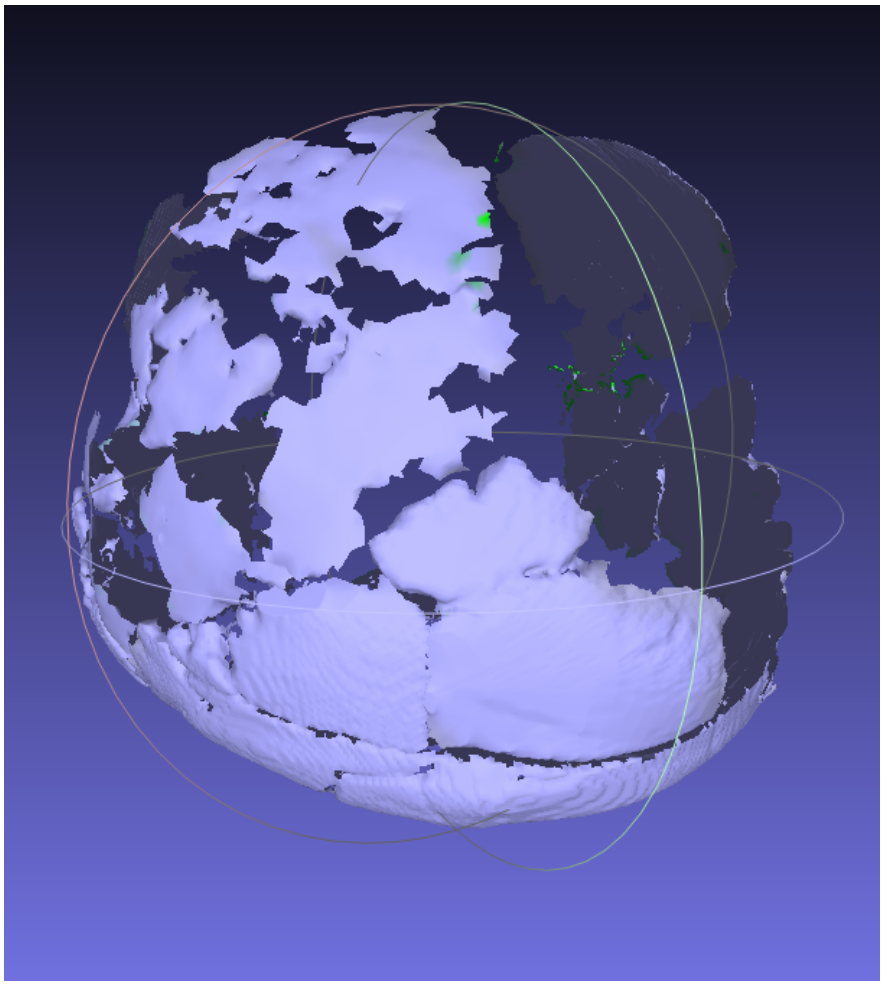

Figure 2.7: Finished surface-only 3D mesh of the Ndutu cranial vault and base fragment cluster.

The application of semi-landmarks also mandated several minor preparation procedures, such as ”re-disarticulating” the previous AM_mesh to produce new fragment meshes in MeshLab after each alignment. This was required since all of the landmarks in AM_set had been translated along with their meshes by the *dta()* in its previous execution. The steps followed to do this were the same as the ones detailed in Subsection 2.1.1.

2.4 Principal Component Analysis

To compare the effects and implications of the reconstruction procedures, I executed a Principal Component Analysis. In GM, a PCA makes it possible to visualize the variation in terms of shape among the specimens in a sample and recognize the axes responsible for the largest proportion of such. To identify them, the analysis aims to eliminate the redundancy in the data, for which a variance-covariance matrix (a symmetrical matrix constructed through the multiplication of the data matrix times its transpose that contains in its diagonal the variances and outside it the covariance between data pairs) is constructed. During the analysis, a new matrix where the data do not depend on each other (an orthonormal base) is also produced. This new matrix is a transformation of the original matrix where covariance is equal to zero (known as orthogonality). The result is a diagonal matrix of eigenvalues - non-zero variances

that are normalized into the principal components (Zelditch et al., 2004).

A dispersion graph comparing two of the components responsible for the largest proportion of the variation in the sample allows to infer causal relationships for the association or dissociation of specimens based on their principal component scores (PC scores). This, since it couples affine groups of data (ibid.) - in this case, it will accumulate specimens with a similar landmark configuration in a given sector of the represented morphospace (a space plain relating and describing the shape of the specimens (Mitteroecker & Huttegger, 2009)).

To perform these analyses, I exported each alternative AM_set array to a *.TPS file, built a file list, and imported them to the MorphoJ software. The MorphoJ allowed to select three specific landmarks: No. 22 (the left *asterion*), No. 27 (the right *asterion*), and No. 28 (*lambda*), in the *Procrustes fit for* [data set] ... emerging dialog to align the specimens for a GPA. This made it possible to eliminate other sources of variation only among the alternative reconstructions, given that these landmarks are in the same position in both specimens. Following the usual procedure, I created a variance-covariance matrix via *Preliminaries* > *Generate Covariance Matrix*. Then I executed the PCA with these data by following *Variation* > *Principal Component Analysis*. I subsequently inspected the eigenvalues histogram in the *Eigenvalues* tab under the the *Graphics* tab to identify the major axes of variation in the sample using the *scree plot* method (Zelditch et al., 2004). Then, I visualized the shape changes along these principal components (PCs) in the *PC shape changes* tab by setting the scale factor to 0.1 and -0.1.

Chapter 3

Results

3.1 Articulated Fragment Reassembly

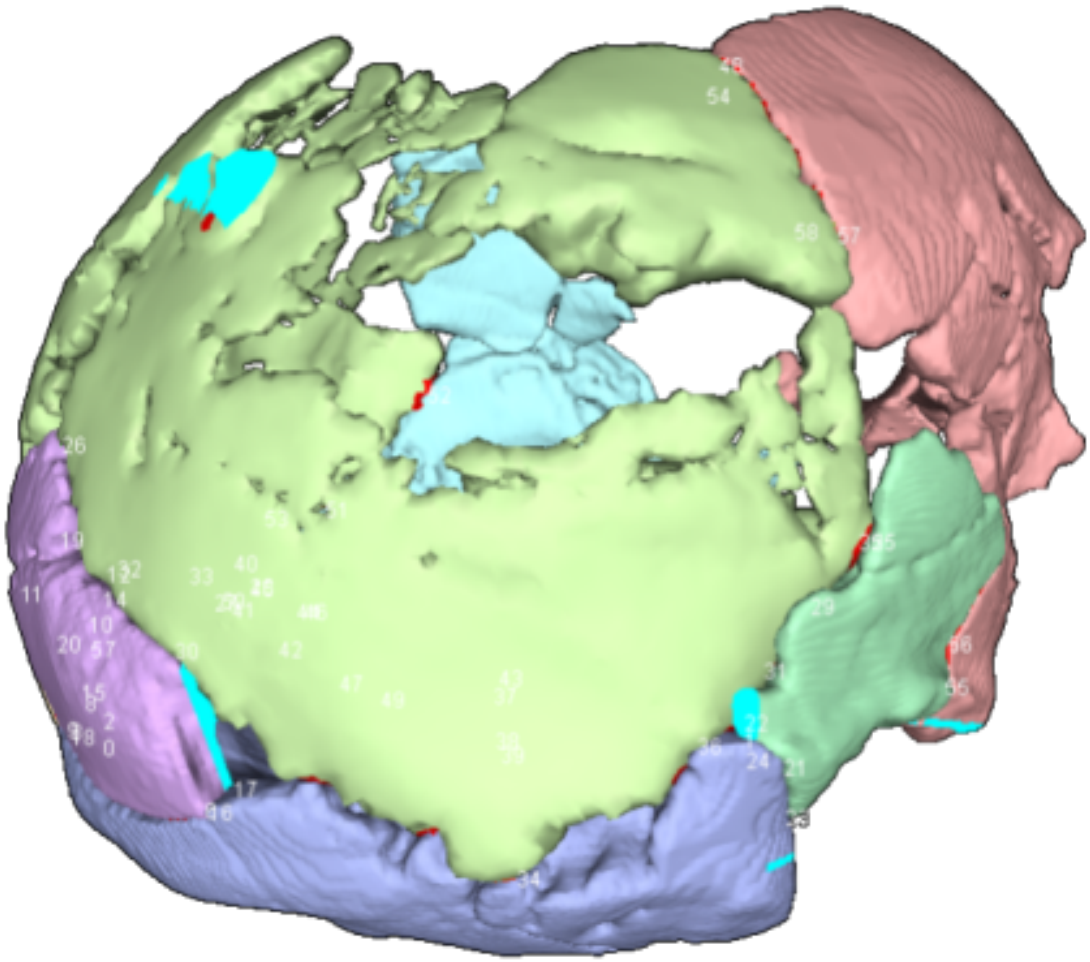

Figure 3.1: Ndutu cranial vault and base fragment cluster reassembled for this work using the Fragment Reassembler version 1.0 (Palmas et al, 2015). *This figure shows 3D mesh overlap (bright red) and deformation introduced by less-than rigid matrix transformation (light blue).*

The Fragment Reassembler software allowed to piece together the articulated fragments of the Ndutu cranium in hierarchical fashion. After the deletion of this hierarchy, the fragments were left joined by constrain bands. Since they are fundamentally contingent to the placement of the point pairs, the constrain bands along with their corresponding residual energy percentage are listed in Appendix A. Here, I report only on the final result of this preliminary step.

The outcome of the reassembly process was the construction of two 3D models. On one side, a large fragment cluster constituting the Ndutu cranium's vault and base, and on the other, a recreation of Clarke's reconstruction in fully assembled form. Both models exhibit minimal 3D mesh overlap (bright red faces), most of which affected the parietals. It is noteworthy that, as illustrated by both Figures 3.1 and 3.2, the Fragment Reassembler software reported that the process introduced a negligible amount of deformation in some regions of the cranium (light blue faces).

Nevertheless, the most conspicuous difference between both reassembled 3D models is that the Fragment Reassembler's algorithm assembled both frontal bone and sphenoid fragments further apart from each other. When considering fracture surface correspondence, global energy reduction makes for a wider frontal bone in the Ndutu cranium (Figure 3.3).

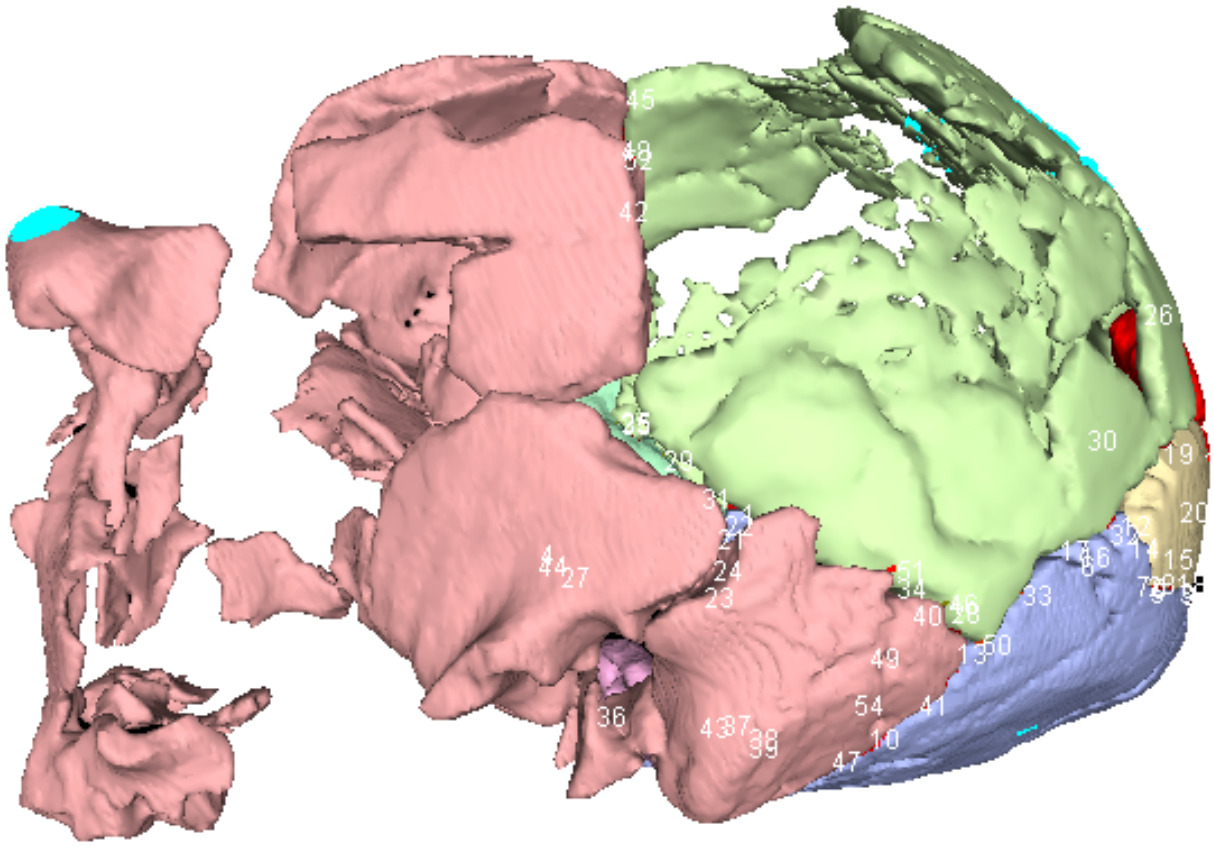

Figure 3.2: Plaster-free 3D model of the Ndutu cranium as reconstructed by Clarke and published in 1990, reassembled for this work using the Fragment Reassembler version 1.0 (Palmas et al, 2015).

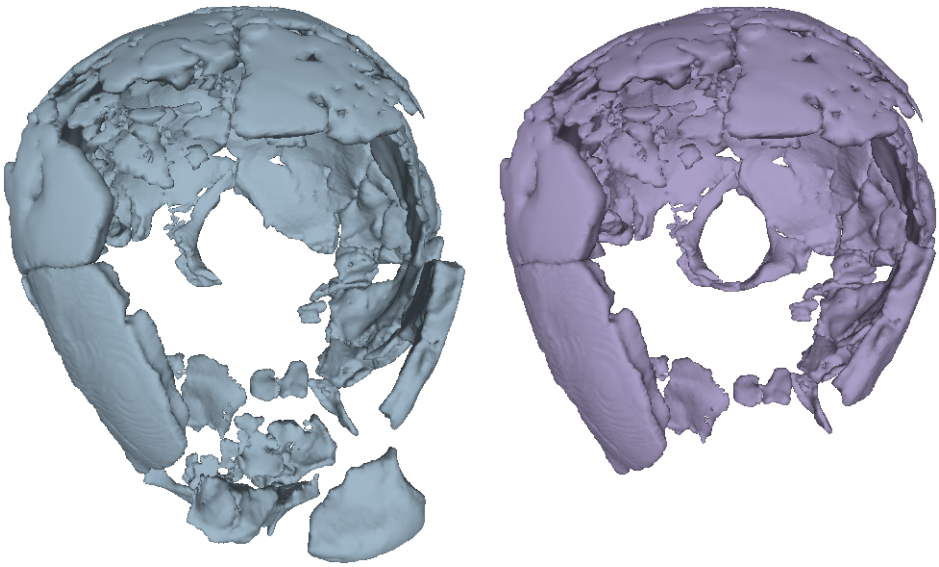

Figure 3.3: Recreation of Clarke's reconstruction (left) and (right) reassembled Ndutu cranium vault and base fragments. Vertical view.

3.2 Digital Alignment

3.2.1 Measurement Validation

Landmarks were registered on the Ndutu cranial vault and base, as well as on the rest of the (feature bearing) fragments and on the reference sample as explained in Section 2.2.2. Measurement bias across both the sample and the Ndutu specimen was assessed in three ways, as detailed in Section 2.3.4. The results that follow account for all of the landmark data (whether belonging to the sample or target specimens) and are grouped considering their correspondence to each of the three major fragment clusters of the Ndutu cranium.

The results of the first of these, the centroid size Procrustes ANOVA were as follows. For the cranial vault and base cluster (Table 3.1) an F statistic of 2462.96 indicating that the variance among specimens is far greater than within them (that is, among repeated measurements) and a p-value inferior to 0.0001 strongly rejected the null hypothesis that the means were equal. Likewise, the analysis of the measurements of the facial skeleton cluster (Table 3.2) with an F of 519.27 and a p-value of less than 0.0001 did not support this either. Finally, the left supraorbital torus fragment (Table 3.3), where few landmarks had been collected, showed a somewhat weaker, albeit certain, rejection of the null hypothesis given an F statistic of 38.70 and a p-value of < 0.0001.

Table 3.1: Neurocranium Centroid Size Procrustes ANOVA

Effect	SS	MS	df	F	P(param.)
Individual	947.440574	35.090392	27	2462.96	<.0001
Residual	1.595692	0.014247	112		height

Table 3.2: Facial Skeleton Centroid Size Procrustes ANOVA

Effect	SS	MS	df	F	P(param.)
Individual	260.181857	9.636365	27	519.27	<.0001
Residual	2.078450	0.018558	112		

Table 3.3: Left Supra-Orbital Centroid Size Procrustes ANOVA

Effect	SS	MS	df	F	P(param.)
Individual	27.691616	1.025615	27	38.70	<.0001
Residual	2.968070	0.026501	112		

ICC's were obtained for each landmark set using the results of the ANOVA tests. It is noteworthy that these results varied depending on the number of landmarks and their definitions. While very high ICC's were reported for the neurocranium and facial skeleton landmarks (0.99044 and 0.99797, respectively), a slightly lower coefficient (0.88291) was obtained from the landmark registration on the left supra-orbital fragment, where landmarks found on bony ridge curves were relatively abundant (see Section 2.2.2). However, consideration of the number of repeated measurements revealed that the repeatability of the registration process was indeed higher overall. Again, the neurocranium and facial skeleton landmark sets returned near-one averaged repeatability values (0.99807 and 0.99959), while a marginally lower value of 0.97416 was obtained for the left supra-orbital landmarks.

Absolute measurement error also indicated that the repeated registration of landmarks varied moderately. Figure 3.4 summarizes and compares the measurement error per repetition and per specimen across all landmark sets. Despite the fact that gathering experience as I collected the landmarks on the specimens seems to have caused this error to be reduced as I progressed through the specimen list (see Figure 3.4 where the specimens are listed in the sequence in which they were measured), it is clear that the distribution of per measurement iteration averages (see Table 3.4) does not clearly support any tendency.

Instead, in some instances high measurement error seems to reflect the inability to observe some suture outlines, as in the cases of Dali and KNM ER 1470 where I found the location of *asterion* was hardest to find. In the former instance, these appear to have been obscured by poor preservation. Still, in average, each repetition deviated less than 0.18 cm from the mean shape.

Table 3.4: Mean measurement error per fragment landmark set and registration iteration

Fragment	Euclidean distance (cm)				
Facial Skeleton	0.1410042	0.1236366	0.1419893	0.1197935	0.1467424
Neurocranium	0.1704310	0.1663307	0.1550111	0.1583391	0.1645547
Supra-orbital	0.1261352	0.1230068	0.1098489	0.1142660	0.1134271

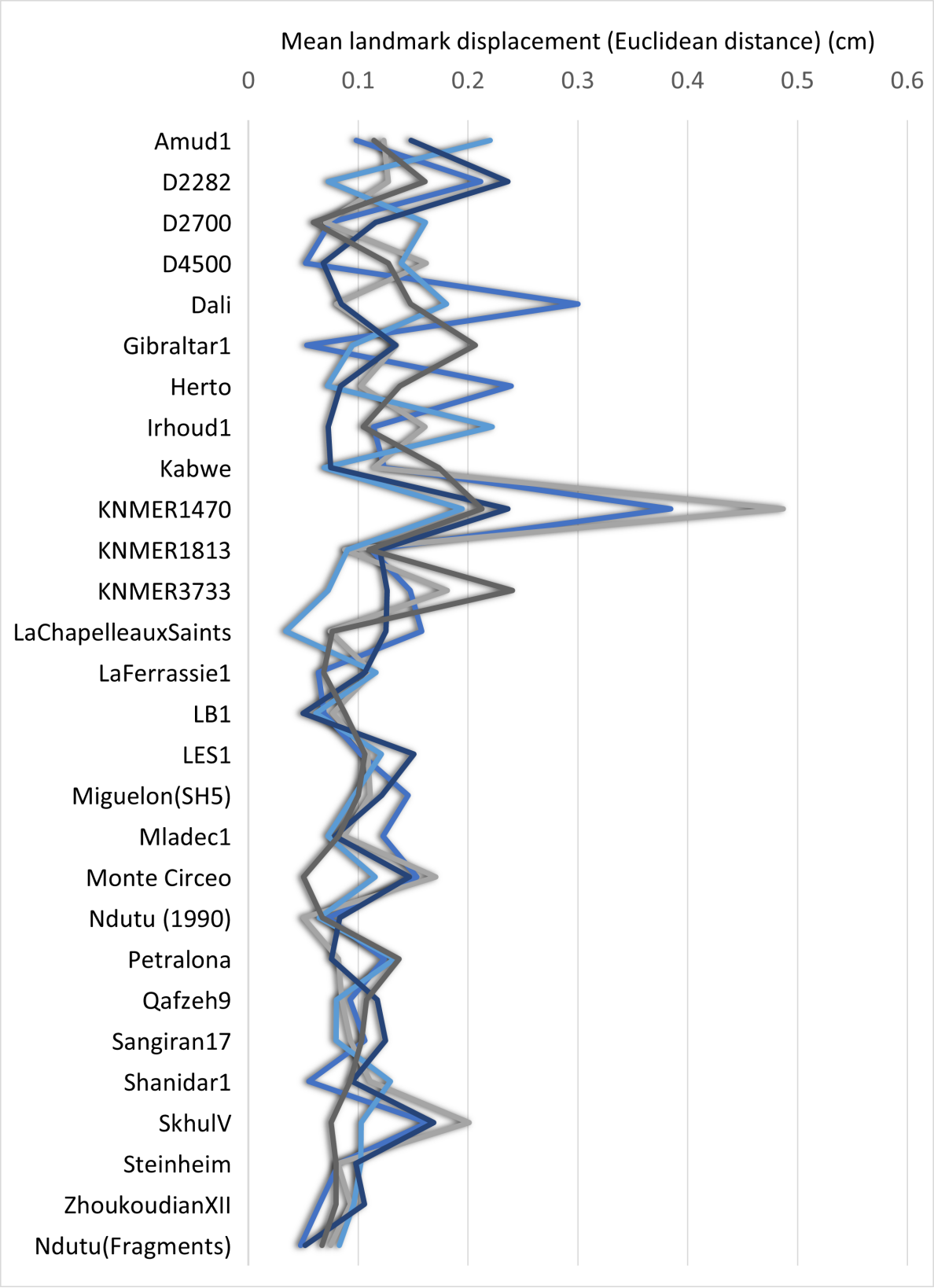

Figure 3.4: **Absolute measurement error.** Mean landmark displacement (Euclidean distance) per repetition and specimen between corresponding landmarks in repeated registrations as indicated by mean landmark displacement (in cm).

3.2.2 Assessment results

Test No. 1

The *dta()* achieved a relatively low degree of precision when used to align the same landmarks found on each fragment of Ndutu cranium on each of the specimens in the sample based on a template picked from the same group. When executed having declared the *pairs_1* and *pairs_2* variables null and using only the landmarks in Section 2.2.2, the ”re-aligned” versions of each cranium deviated nearly 0.8 cm from their original selves, after having been partially superimposed. In average, the ”re-alignment” of the facial skeleton with the Neurocranium generated shapes where the landmarks were 0.50234 cm away from their position in the complete specimens (Figure 3.5). When re-aligning the landmarks on the left supra-orbital (plotted in Figure 3.6), each cranium's shape deviated by a mean of only 0.26934 cm.

With an average landmark displacement of 0.38583 cm, these results appear only slightly less accurate than those reported by Profico and colleagues in 2019 between their reconstruction of the Amud 1 cranium and Susuki and Takai's 1970 reconstruction. However, in the case of Amud 1, only the supra-orbital fragment achieved comparable results (mean landmark displacement equals 0.31778 cm), while the facial skeleton returned a larger error (0.78092 cm) possibly due to differences in the landmarks selected and in the nature and number of fragments aligned. As explained previously, the aligned portions contained the same landmarks as the fragments in the Ndutu cranium would and not the ones that Profico *et al* chose to align. Moreover, the template chosen by the *dta()* tool was Skhul 5 and not La Ferrasie 1 or Shanidar 1, as in their work.

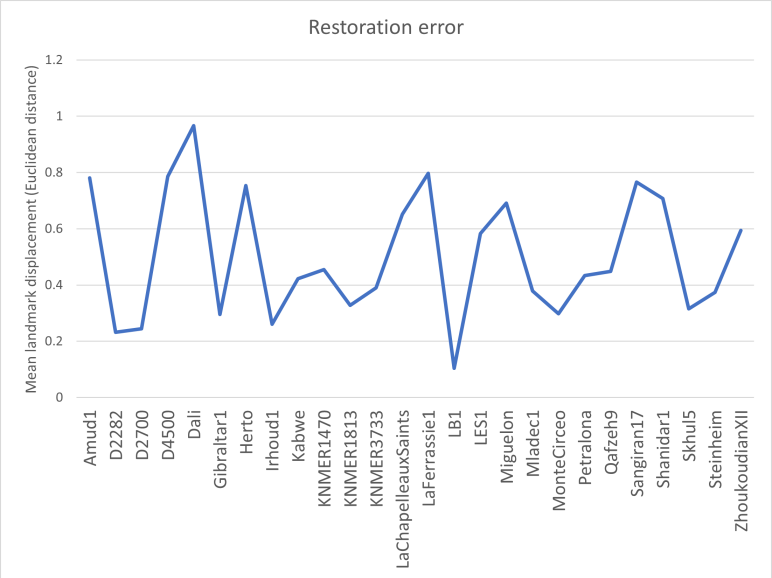

Figure 3.5: Facial skeleton fragment cluster reconstruction error (mean corresponding landmark Euclidean distance) per specimen as indicated by mean landmark displacement (in cm).

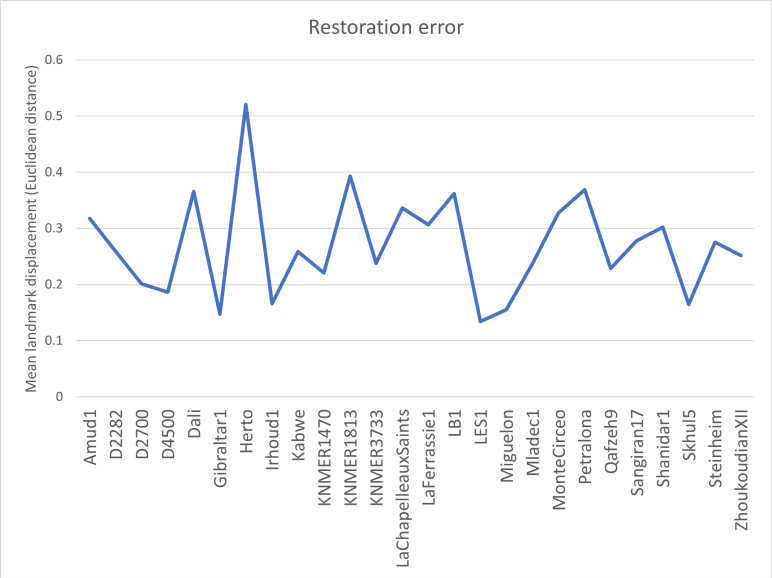

Figure 3.6: Left supra-orbital fragment reconstruction error (mean corresponding landmark Euclidean distance) per specimen as indicated by mean landmark displacement (in cm).

Test No. 2

Executing the *dta()* while forcing it to use the reference sample consensus shape produced better results in general. The distance between corresponding landmarks was shorter in average. The mean reconstruction error for the facial skeleton alignment (Figure 3.7) resulted in 0.37208 cm, while the left supra-orbital (Figure 3.8) was aligned an average of 0.30853 cm away from its position in the crania of the sample, noticeably better than when using a template, at least in general terms.

In the case of the Amud 1 cranium, the tests returned a much smaller reconstruction error in the alignment of the facial skeleton, a mere 0.37549 cm away from Susuki and Takai's reconstruction, which is still only modestly inferior to the results of Profico and colleagues tests, despite the differences in landmark choice. The supra-orbital fragment alignment returned an Euclidean distance of 0.30165 cm for Amud 1, which is comparable to the aforementioned work. However, it was able to produce errors as low as 0.10494 for the Gibraltar 1 individual. Therefore, it appears reasonable to expect that the resulting alignment could be equally as close or even closer to its original position when using the mean shape rather than a template from the RM_sample. This contradicts what is suggested in Profico et al., 2019.

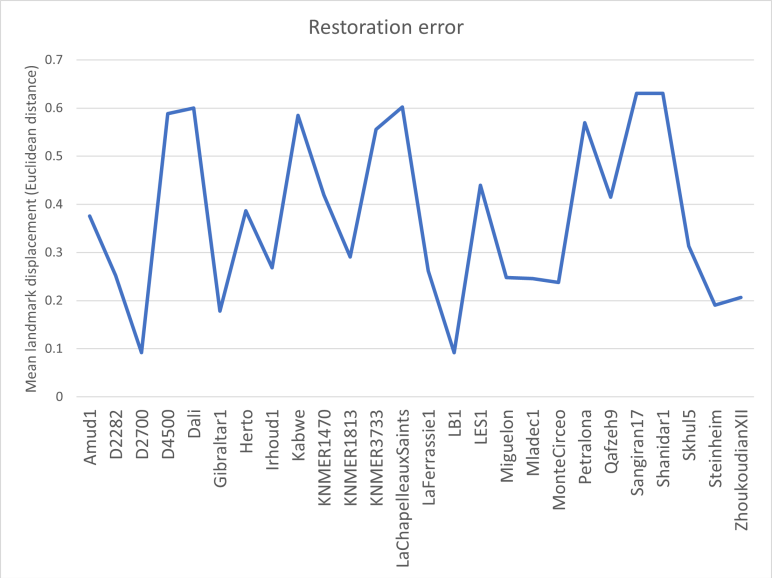

Figure 3.7: Facial skeleton fragment cluster reconstruction error (mean corresponding landmark Euclidean distance) per specimen using the sample consensus shape as a template as indicated by mean landmark displacement (in cm).

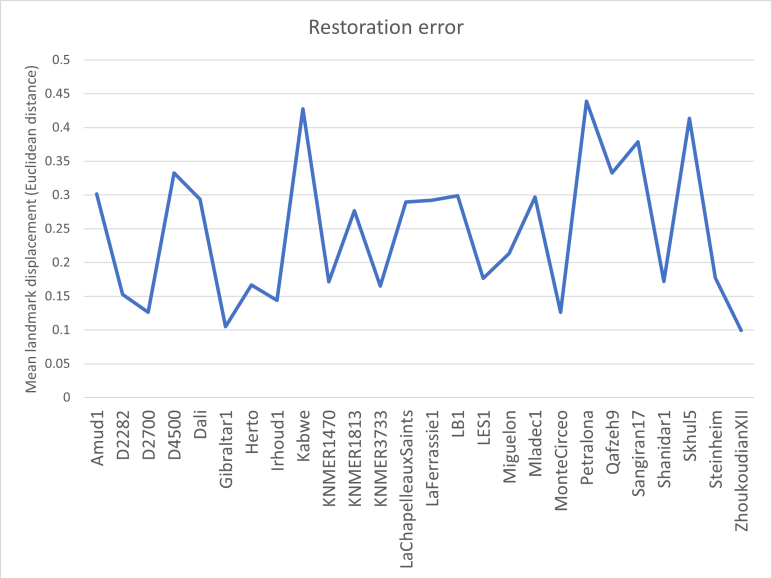

Figure 3.8: Left supra-orbital fragment reconstruction error (mean corresponding landmark Euclidean distance) per specimen using the sample consensus shape as a template as indicated by mean landmark displacement (in cm).

Test No. 3

The implementation of the symmetrization process gravely reduced the tool's precision. In this test, introducing symmetrical landmark correspondence caused an average landmark displacement of 1.70024 cm for the perinasal and maxilla (Figure 3.9) and a more promising mean error of 0.26934 cm for the left supra-orbital (Figure 3.10). When applied to the Ndutu cranium

reconstruction for the sake of further investigating these results, it caused severe forward and downward twisting of the facial skeleton but not of the supra-orbital.

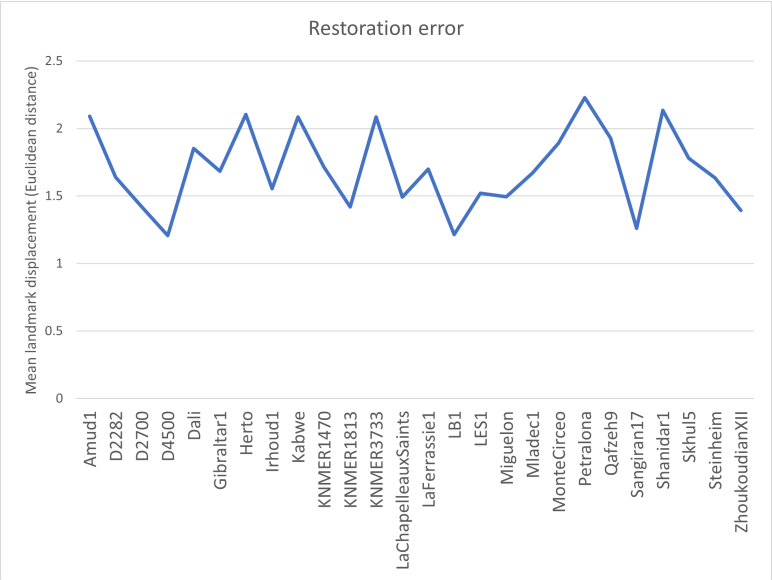

Figure 3.9: Facial skeleton fragment cluster reconstruction error (mean corresponding landmark Euclidean distance) per specimen using symmetrical landmark correspondence information as indicated by mean landmark displacement (in cm).

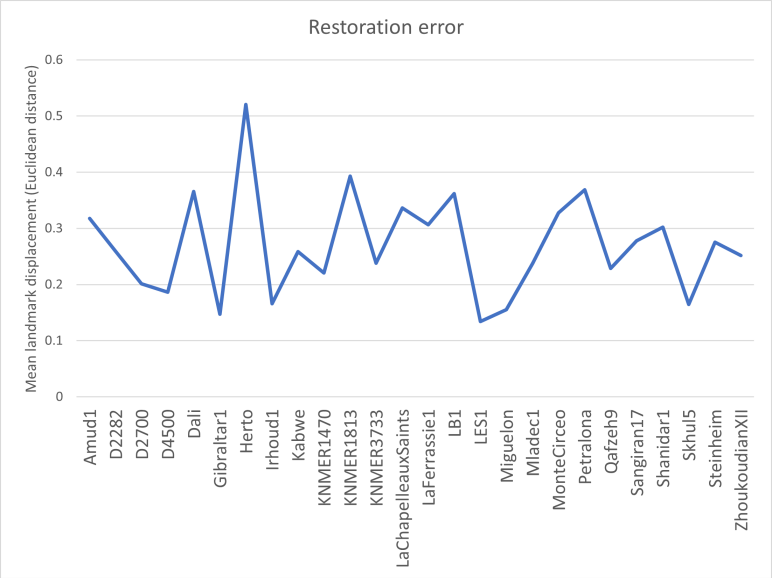

Figure 3.10: Left supra-orbital fragment reconstruction error (mean corresponding landmark Euclidean distance) per specimen using symmetrical landmark correspondence information as indicated by mean landmark displacement (in cm).

Test No. 4

Sampling the cranial vault and base surface's morphology using sliding semi-landmarks produced similarly unfavorable results for the facial skeleton. When using a template from the RM

sample, the landmark displacement in the alignment of the facial fragments was always at least 0.72008 cm, with a mean of 1.08619 cm (Figure 3.11). On the other hand, the average error for the reconstruction of the position of the landmarks in the supra-orbital torus fragment lower than previous tests, with an average distance of of 0.15025 cm (Figure 3.12).

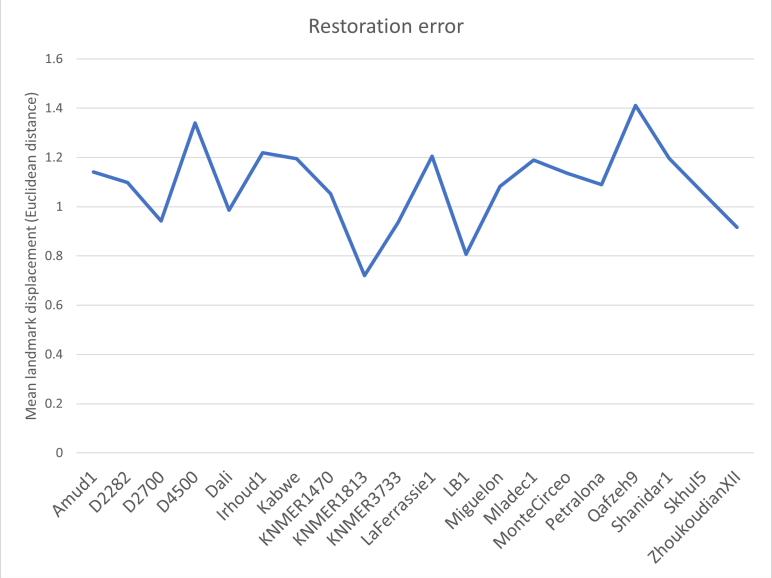

Figure 3.11: Facial skeleton fragment cluster reconstruction error (mean corresponding landmark Euclidean distance) per specimen applying surface semi-landmarks as indicated by mean landmark displacement (in cm).

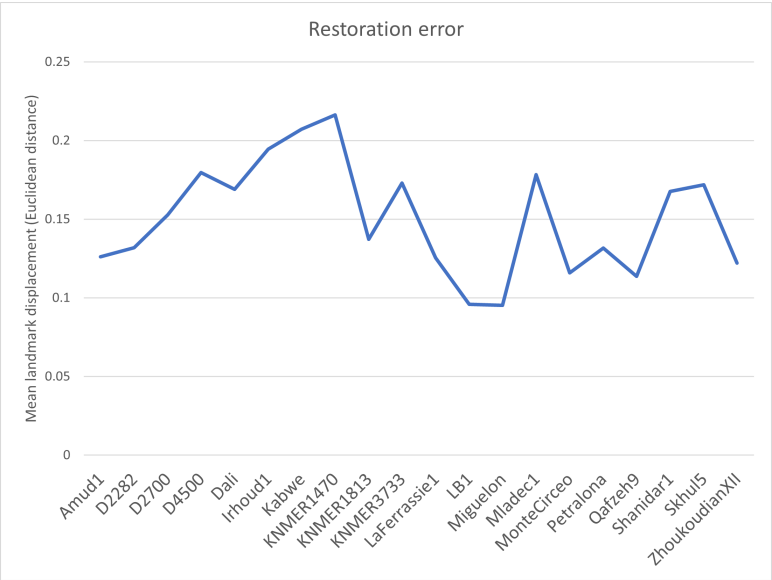

Figure 3.12: Left supra-orbital fragment reconstruction error (mean corresponding landmark Euclidean distance) per specimen applying surface semi-landmarks as indicated by mean landmark displacement (in cm).

Test No. 5

The use of a semi-landmark-based sample consensus shape also produced mixed results. Although when aligning the facial skeleton fragments the average sat at an conspicuously long distance of 1.07578 cm (Figure 3.13). However, the use of this approach to align the supra-orbital fragment reduced the average Euclidean distance even further: 0.12834 cm (Figure 3.14).

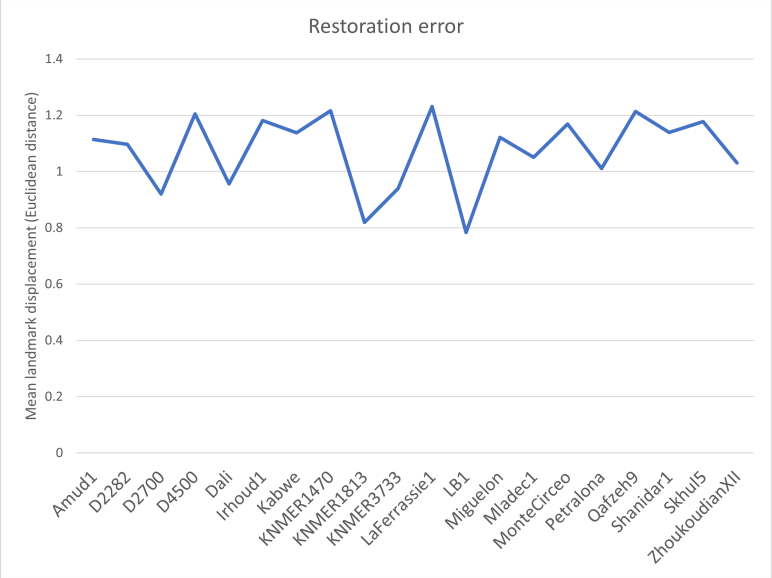

Figure 3.13: Facial skeleton fragment cluster reconstruction error (mean corresponding landmark Euclidean distance) per specimen applying surface semi-landmarks and using a sample consensus shape as a template as indicated by mean landmark displacement (in cm).

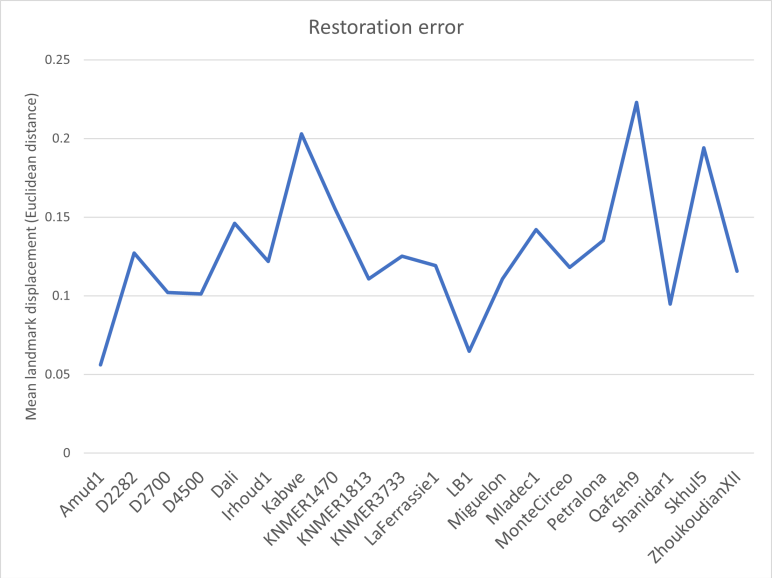

Figure 3.14: Left supra-orbital fragment reconstruction error (mean corresponding landmark Euclidean distance) per specimen applying surface semi-landmarks and using a sample consensus shape as a template as indicated by mean landmark displacement (in cm).

Test No. 6

Using sampling the specimen surfaces through sliding semi-landmarks and then enforcing symmetry constrains on the fixed landmarks of the set brought about better results than test No. 4. Nonetheless, the *dta()* performed poorly. The alignment of the facial skeleton presented a mean error of 1.85070 cm (Figure 3.15), while the supra-orbital fragment was placed 0.14782 cm (Figure 3.16) away from its original location in average.

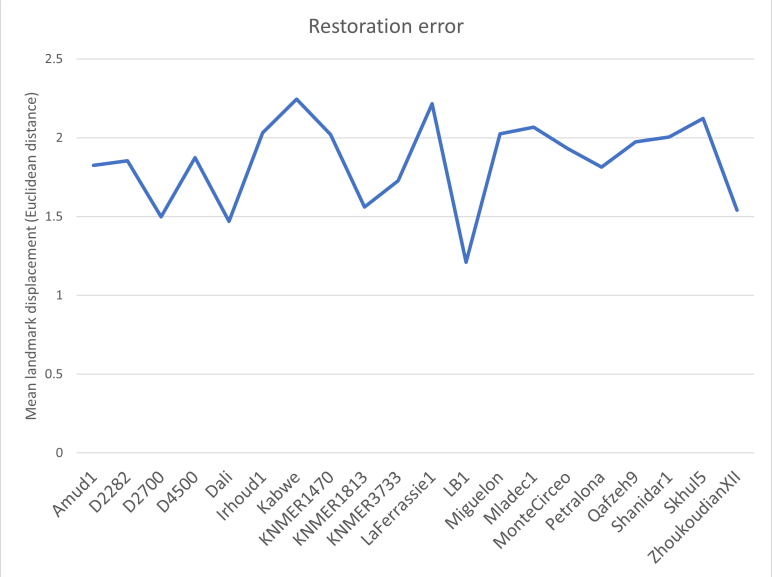

Figure 3.15: Facial skeleton fragment cluster reconstruction error (mean corresponding landmark Euclidean distance) per specimen applying surface semi-landmarks and enforcing symmetry constrains as indicated by mean landmark displacement (in cm).

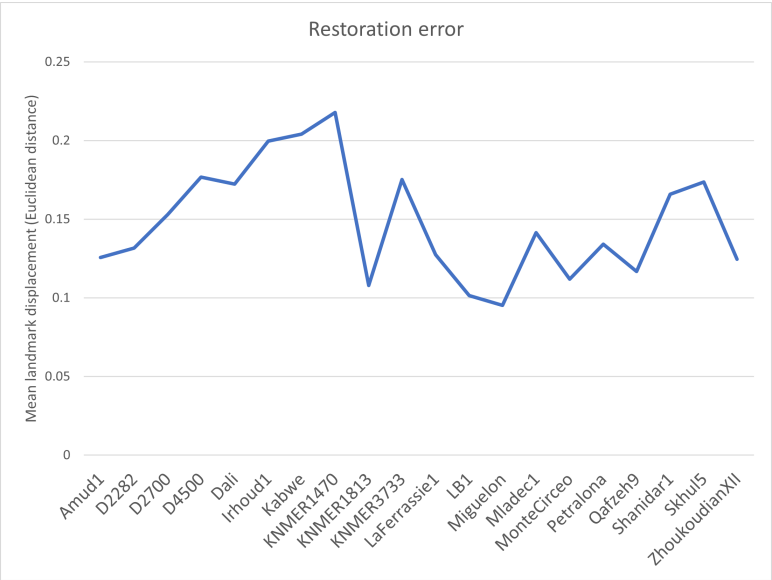

Figure 3.16: Left supra-orbital fragment reconstruction error (mean corresponding landmark Euclidean distance) per specimen applying surface semi-landmarks and enforcing symmetry constrains as indicated by mean landmark displacement (in cm).

Test No. 7

Possibly the largest reconstruction error overall was produced when combining the first and second approaches. When aligning the facial skeleton considering symmetry and employing a consensus-based template, the mean reconstruction error rose to 2.09893 cm, and while estimating the location of the supra-orbital fragment the mean error was 0.24557 cm (Figures 3.17 and 3.18).

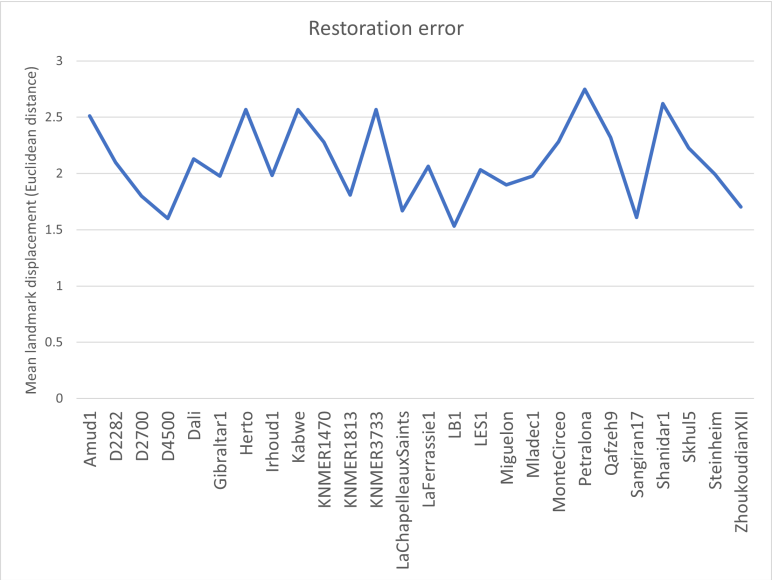

Figure 3.17: Facial skeleton fragment cluster reconstruction error (mean corresponding landmark Euclidean distance) per specimen using a sample consensus shape template while enforcing symmetry constrains as indicated by mean landmark displacement (in cm).

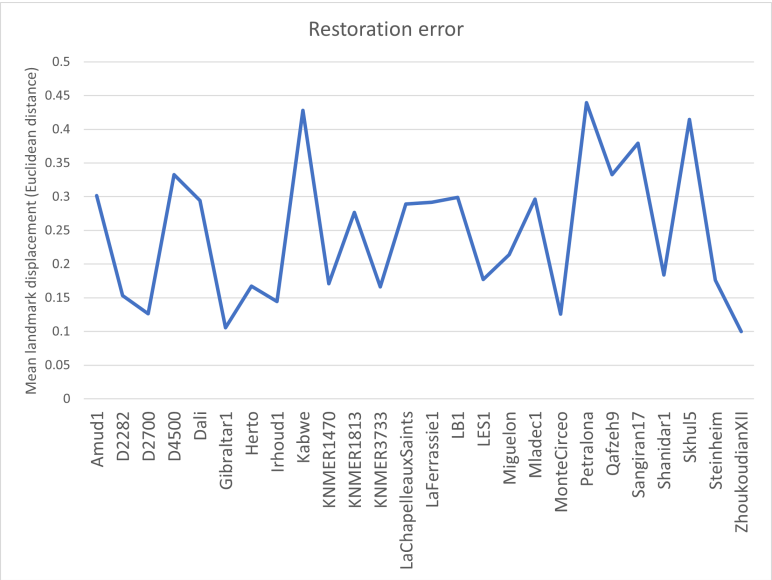

Figure 3.18: Left supra-orbital fragment reconstruction error (mean corresponding landmark Euclidean distance) per specimen using a sample consensus shape template while enforcing symmetry constrains as indicated by mean landmark displacement (in cm).

Test No. 8

Combining all data modifications again generated disparate results. For the facial skeleton fragment cluster, the mean landmark displacement was 1.58420 cm, having been as low as 1.02931 cm in the D2700 cranium and as high as 2.06054 in Skhul 5 (Figure 3.19). However, the *dta()* estimated the location of the supra-orbital landmarks a mere 0.12931 cm away from their real position in average, only slightly further away than in test No. 5 (Figure 3.20).

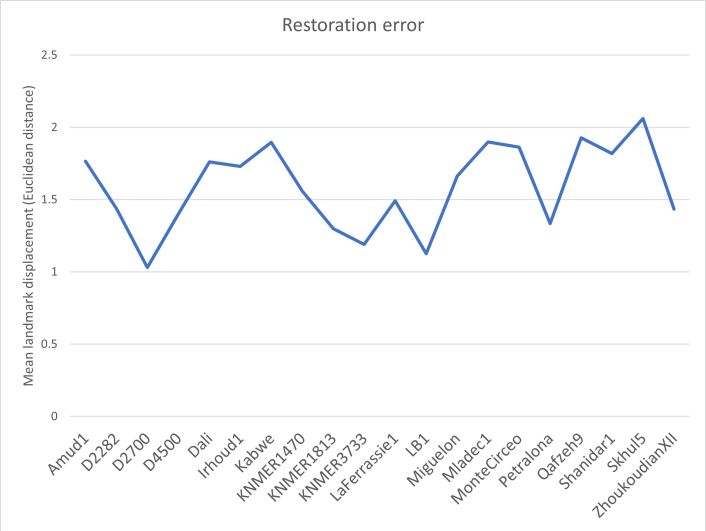

Figure 3.19: Facial skeleton fragment cluster reconstruction error (mean corresponding landmark Euclidean distance) per specimen having applied sliding surface semi-landmarks, using a sample consensus shape template, and enforcing symmetry constrains as indicated by mean landmark displacement (in cm).

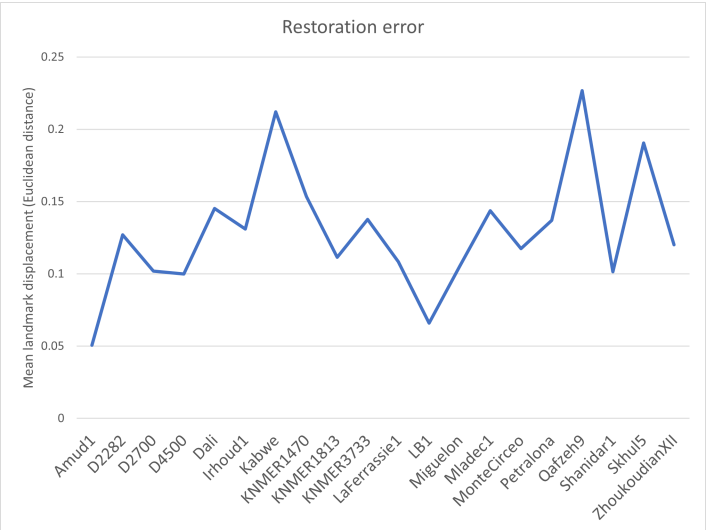

Figure 3.20: Left supra-orbital fragment reconstruction error (mean corresponding landmark Euclidean distance) per specimen having applied sliding surface semi-landmarks, using a sample consensus shape template, and enforcing symmetry constrains as indicated by mean landmark displacement (in cm).

3.2.3 Test Variable Interactions

I conducted a three-way ANOVA to ascertain the effects of the use of a consensus shape based-template, surface sampling with sliding semi-landmarks, and the implementation of the optional symmetrization procedure on the mean displacement of landmarks resulting from the execution of the *dta()* on all of the specimens in the sample. As a preliminary step, I tested the assumptions of said three-way ANOVA. Normality was evaluated using Shapiro-Wilk's test, while homoscedasticity was assessed following Levene's method.

For the reconstruction of the facial skeleton landmarks, the residuals of the model associating the three factors with the reconstruction error were normally distributed ($p > 0.05$) (Table 3.5). Mean landmark displacement also had a normal distribution except in one group ($p = 0.0338$), where using a consensus based-template was the only factor at play (although a the null hypothesis was only marginally discarded when this was combined with the use of semi-landmarks) (Table 3.6). Levene's test revealed that two out of three groups complied with the assumption of homoscedasticity ($p > 0.05$). It is only when the grouping factor is the use of semi-landmarks ($p = 1.22\times10^{-15}$) that the equality of variances cannot be assumed (Table 3.14).

Table 3.5: Shapiro-Wilk's normality test for the model residuals of the function of the reconstruction error of the facial skeleton landmarks

Variable	Statistic	P-value
Residuals (model)	0.996	0.902

Table 3.6: Shapiro-Wilk's normality test for experiment groups of the reconstruction error of the facial skeleton landmarks

Consensus shape -based template	Symmetrization	Use of semi-landmarks	Variable	Statistic	P-value
no	no	no	Restoration error	0.948	0.204
no	no	yes	Restoration error	0.977	0.892
no	yes	no	Restoration error	0.955	0.295
no	yes	yes	Restoration error	0.941	0.254
yes	no	no	Restoration error	0.915	0.0338
yes	no	yes	Restoration error	0.906	0.0543
yes	yes	no	Restoration error	0.957	0.336
yes	yes	yes	Restoration error	0.959	0.518

Table 3.7: Levene's test for the equality of variances for factor groups of the reconstruction error of the facial skeleton landmarks

Factor	df1	df2	Statistic	P-value
Symmetrization	1	182	1.78	0.184
Consensus shape -based template	1	182	3.14	0.0778
Use of semi-landmarks	1	182	77.0	1.22e-15

Table 3.8: Three factor ANOVA (type II tests) of the mean landmark displacement of the reconstruction error of the facial skeleton landmarks

Effect	DFn	DFd	F	P-value	p<.05	ges
Consensus shape	1	176	0.175	6.76e-01		0.000993
Symmetrization	1	176	867.653	6.17e-70	*	0.831000
Semi-landmarks	1	176	37.331	6.23e-09	*	0.175000
Consensus shape:Symmetrization	1	176	6.273	1.30e-02	*	0.034000
Consensus shape:Semi-landmarks	1	176	13.023	4.01e-04	*	0.069000
Symmetrization:Semi-landmarks	1	176	119.487	1.48e-21	*	0.404000
Consensus shape:Symmetrization: Semi-landmarks	1	176	26.988	5.62e-07	*	0.133000

A statistically significant three-way interaction between the use of a consensus shape-based template, the deployment of the symmetrization process and the application of semi-landmarks in the alignment of the facial skeleton landmarks was found ($p = 5.62 \times 10^{-07}$) (Table 3.8). Single factors also had a significant effect on the results, with the use of the optional symmetrization procedure having by far the largest effect size (ges = 0.831). Taking this into consideration, I investigated simple two-way interactions between the use of semi-landmarks and consensus shape -based template at both levels of the *symmetrization* variable. A follow-up two-way ANOVA (Table 3.9) revealed a statistically significant ($p > 0.05$) two-way interaction between the use of semi-landmarks and a consensus when the optional symmetrization process is executed.

Table 3.9: Two factor ANOVA at both levels of the symmetrization variable of the mean landmark displacement of the reconstruction error of the facial skeleton landmarks

Symmetrization	Effect	DFn	DFd	F	P-value	p<.05	ges
no	Consensus shape	1	88	4.24	4.2e-2	*	0.046
no	Semi-landmarks	1	88	283	3.07e-29	*	0.763
no	Consensus shape:Semi-landmarks	1	88	2.45	1.21e-1		0.027
yes	Consensus shape	1	88	2.87	9.4e-2		0.032
yes	Semi-landmarks	1	88	7.82	6e-3	*	0.082
yes	Consensus shape:Semi-landmarks	1	88	26.1	1.89e-6	*	0.228

When aligning the facial skeleton landmarks, the use of semi-landmarks had the strongest effect (significant single single main effect) on the reconstruction error when a consensus shape-based template was used along the execution of the symmetrization procedure (Table 3.10). Estimated marginal means for the subjects where consensus templates and symmetrization were (test No. 7) or were not (test No. 8) used in conjunction with semi-landmarks differed only slightly from the observed means (1.58 cm and 2.10 cm, respectively). This allowed to interpret that, despite having the largest effect size (ges = 0.387), the effect of the use of sliding semi-landmarks is associated with a reduction of the joint amplification of the reconstruction error caused by combining the other two variables. Since the marginal mean is still larger, only using a consensus shape-based template instead of combining it with any other approach seems to offer better results.

Table 3.10: ANOVA at both levels of the consensus shape variable of the mean landmark displacement of the reconstruction error of the facial skeleton landmarks when symmetrization is used

Consensus shape	Symmetrization	Effect	DFn	DFd	F	P-value	p<.05	ges
no	yes	Semi-landmarks	1	44	3.05	8.8e-2		0.065
yes	yes	Semi-landmarks	1	44	27.8	3.96e-6	*	0.387

The residuals of the model for the three-way ANOVA of the data outputted by the simulations of the alignment of the supra-orbital landmarks did not meet the assumption of normality (Table 3.11). Hence, logarithmic transformation of the reconstruction error values obtained for each one of the tests was a necessary prior step. This ensured that the model residuals (Table 3.12) and all of the experiment group data (Figure 3.13) distributed normally. Meanwhile, Levene's test was not significant on two of the three factor-based groups (Table **??**.

Table 3.11: Shapiro-Wilk's normality test for the model residuals of the function of the reconstruction error of the supra-orbital landmarks

Variable	Statistic	P-value
Residuals (model)	0.975	0.00199

Table 3.12: Shapiro-Wilk's normality test for the model residuals of the function of the log-transformed reconstruction error of the supra-orbital landmarks

Variable	Statistic	P-value
Residuals (model)	0.988	0.114

Table 3.13: Shapiro-Wilk's normality test for experiment groups of the log-transformed reconstruction error of the supra-orbital landmarks

Consensus shape -based template	Symmetrization	Use of semi-landmarks	Variable	Statistic	P-value
no	no	no	log(Restoration error)	0.978	0.819
no	no	yes	log(Restoration error)	0.955	0.447
no	yes	no	log(Restoration error)	0.978	0.819
no	yes	yes	log(Restoration error)	0.962	0.595
yes	no	no	log(Restoration error)	0.935	0.102
yes	no	yes	log(Restoration error)	0.945	0.298
yes	yes	no	log(Restoration error)	0.938	0.122
yes	yes	yes	log(Restoration error)	0.941	0.249

Table 3.14: Levene's test for the equality of variances for factor groups of the log transformed reconstruction error of the supra-orbital landmarks

Factor	df1	df2	Statistic	P-value
Symmetrization	1	182	10.0	0.00183
Consensus shape -based template	1	182	0.00955	0.922
Use of semi-landmarks	1	182	10.0	0.00183

A three factor ANOVA conducted on the log transformed mean landmark displacement resulting of the alignment of the supra-orbital landmarks revealed no significant interactions. Nonetheless, both the use of both a consensus shape-based template and sliding surface semi-landmarks exerted main effects ($p > 0.05$) on the reconstruction error (Table 3.15), with the latter having the largest effect size.

Table 3.15: Three factor ANOVA (type II tests) of the log transformed reconstruction error of the supra-orbital landmarks

Effect	DFn	DFd	F	P-value	p<.05	ges
Consensus shape	1	176	7.965	5.00e-03	*	4.30e-02
Symmetrization	1	176	0.001	9.70e-01		7.98e-06
Semi-landmarks	1	176	121.422	8.28e-22	*	4.08e-01
Consensus shape:Symmetrization	1	176	0.010	9.19e-01		5.89e-05
Consensus shape:Semi-landmarks	1	176	0.140	7.08e-01		7.96e-04
Symmetrization:Semi-landmarks	1	176	0.006	9.36e-01		3.63e-05
Consensus shape:Symmetrization: Semi-landmarks	1	176	0.006	9.37e-01		3.54e-05

Pairwise comparisons computed using the estimated marginal means test on the original data revealed that statistically significant differences between both levels of both main effects - i. e., that, when aligning the supra-orbital landmarks, both forcing the *dta()* to use a consensus shape as a template instead of a subject in the sample and sampling neurocranium surfaces using sliding semi-landmarks, separately, produced significantly different reconstruction error values than when allowing the tool to choose a template using a smaller fixed landmark set. Notably, a lower p-value was reported for semi-landmark use ($p = 7.31 \times 10^{-20}$) (Table 3.16). This configuration was also associated with the lowest estimated marginal mean of 0.139 cm (only slightly lower than the observed mean).

Table 3.16: Estimated marginal means test (Lenth, 2021) for the reconstruction error of the supra-orbital landmarks (Bonferroni-adjusted)

Factor	Response variable	Level 1	Level 2	df	Statistic	P-value	p.adj
Consensus shape	Restoration error	no	yes	182	1.57	0.118	0.118
Semi-landmarks	Restoration error	no	yes	182	10.3	7.31e-20	7.31e-20 *

3.2.4 Digital Restoration

Taking in to account the *dta()* performance effect and interaction analysis results exposed in the previous section, one can venture that the scenario where the tool performs best is when the supra-orbital is aligned using only sliding semi-landmarks, while the error is minimized when aligning the facial skeleton fragments using fixed landmarks along with a consensus shape-based template. Heeding this train of thought, I followed a mixed approach to produce a primary reconstruction of the location of the fragments of the Ndutu cranium henceforth dubbed *Ndutu_MIX* (Figure 3.28, b, and Figures 3.21, 3.22, 3.23, 3.24, 3.25, and 3.26).

For the alignment of the supra-orbital fragment, sliding semi-landmarks were added to the same fixed landmark set. The *dta()* was allowed to choose the best template using a 136 landmark set that included these surface sampling points. As a result, the alignment of the supra-orbital fragment was based on the Irhoud 1 cranium. Meanwhile, the facial skeleton's alignment only employed fixed landmarks, but the consensus shape as a template, reducing the reconstruction error to its minimum.

The semi-landmarks applied on the Ndutu cranium permitted the sampling of the preserved outer table of the left parietal, which boasts the parietal bossing discussed in Clarke, 1990 and later publications. It also made it possible to consider the occipital squama's roundness and convexity, but specially the position of a few semi-landmarks located on the surface of the frontal squama, to estimate the alignment of a contiguous element - the antero-lateral end of the frontal bone.

Considering the possibility that using the consensus shape as a template on the supra-orbital fragment also exerted an error reducing effect on the alignment, I created a few additional alternative reconstructions, which were based exclusively on the 36 fixed landmark set. The first of them, which I named *Ndutu_M*, employed a the consensus landmark configuration as the template to align both the supra-orbital and facial elements. In a second case, the *dta()* tool was simply allowed to run as usual, consequentially searching for an appropriate template from the RM sample to align both fragments. This time, the procedure also found that Irhoud 1 posessed the fixed landmark configuration that was closest to that of the Ndutu fragments. Hence, this second alternative, named *Ndutu_T* was also based on the Moroccan individual.

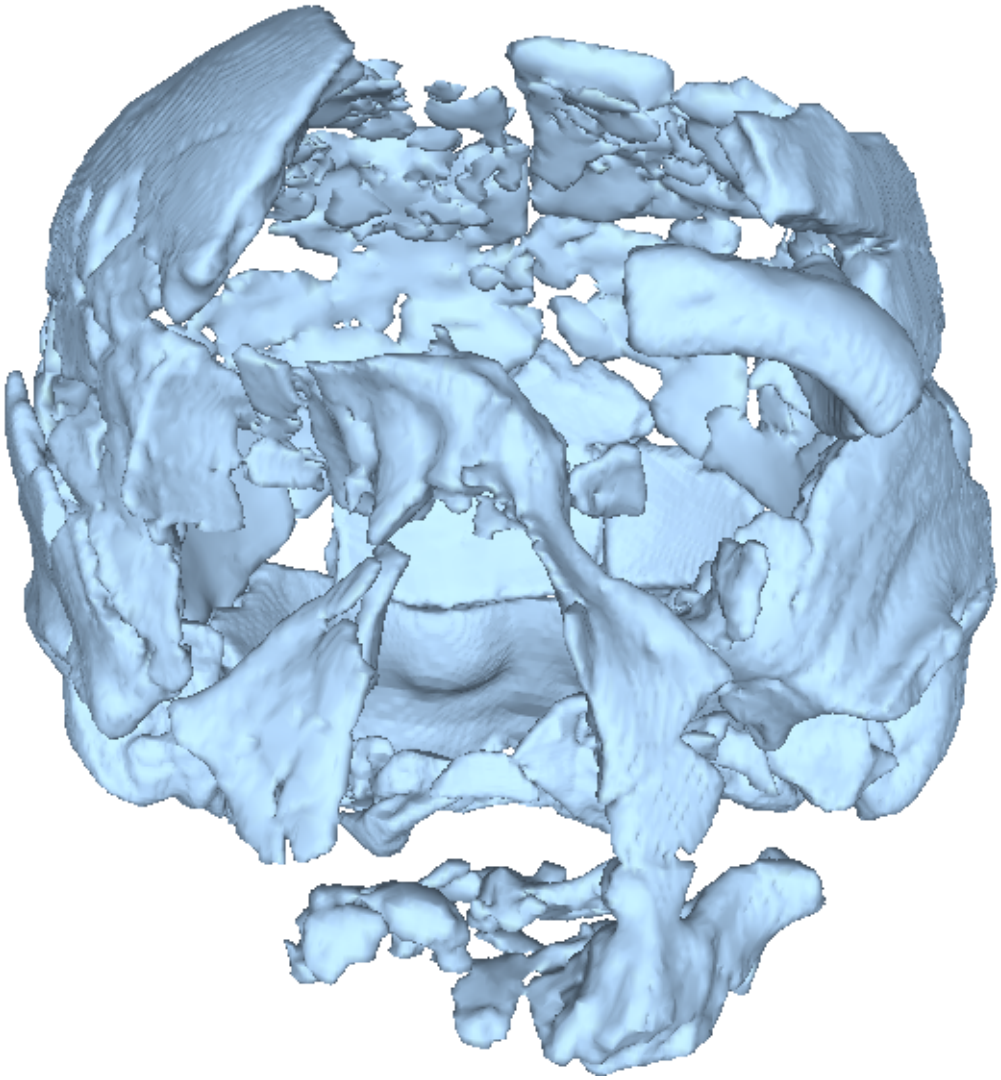

Figure 3.21: Reconstruction of the Ndutu cranium using fixed landmarks and sliding surface semi-landmarks to align the supra-orbital fragment and fixed landmarks to position the facial skeleton fragment cluster, frontal view.

Figure 3.22: Reconstruction of the Ndutu cranium using fixed landmarks and sliding surface semi-landmarks to align the supra-orbital fragment and fixed landmarks to position the facial skeleton fragment cluster, left lateral view.

Figure 3.23: Reconstruction of the Ndutu cranium using fixed landmarks and sliding surface semi-landmarks to align the supra-orbital fragment and fixed landmarks to position the facial skeleton fragment cluster, right lateral view.

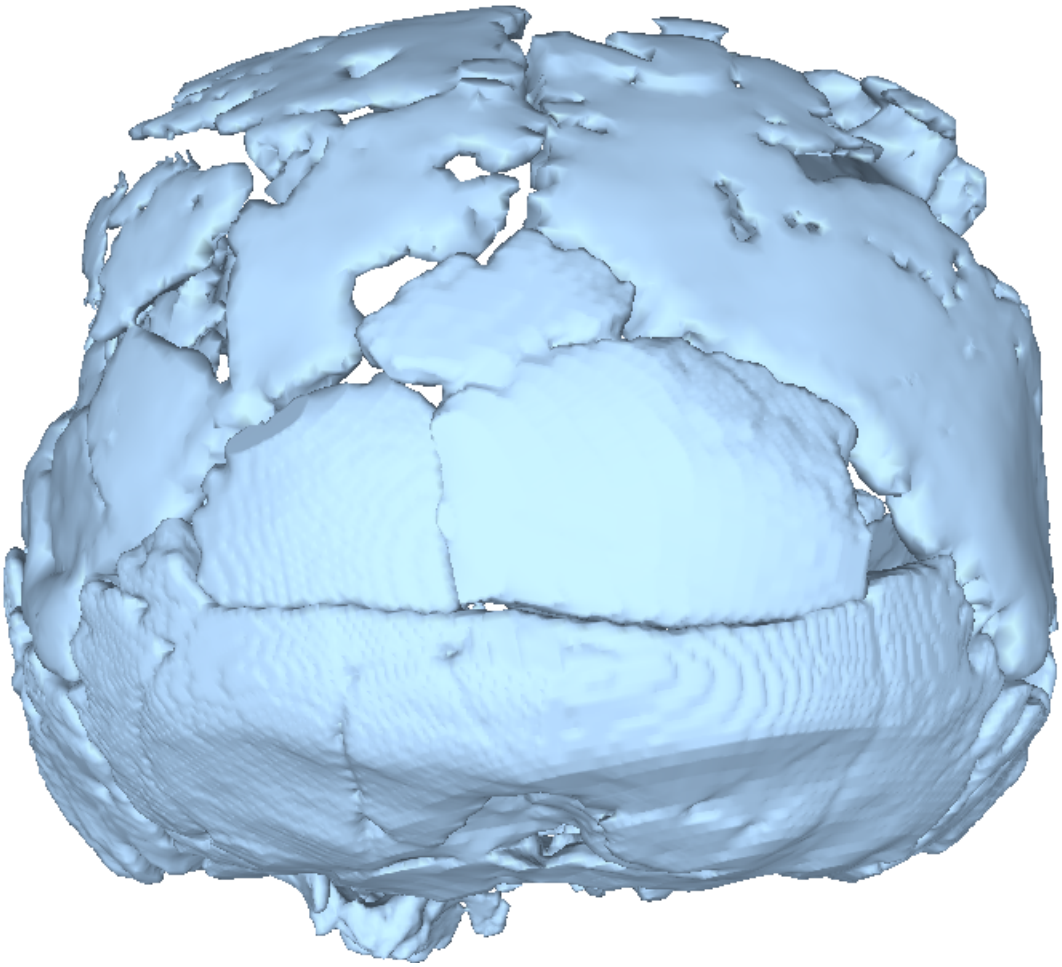

Figure 3.24: Reconstruction of the Ndutu cranium using fixed landmarks and sliding surface semi-landmarks to align the supra-orbital fragment and fixed landmarks to position the facial skeleton fragment cluster, nuchal view.

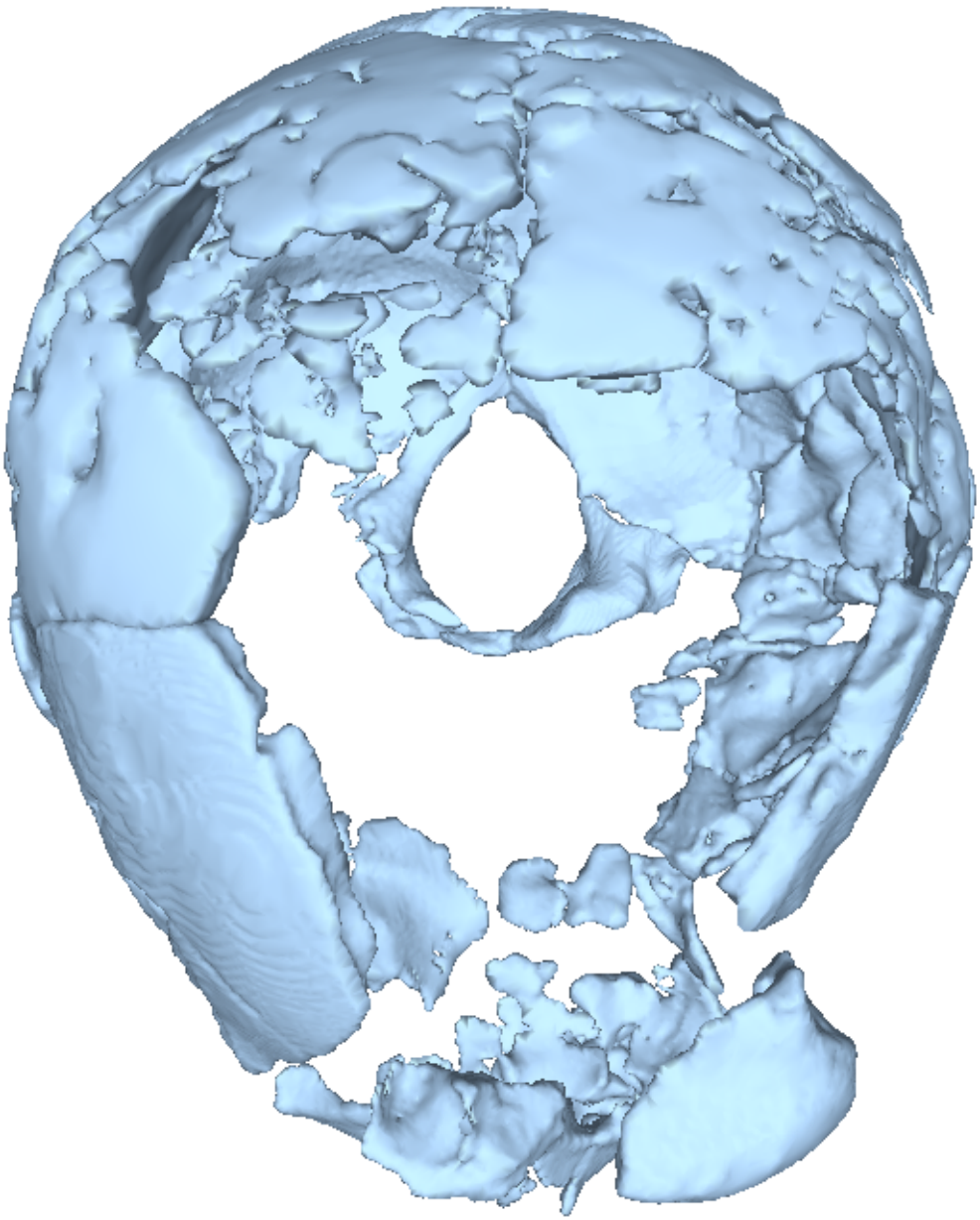

Figure 3.25: Reconstruction of the Ndutu cranium using fixed landmarks and sliding surface semi-landmarks to align the supra-orbital fragment and fixed landmarks to position the facial skeleton fragment cluster, vertical view.

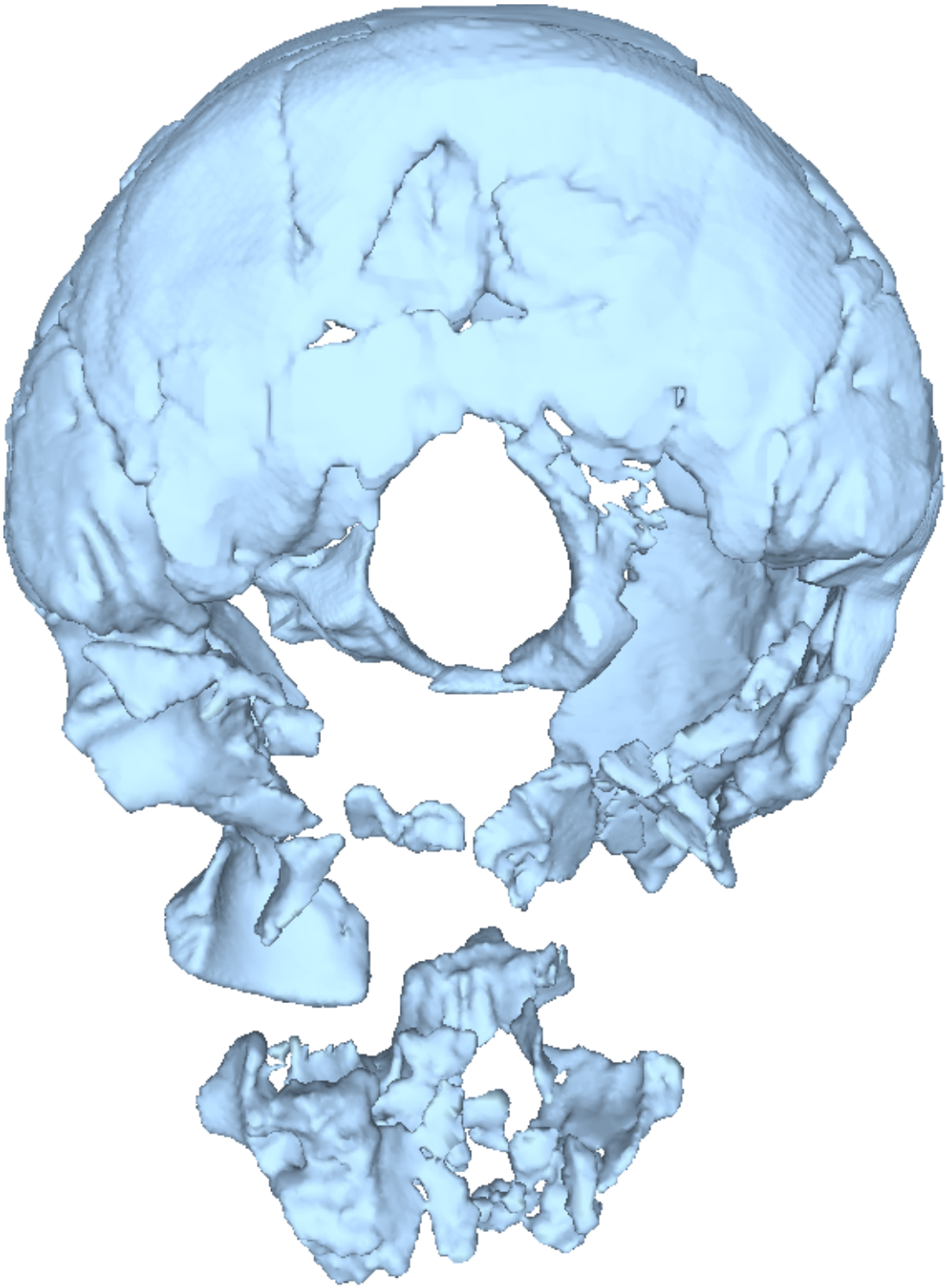

Figure 3.26: Reconstruction of the Ndutu cranium using fixed landmarks and sliding surface semi-landmarks to align the supra-orbital fragment and fixed landmarks to position the facial skeleton fragment cluster, basal view.

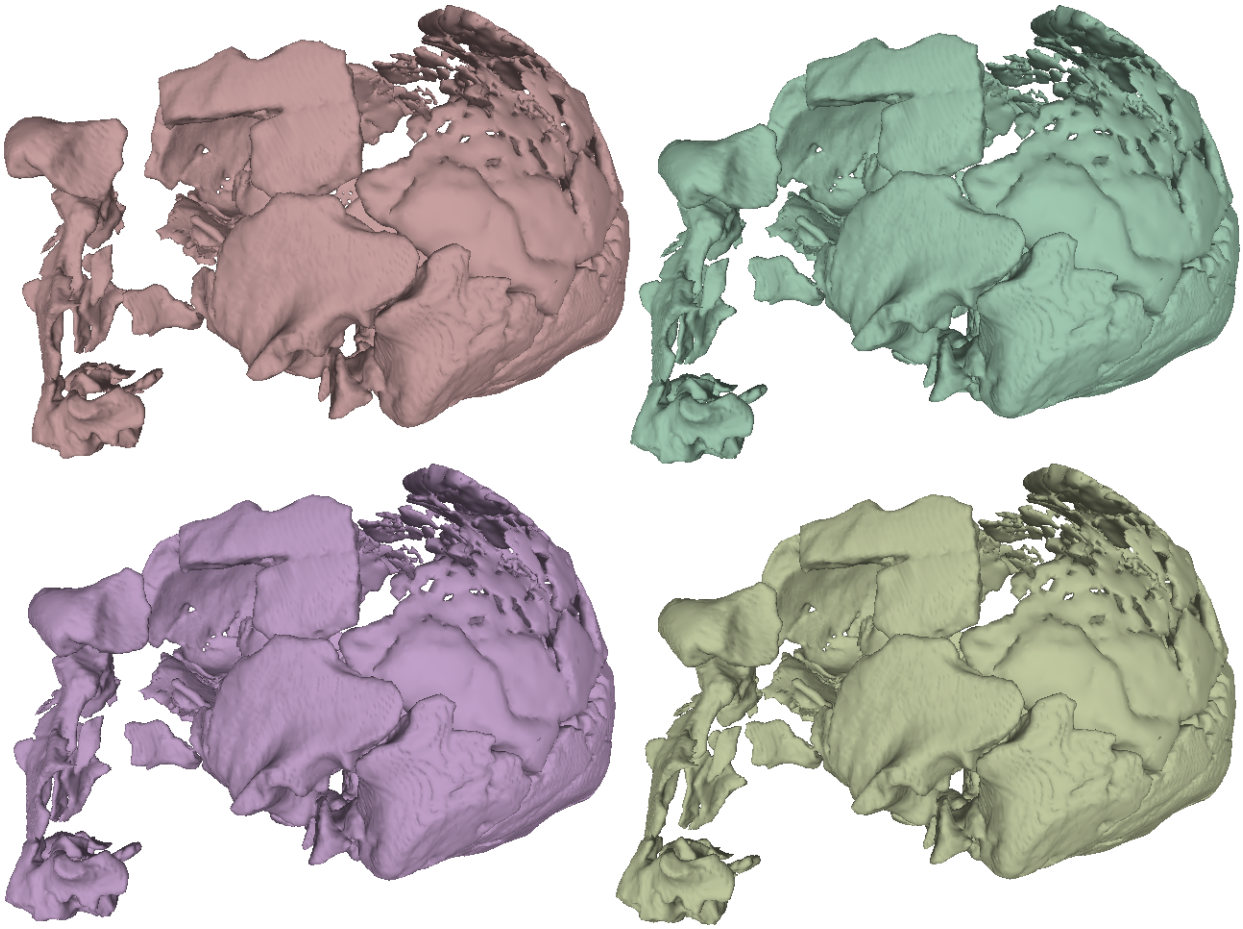

Figure 3.27: Alternative reconstructions of the Ndutu cranium, left lateral view. a, Recreation of Clarke's reconstruction; b, *semi-landmark based alignment of the supra-orbital fragment using Irhoud 1 as the template and fixed landmark-based alignment of the facial skeleton using a consensus shape template (*Ndutu_MIX*)*; c, *fixed landmark-based alignment of both fragments using a consensus shape template (*Ndutu_M*)*; d, *fixed landmark-based alignment of both fragments using Irhoud 1 as the template (*Ndutu_T*)*.

In all reconstructions, the unarticulated fragments are located at a sound distance from the rest of the preserved portions of the cranium. They are also correctly positioned along the mid-line, thanks to the *dta()*'s reflection and relabeling sub-process (Profico et al., 2019). The position of the facial skeleton in all reconstructions still agrees with that of the lesser and greater wings of the sphenoid, as intended by Clarke (1990).

Although the differences are relatively modest, when compared to the Clarke's reconstruction (as recreated for this project), all of the reconstructions display a lower, more prognate facial skeleton, specially the template based reconstruction *Ndutu_T*. Consequentially, the basicranium is also less flexed. As mentioned before, the cranial vault is also moderately narrower, albeit this is further acentuated towards the front. Perhaps the most notorious difference is that the supraorbital is lower and less forwardly projected in all of the reconstructions when compared with Clarke's.

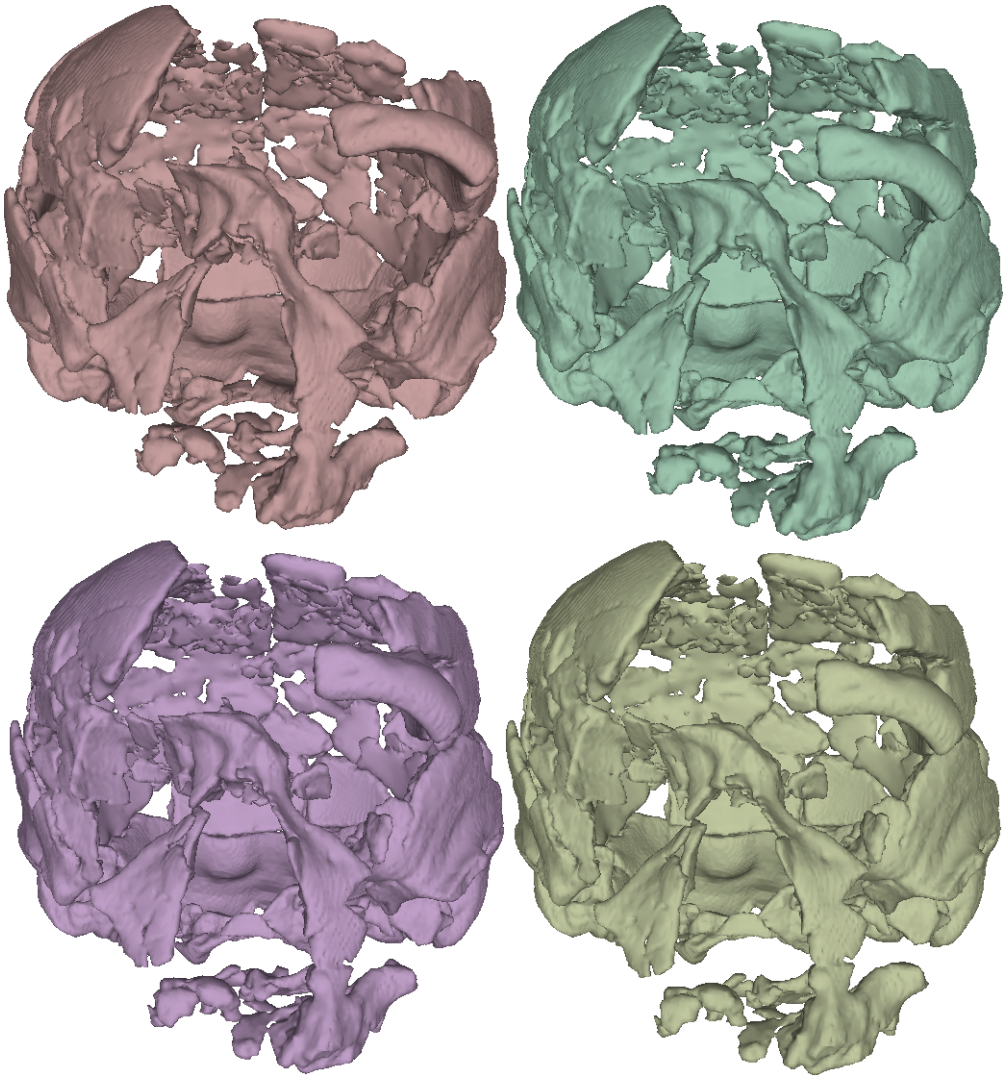

Figure 3.28: Alternative reconstructions of the Ndutu cranium, frontal view. a, Recreation of Clarke's reconstruction; b, *semi-landmark based alignment of the supra-orbital fragment using Irhoud 1 as the template and fixed landmark-based alignment of the facial skeleton using a consensus shape template (*Ndutu_MIX*)*; c, *fixed landmark-based alignment of both fragments using a consensus shape template (*Ndutu_M*)*; d, *fixed landmark-based alignment of both fragments using Irhoud 1 as the template (*Ndutu_T*)*.

In particular, the *Ndutu_MIX* reconstruction displays a slightly lower and laterally projecting supra-orbital than *Ndutu_M*. Consequentially, the facial skeleton fragments are also only minutely further down and closer to the cranial vault. They are also modestly rotated clockwise about the antero-posterior axis.

Unlike the mean shape-based reconstruction *Ndutu_M*, the one produced using Irhoud 1 as the template produced a less projecting supra-orbital. As a matter of fact, *Ndutu_T* displays the lowest, most restrained supra-orbital of all alternative reconstructions. The facial profile of *Ndutu_T* is also more prognate than *Ndutu_M*, imitating that of Irhoud 1. Additionally, in *Ndutu_T* the facial skeleton fragment cluster appears rotated counterclockwise about the antero-posterior axis.

3.3 Principal Component Analysis

3.3.1 Proportion of the variation explained by the principal components

The eigenvalue histogram or scree plot in Figure 3.29 clearly shows that most of the variation in the sample is described by PC 1 and PC 2. A clear inflection point can be observed between PC 1 and PC 2, after which most PCs cover similar (although decreasing) proportions of the variation. This indicates that the first two discernibly constitute the components which are most biologically meaningful. PC 1 accounts for 21.25% of the variation, while PC 2 describes 10.46% of it.

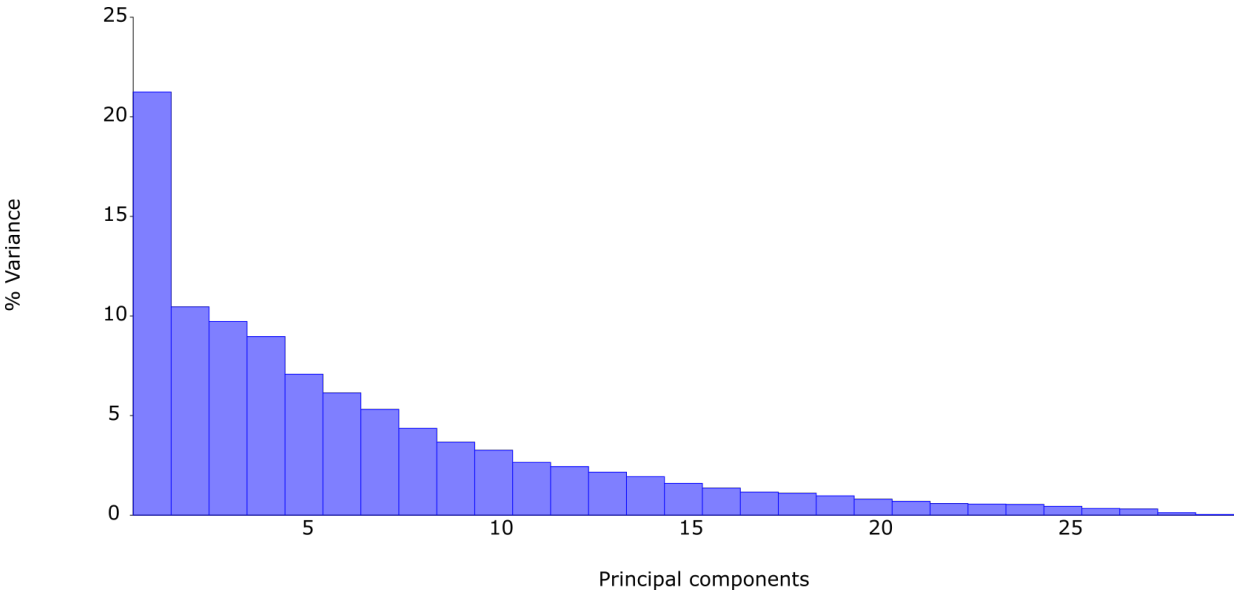

Figure 3.29: Histogram of the principal components (eigenvalues).

3.3.2 Shape changes across the principal components

Based on what can be elucidated from the superposed wire frame graph in Figure 3.30, changes along PC 1 describe cranial length, anterior and posterior width. This is denoted by the direction of the vectors in *lambda* (No. 28), *inion* (No. 29), *asterion* (No. 22 and 27), *stephanion* (No. 23), and *sphenion* (No. 19 and 24).

Most importantly, PC1 also captures changes in cranial flexion, prognathism/orthognathism, and supra-orbital constriction. In lesser proportion, it also accounts for the shape and the distance between the inner and outer contours of the section of the dental arcade that is preserved in the Ndutu cranium, as shown by the vectors departing from landmarks No. 1 to 7 and No. 31 (the lateral glenoid point).

Traits associated to the orbits, including supra-orbital torus projection or retraction appear to be related to this PC too. The points registering the position of the fronto-zygomatic suture and the supra-orbital margin - i.e. the *frontomalare orbitale*, *frontomalare temporale* points (No. 17 and 18), and the mid-torus inferior point (No. 12) - move forward or backward across the sample.

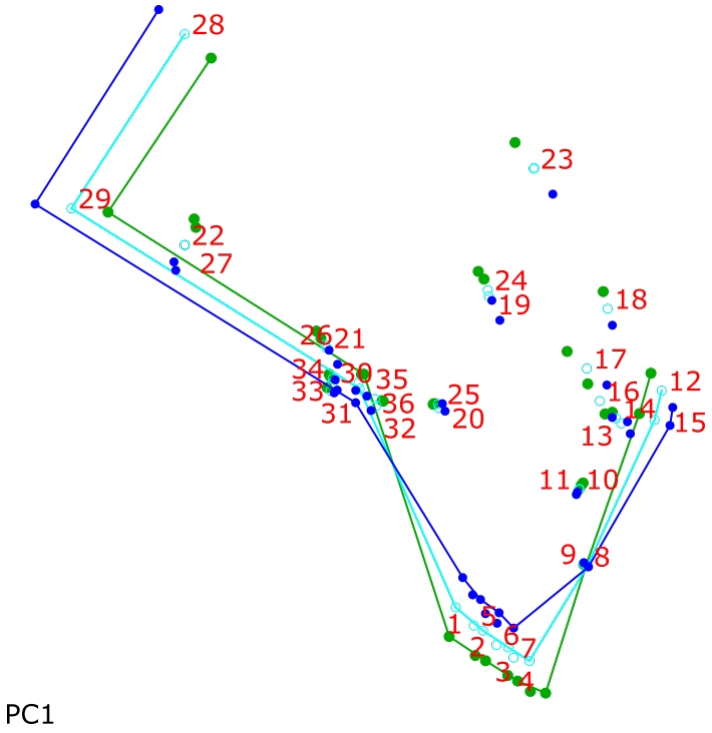

Figure 3.30: Shape variation along Principal Component 1. Lateral view. The green line corresponds to a negative (-0.1) scalar factor, while the blue line is a positive (0.1) scalar factor. Hollow circles and light blue lines are the sample mean.

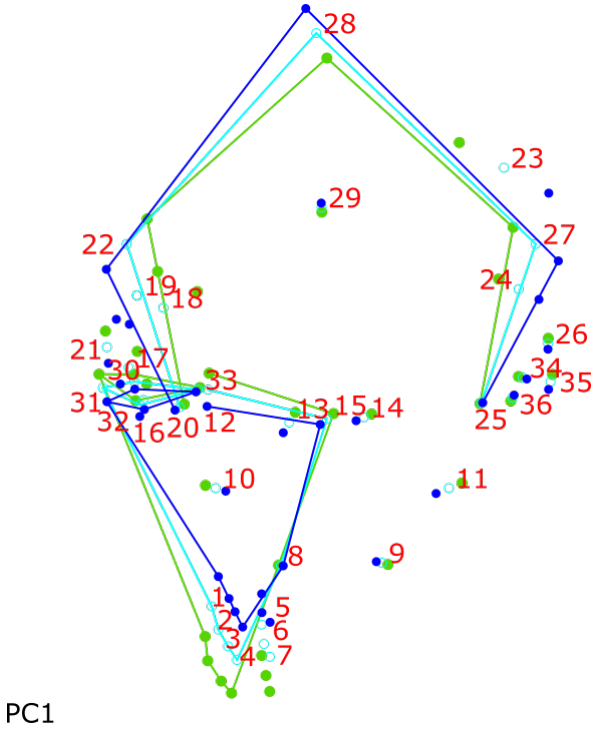

Figure 3.31: Shape variation along Principal Component 1. Vertical view. The green line corresponds to a negative (-0.1) scalar factor, while the blue line is a positive (0.1) scalar factor. Hollow circles and light blue lines are the sample mean.

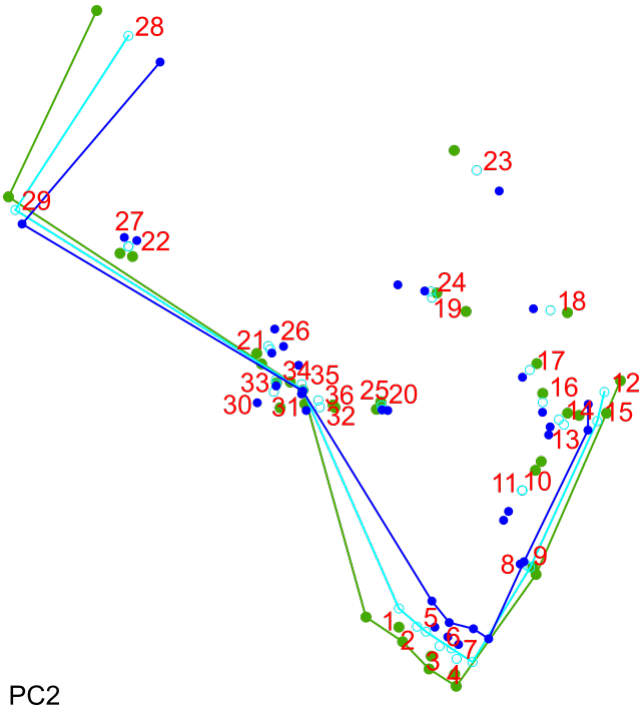

Figure 3.32: Shape variation along Principal Component 2. Lateral view. The green line corresponds to a negative (-0.1) scalar factor, while the blue line is a positive (0.1) scalar factor. Hollow circles and light blue lines are the sample mean.

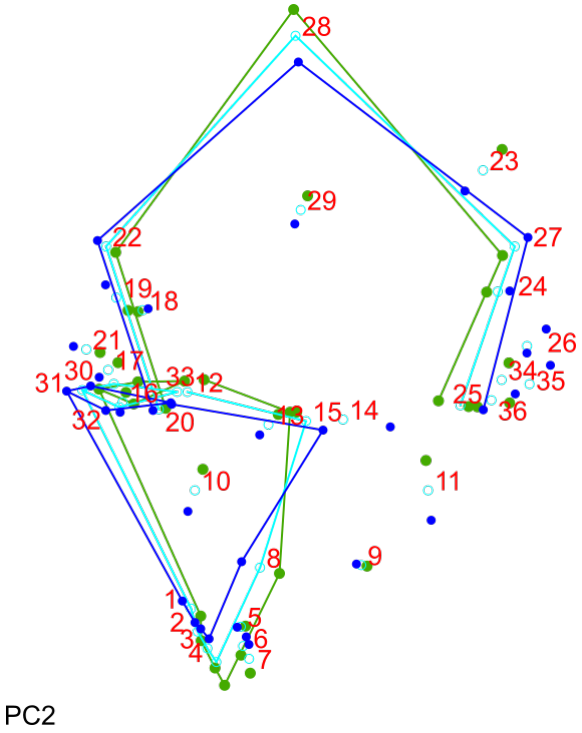

Figure 3.33: Shape variation along Principal Component 2. Vertical view. The green line corresponds to a negative (-0.1) scalar factor, while the blue line is a positive (0.1) scalar factor. Hollow circles and light blue lines are the sample mean.

In the other hand, PC 2 (Figures 3.32 and 3.33) depicts changes in inter-orbital width, which varies largely across the sample given the changes in the location of the left and right *maxillofrontale* points (No. 13 and 14). Other landmarks also move downward and away from the top of the cranium. Changes in temporo-mandibular joint width can also be discerned along this component, although some variation on the forward/backward projection of the lateral edge of this joint can also be seen in PC1. However, one of the most conspicuous changes along PC 2 is perhaps the position of *lambda* (No. 29), which may be explained by differences in the angle between the nuchal (not observable) and occipital planes in the sample. Facial projection and facial height are also notably variable along this PC (although the latter could be related to preservation).

3.3.3 Principal component scores

Figure 3.34 shows the specimens scattered according to their PC scores in PC 1 and PC 2. Here, their proximity is an indication of their similarity in terms of overall shape. A notable fact is that using a landmark set based on the preserved anatomy of the Ndutu cranium, differences among specimens akin to the Neanderthal or sapient lineage, or between Middle and Late Pleistocene, and Eurasian and East Asian specimens are not immediately obvious. The underlying implication of this is that the position of the landmarks found in the Ndutu specimen are of lesser value than other traits when trying to group these hominins.

In relation to the other specimens in the reference sample, the alternative reconstructions of the Ndutu cranium appear to be quite close to the mean in terms of PC1, with the template-based reconstruction being the closest. Regarding this, it is likely that this is a consequence of the method employed, since Irhoud 1 is also nearly in the middle of the range of PC1. Either way, all reconstructions are on the upper right quadrant of the scatter plot, which indicates that they have a slightly longer neurocranium, a shorter, higher positioned, and less projected splachnocranium, and a less flexed neurocranium.

Solely in terms of the shape outlined by the 37 fixed landmark set defined in Section 2.2.2, all of the Ndutu reconstructions are closest to the Irhoud I fossil, regardless of the reconstruction methodology. The Sima de los Huesos 5 is also notably more similar to Ndutu than the rest of the hominins in the sample. However, considering only what can be discerned from the position of the fixed landmark set used for this project, the the Ndutu cranial vault is antero-posteriorly shorter and posteriorly wider than Irhoud 1. It also anteriorly narrower, it exhibits a lower *inion* and a slightly more anteriorly positioned *lambda*. Meanwhile Miguelón possesses an antero-posteriorly narrower, more horizontally oriented glenoid fossa than Ndutu.

While strictly contingent to the landmarks chosen for it, the results of this analysis suggest that Ndutu is affine to early representatives of the sapient lineage. Nevertheless, a thorough contrast with other available evidence, with special attention to the metric and non-metric traits displayed by these crania and their interpretation, should further clarify Ndutu's correspondence to this stock.

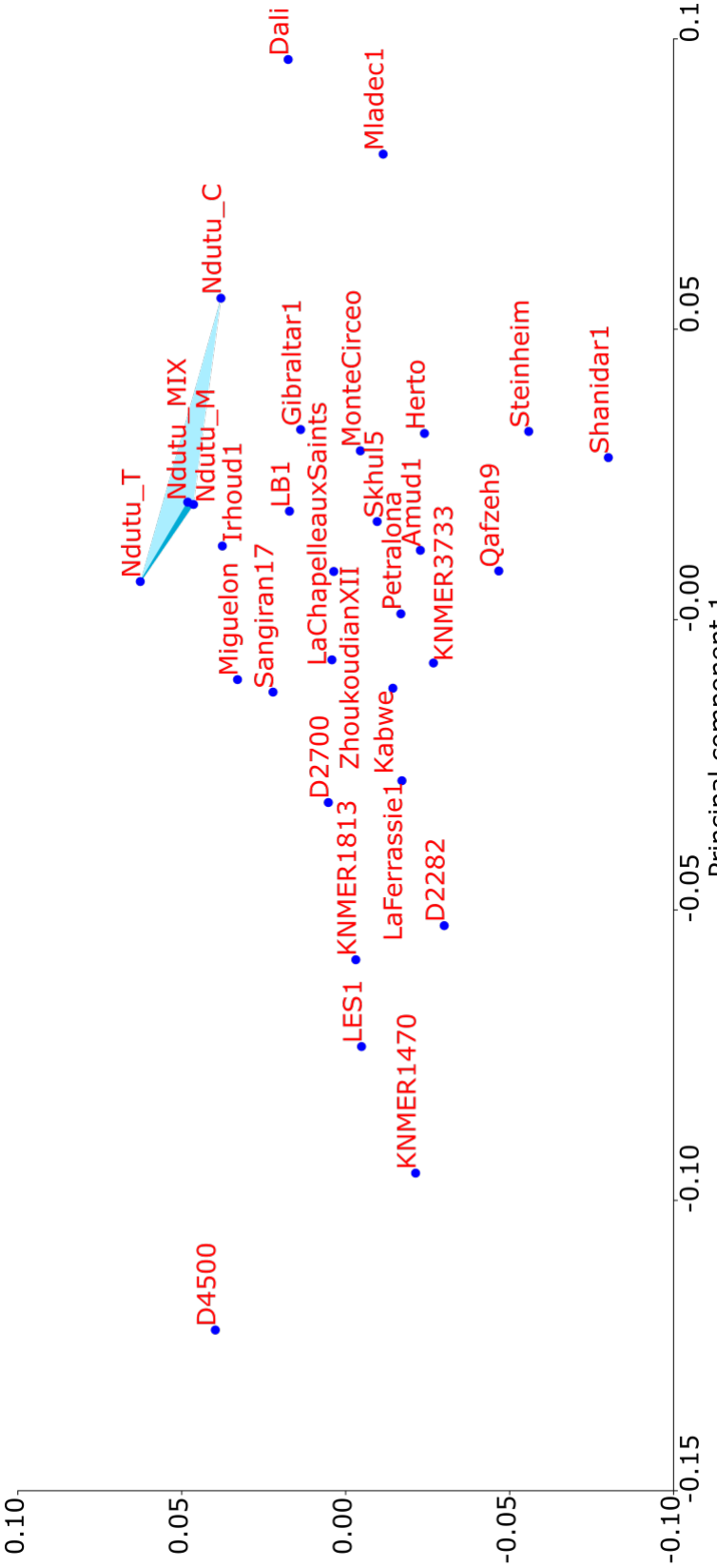

Figure 3.34: Principal component scores in PC1 and PC2 of the specimens in the sample used for the reconstruction of the Ndutu cranium's disarticulated fragments. *The light blue area indicates the region of morphospace between the alternative reconstructions of the Ndutu cranium, including Clarke, 1990. The smaller teal area signals the region covered by the virtual reconstructions presented in this work.*

Chapter 4

Discussion

4.1 Digital Restoration Strategy

From the moment they are deposited on the ground, throughout their entire taphonomic and diagenetic trajectory, the excavation, collection, and preparation processes, and (I add) the incidents that may arise while they are in display or even simply stored, the remains of our long past ancestors will inevitably become disarticulated, fragmented and/or distorted (Lautenschlager, 2016). There is a calming effect in spending hours inside the laboratory attempting to mend these artifacts and even some level of craftsmanship in doing so by hand. Notwithstanding, albeit possibly unavoidable to a certain degree, these frivolities frequently come at the cost of being partial to the restorer's assumptions.

Both in 1976 and in 1990, Clarke explained how he followed straightforward and well-established criteria to reconstruct the Ndutu cranium (see Section 1.2). He estimated the position of the unarticulated fragments using his knowledge about human anatomy and his experience observing, measuring and reconstructing hominin fossils. Yet, in terms of being able to base the position of these discontinuous fragments solely on this previously acquired information, his tool set was limited.

In the recent decades, much has been developed to attempt to construct a *bias-free* bridge between this experience and reconstruction/reconstruction tasks (see Section 1.5). Several works evidence the paleoanthropological community's will to revisit previous efforts (for example Profico et al., 2019; Di Vincenzo et al., 2017). In this work, I further tested and applied an already established method to use the information extracted from a sample of hominin crania to estimate the position of discontinuous fossil remains.

To perform that task, I had to first apply two simple and entrenched principles of traditional physical manual reconstruction (break surface correspondence, anatomical position) in a virtual setting to prepare a piece of the cranium which, although integrated by continuous fragments, had been separated into various uneven ones. It is overly likely that these criteria were the same as Clarke's, even though he only explicitly mentioned that he considered their approximate anatomical relationships (Clarke, 1976).

However, the application of a global energy reduction function on 58 paired points along corresponding fragment surfaces produced a model that diverged from Clarke's reconstruction in the sense that it possessed a wider frontal bone and, consequently a rounder outline when viewed from atop. This last observation is particularly transcendental because it bestows on the Ndutu individual a neurocranial morphology that splits from the *H. erectus/ergaster* pentagonal contour (see Clarke, 1976, 1990).

It is also tremendously determinant because this reassembled neurocranium was the base of the later digital alignment. Still, as illustrated in Section 1.5, the global energy reduction function is one of many analogous optimization algorithms widely used for reconstruction purposes, which lends confidence to the method followed here.

In 1976 and in 1990, Clarke stated that he used the preserved greater and lesser wings of the sphenoid as a guide when approximating the position of the facial skeleton fragments. To my own dismay, I was not able to consider this bone's morphology when aligning the Ndutu facial skeleton.

In an ideal setting, access to hominin crania CT-scans would have allowed to place landmarks on this and many endocranial structures while maintaining a reasonable sample size, yet their scarcity made this unfeasible. Thus, spatial relationships between the unsampled endocranial anatomy and this fragment cluster were a major concern while assessing the results of the final digital alignment. Fortunately, all of the products of the application of the *dta()* tool selected on the basis of the results of the tests undertaken for this project were in sound agreement with the preserved portions of the sphenoid.

To determine the best approach to reconstruct the Ndutu cranium I performed a series of tests and analyses whose results apparently contradict the conclusions of the tool's original publication. In 2019, Profico and colleagues reported that the *dta()* performed best when an individual of the same sex and taxonomic attribution was used as a template for the alignment based on the application of the algorithm in a sample of extant non-human primates. Yet, on tests No. 2, 7, and 8 I explored the possibility of not choosing a particular specimen as the template for the reconstruction of the Ndutu facial skeleton and supra-orbital fragment positions and using a sample consensus landmark configuration instead. The idea behind this came after taking into account the available literature.

Few publications agree upon which fossil the Ndutu cranium's morphology is closest to. In 1976, Clarke implied that, although clearly documenting a more primitive status than Ndutu, the Zhoukoudian III cranium was most similar. Later, in 1983, Rightmire nominated the Kabwe, Elandsfontein and Bodo - only the first of which could be included in this sample. Clarke argued that the closest specimen was either Steinheim (also in this project) or Salé in 1990(an incomplete specimen that would later be proven to be pathological (?, ?)). In 2016, Stringer proposed that the Ndutu cranium resembled Thomas Quarry the most. Still, after some time Rightmire insisted in relating this specimen to Kabwe (G. P. Rightmire, 2017).

Even when my approach was clearly distinct, I expected the *dta()* tool to pick Steinheim, Kabwe or even Zhoukoudian as the template. Despite this, the program used Irhoud 1, a specimen already known before the Ndutu specimen had been unearthed. Although this result merited discussion (which will ensue in the following pages), what followed was asking: *What if the best template was among the partial or unaccessible specimens nominated in the literature (like Zhoukoudian III, Elandsfontein, Bodo, Salé or Thomas Quarry)? What if instead I chose neither of the specimens in the sample in particular? How imprecise would doing that be?*

Test No. 2 implied that not choosing a particular individual as a template improved the tool's performance. Although the data obtained for the Amud 1 cranium suggested that in the case of hominin fossils choosing a specimen or the mean as a template returned largely similar errors, the averaged results and the method effect analyses suggested otherwise. This seeming contradiction with Profico *et al*'s work becomes less striking when one considers the variability of the samples used on each work. The test sample from which they extracted these conclusions included twelve genera (namely, *Alouatta*, *Ateles*, *Cebus Gorilla*, *Homo*, *Hylobates*, *Macaca*, *Pan*, *Papio*, *Pongo*, *Symphalangus*, and *Therapithecus*) from both suborders of Primates (hap-

lorhine and strepsirhine). Elseways, the individuals in this work's sample all belonged to the same genus, *Homo*. Therefore, it seems reasonable that aligning disarticulated fragments based on a template from the same genera will return relatively better results when aligning it using a specimen from a different order is a possibility.

On the other hand, although the accuracy of sex correspondent templates in hominin reconstruction may deserve some consideration, it is noteworthy that many non-human primates are remarkably more sexually dimorphic than our closest relatives. For example, some of the primate genera included in Profico and colleague's sample, such as *Alouatta*, *Gorilla*, *Macaca*, *Papio*, *Pongo*, and *Therapithecus* are strongly to extremely dimorphic both in body size and canine development. Only a few others display slight differences - for example, *Cebus* and *Hylobates* (Plavcan, 2001).

It is generally accepted that sexual dimorphism is reduced in genus *Homo*, even when compared with *Australopithecus*[1]. In fact, sexual dimorphism is significantly reduced from *H. erectus* and on, where male and female body sizes have been estimated to be only 1.2 standard deviations (SD) away from each other - in *H. sapiens* this distance reaches 1.1 SD (Grabowski, Hatala, Jungers, & Richmond, 2015). This further stresses that some of Profico *et al*'s conclusions may not be extensible to less variable samples. Furthermore, the Ndutu individual's sex is not an uncontended matter (see Section 1.3).

Another unforeseen ramification of the tests was the poor performance of tool under the application of symmetrization constrains. Even when Profico and colleagues (2019) explain that the tool relabels and reflects the landmarks to mitigate the impact of asymmetry, undergoing the "optional symmetrization process" detailed in the Arothron package manual (Profico et al., 2018) produces aberrant results. This issue may be, nonetheless, explained by the asymmetrical nature of the landmark set itself, given that it contained very few paired bilateral landmarks on the facial skeleton fragment cluster.

Tests No. 4, 5, 6, and 8 all included surface semi-landmarks in the data. The results of those tests permitted the presentation of a reconstruction of the Ndutu cranium that employed the approaches that generally induced least errors. Profico and colleagues also presented a sliding surface semi-landmark-based reconstruction of the Amud 1 cranium alongside a fixed landmark-based one. However, they did not explicitly endorse either.

As stated in Chapter 1, the expected result was that a surface semi-landmark-based reconstruction with a consensus shape template would produce smaller errors because sliding surface semi-landmarks allow to sample more broadly, which makes it possible to capture the morphological signal hidden in the curves of otherwise featureless bones. This includes traits such as parietal bossing, which recurrently appears in the literature (see Chapter 1).

Woefully, even when the use of sliding surface semi-landmarks alongside a consensus shape-based template seemed to improve the performance of the tool when aligning the landmarks in the left supra-orbital fragment, the follow-up analyses revealed that their combined effect did not significantly influence the restoration error. Moreover, when attempting to estimate the position of the facial skeleton, the error rose greatly. The best results were obtained when just employing a consensus shape-based template to align the facial landmarks, while using sliding semi-landmarks and nothing else worked better for the supra-orbital fragment.

The take-away of this observation is that different data management methods achieved the best possible performance when using the *dta()* to restore each fragment. Upon consideration

[1] Although newer works have suggested otherwise, for example, Reno and colleagues (2003) posit that, after adjusting skeletal measurements for temporal and geographical variance, *Australopithecus afarensis* exhibits similar sexual dimorphism to *H. sapiens*.

of Gunz et al.'s (2009) outlines, I posit that the notions of integration and modularity offer an option to interpret these results. Integration is defined as the ontogenic inter-relatedness and co-dependence between traits or modules that are interconnected by means of genes, developmental mechanics and spatial relationships (Lieberman, 2011). On the other hand, modules are highly integrated anatomical and functional units that are evolutionarily persistent (they appear repeatedly in the fossil record) and respond to independently to selection (Müller, 2007).

In previous literature, the human cranium has been divided into at least two major modules: the neurocranial and the orofacial module. In Cheverud, 1982, these modules are subdivided into distinct sub-units constituting functional matrices (packed and made up of the tissues and spaces necessary to perform a common function (Lieberman, 2011)). These include as the frontal, parietal and occipital for the neurocranium, and the frontal, orbital, nasal, oral and masticatory sub-units for the orofacial one.

Other authors distinguish different modules. For example, M. Sardi, F. Ventrice, and F. Ramírez (2007) discriminate between the cranial vault and base and appoint other names to them, such as anteroneural, midneural, and posteroneural (for the occipital, excluding the cranial base) for the cranial vault, and optic, respiratory, masticatory, and alveolar for the face. Some authors discern *modularized* traits based on their changes across specimens in GM studies. Basicranial flexion, facial retraction, cranial globularity and masticatory aparatus shape and position were recognized by R. González-José in (2008) who used Skelton and McHenry's trait definitions (see Chapter 1) to identify trends in hominin evolution.

Modules are complex developmental and evolutionary units. Their physical appearance (the phenotype) is a product of the set in motion of development mechanisms that are consistent across their evolutionary trajectory. Innovative traits (apomorphies) in their evolution arise from changes in the way in which these mechanisms interact, as well as in the timing of said interactions. Changes in this *ontogenic program* can alter the start, direction and intensity of the growth of the structures that integrate them, thus producing the observed morphological diversity (Zollikofer, 2012).

This can occur because the production of a phenotype depends on a number of interacting factors. Genes contribute to the construction of the phenotype through a development regulating machinery that is structured in a hierarchical fashion. Specifically, high hierarchy genes promote or inhibit growth and cell differentiation in the embryo through co-dependent circuits. This is why modifications to the sequence of these genes can cause changes in the components of the phenotype - this is the primary creative force responsible for the appearance of apomorphies (Müller, 2007).

Yet other factors are involved in a convoluted interplay with this genetic control. For example, modules in the cranium are tightly packed sub-units that co-vary because elements growing within and outside them interact with each other mechanically in confined space. Many of the cells integrating the tissues of the human head start in the axial embryo where their growth and differentiation (*morphogenesis*) is coordinated by high hierarchy genes known as *Hox* genes (Lieberman, 2011).

Cells coming from the neural tube, mesoderm, surface ectoderm, gut tube, and neural crest migrate to form the neural placodes and the branchial arches, which ultimately form the various structures in the face. As they travel to their positions, they experience change inducing interactions with the cells they encounter. Similarly, structures in the cranial base form exclusively from the paraxial mesoderm and the neural crest - the latter responsible for conforming the anterior cranial base (Nie, 2005). On the other hand, the growth of the bones in the cranial vault is induced by tension in dura mater as the brain grows, which causes fibroblast growth factor 2

(Fgf2) to be secreted (Lieberman, 2011).

Research into the interactions at the genetic, celular, tissular, organic (but also organismal and environmental) levels between ontogenic mechanisms such as the ones exemplified before, is the core of evolutionary-developmental biology. Its research agenda offers a mechanistic approach to understanding evolution (Müller, 2007).

Modules are, thus, not discrete units; they are interconnected with each other, albeit more correlated within themselves than with other modules (Cheverud, 1982). For example, relative brain size has been long hypothesized to influence cranial base flexion. In fact, it has been posited before that, considering the diversity in cranial flexion among Middle and Late Pleistocene *Homo*, that a single shift in the *ontogenic systems* relating and within these modules may have been responsible for the divergence between the Neanderthal and sapient lineages *lieberman2002*.

Bastir and colleagues (2010) have additionally lent support to the notion that facial size also plays an important role in determining basicranial morphology. Upon observation that the Neanderthal cranial base is less flexed that of *H. sapiens* despite having similarly sized brains, they argue that facial shape and size increase the angle formed by *basion*, the *sella turcica*, and the posterior nasal spine. Thus, it is accepted that, in *Homo* evolution, while brain size and consequent cranial base expansion are associated with a greater degree of cranial flexion, as facial size (particularly, its elongation) increases, so does the distance between the temporo-mandibular joint and the dental arcade, and, consequentially, the flexion decreases (Lieberman, 2011).

In light of the aforementioned tests' results, what this implies is that a possible explanation for the fact that sampling the cranial vault and base only produced better results when estimating the position of the supra-orbital in sample-wide tests is, firstly, that some of the surfaces whose morphology was recorded with semi-landmarks belong to the same module (and/or functional matrix) and are considerably close to the landmarks found in that fragment. If in the Ndutu supra-orbital's digital alignment procedure several semi-landmarks are located on the frontal bone (which would be part of the anteroneural module) it can be assumed that the result boasts a similar degree of precision.

Secondly, given that the relation between the alveolar and nasal modules in the facial skeleton fragment cluster and those in the cranial vault is not straightforward, as noted by Bastir and colleagues, it is not surprising that adding landmarks on the frontal bone, occipital and (even in lesser quantity) on portions of the left parietal reduces the capacity of the *dta()*'s algorithm to estimate the position of the facial skeleton. For this case, I posit that it is the landmarks describing the characteristics of the temporo-mandibular joint, part of a module that extends into the face (the masticatory module), and those describing cranial base expansion who may be better predictors of these spatial relations instead. The fact that these landmarks are proportionally better represented in the fixed landmark set ratifies this and indicates that the same approach should not be followed for all fragments when reconstructing hominin crania.

4.2 Shape affinities of the Ndutu cranium

As a consequence of their similarities in respect to the temporo-mandibular joint, cranial base expansion, and, thus the position of the facial skeleton, the reconstruction obtained by combining the methodological approaches which furthest reduced reconstruction error resulted closest to the Irhoud 1 cranium. All of the alternative reconstructions of the Ndutu cranium lie in the

immediate shape space of this specimen, even when using a consensus shape template. The PCA undertaken in this work reveals that Ndutu also exhibits a nasal morphology that is closer to Irhoud 1 than other specimens. Additionally, the consensus-based reconstruction's supra-orbital constriction is in many ways much closer to Irhoud 1, despite not being based on it.

These results reminisce Stringer's interpretation of another Moroccan exemplar, the Thomas Quarry mandible, as being one of the few Middle Pleistocene fragmentary specimens exhibiting modern-like zygomaxillary morphology apart from Ndutu. Unfortunately, this mandible, attributed to *H. rhodesiensis* by Hublin, is lacking its condylar process (Raynal, Mohib, & Lefèvre, 2016) and no mandibles were recovered from Lake Ndutu to further extend this simile. It is still noteworthy that modern human-like dentition from the same site have been directly dated 501 $^{+}$94_76 Ka old (Raynal et al., 2010), close to the Ndutu cranium's antiquity.

The Irhoud 1 specimen was recovered by M. ben Fatmi from Djebel Irhoud, a cavity in a mine in Chemaia, about 60 Km east of the city of Safi, Morocco. It is an rather well-preserved eroded and edentulous cranium missing the greater part of the cranial base, the nasal cavity structures, those behind the dental arcade, the rear of the orbits, and the zygomatic arches. This specimen, alongside two more (Irhoud 2 and Irhoud 3) from the same site, was first described by Ennouchi between 1962 and 1969, who argued that they were closest to the Neanderthal lineage (Schwartz & Tattersall, 2005).

Yet, many researchers currently agree that their affinities lie with the sapient lineage. For example, both Freidline and Stringer seem to agree that the Irhoud 1 specimen displays the zygomaxillary morphology diagnostic of *H. sapiens* (Stringer, 2016). As mentioned in Chapter 1, in a now highly-cited publication Hublin (2017) listed evidence supporting a close relation with the early *H. sapiens* lineage, although he admitted that Irhoud 1 and other associated specimens carried some *primitive retentions*.

Perhaps the most intriguing of his observations is that the Irhoud specimens display an elongated cranial vault shape that is rather similar to Neanderthals. In a GM study of vault shape in the same publication, Hublin found that both Irhoud 1 and 2 are intermediate between recent humans and the areas covered by Neanderthals and Middle Pleistocene hominins in shape space. Particularly, it is the Irhoud 1 cranium who turned out halfway between the configuration observed in *H. neanderthalensis* and that of *H. erectus* in the second PC. Following this, Hublin posited the possibility that modern cranial vault shape evolved later within the sapient clade.

Another remarkable unfolding stemming from the GM analysis here presented is that the PCA indicated that among the closest specimens in terms of the distribution of the landmarks considered for the alignment was Miguelón (Figure 3.34 in Section 3.3). Considering the shape changes accounted for in PC1 and PC2, it can be maintained that Miguelón's proximity in shape space is explained by similarities in occipital morphology, as suggested by Arsuaga et al. (1997).

On a side note, a compelling observation arisen in a previous stage in the development of this work is that the template chosen when executing the *dta()* while using sliding semi-landmarks to sample occipital and frontal squama, alongside the preserved portions of the left parietal was once the Sima specimen. In fact, an early interpretation of this argued that Ndutu could share some features with a stock closer to the sapient-Neanderthal LCA. However, it was later revealed that the tool's choice was a consequence of the misplacement of the *frontotemporale* landmark (No. 18), which is located on the supra-orbital fragment, which holds only three other landmarks (hence the relevance of a single mishap). Additionally, Miguelón's lower occipital is notably narrower than Ndutu's, as indicated by their *lambda-asterion* chords in this work.

It is now clearer that Ndutu cranium may have exhibited a morphology most closely akin to

the sapient lineage. Although some differences are still evident (Figure 4.1), it can be attested upon visual examination the facial projection of the newly reconstructed Ndutu cranium, as well as the level of prognatism, are close to the range of *H. sapiens* even when this alignment is based on the sample consensus (although it should be stressed that the anterior part of the dental arcade is missing). Furthermore, the results of the GM study here, also indicate that the supra-orbital constriction can also be reasonably inferred to have been more similar to early *H. sapiens* than to Middle Pleistocene hominins. This particular trait deviates from list of criteria that in G. P. Rightmire, 2017 justified the inclusion of Ndutu in the same deme as Kabwe.

On the basis of supra-orbital projection, post-orbital constriction, facial projection and angulation, cranial flexion, and temporo-mandibular joint shape, the reconstruction resulting from this work positions this specimen as a representative of a population related to the Djebel Irhoud specimens. This being said, it remains true that other traits within that Rightmire's (2017), such as cranial vault height, cannot possibly have been affected by the reconstruction procedure and should thus be in good agreement his observations and those of other researchers siding with its belonging in a primitive stock.

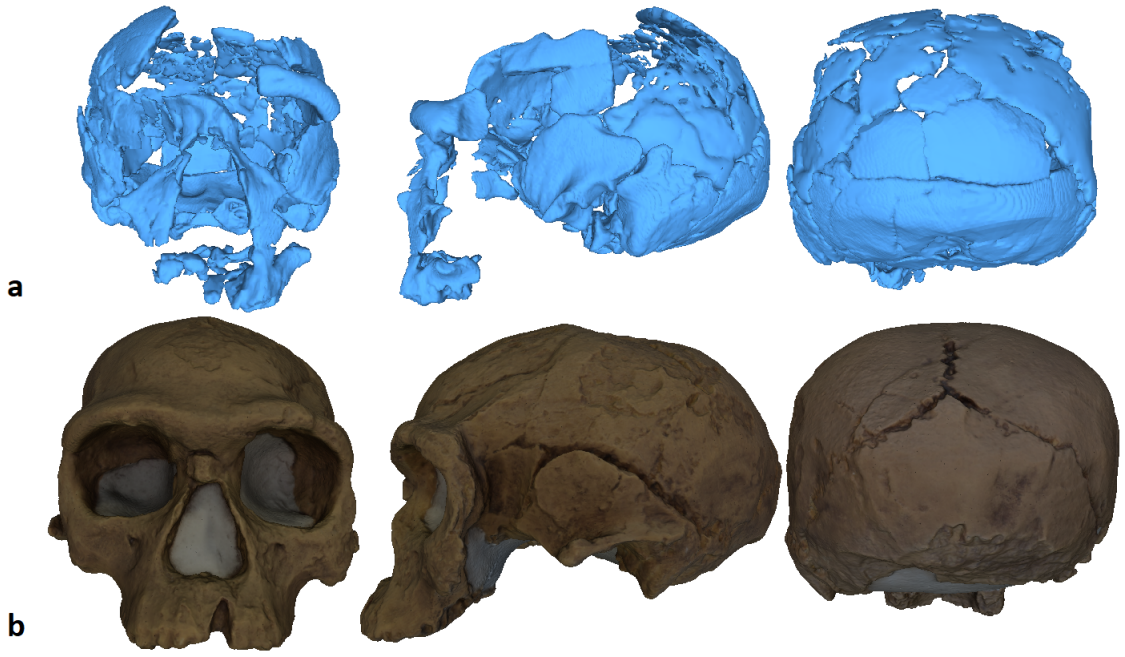

Figure 4.1: Frontal, left lateral, and nuchal view of the mixed approach reconstruction of the Ndutu cranium (a) and the closest specimen in the reference sample in terms of overall shape, (b) Irhoud 1. *The Ndutu cranium is not to scale.*

As briefly stated at the beginning of this composition, Lautenschlager (2016) impeccably warns that the products of digital reconstruction efforts should be regarded as amendable hypotheses. Thus, it is imperative to admit that the current state of the Ndutu reconstruction is susceptible to improvement upon the advancement of the resources available and collaborator contributions. Yet, if the reconstruction hypothesis and the results of the GM analysis presented in this work are held, it may be tenable to extract that some traits akin to *H. sapiens* may have been already distributed across a wide range in Africa 450 Ka ago.

The limited results here dispensed appear consistent with an early onset of the divergence of the sapient branch (Figure 1.4 in Chapter 1). If this is the case, the Ndutu cranium can

be added to a conspicuously variable group of hominin fossils than have been interpreted to document *H. sapiens*'s deep and diverse roots across Africa. Such exegesis constitutes the pillar of the African multi-regional explanation for the origins of extant humans, as explained in the first chapter of this work. Yet, Scerri et al. (2018) have recently proposed additional lines of evidence. Firstly, they postulate that the regional nature of the MSA record may have arisen not only from the advent of *modern cognition* and its interaction with varied ecologies across the continent (as is more broadly accepted), but may also stem from the interplay with a older local heritage. Furthermore, they utter that genetic coalescence estimates approaching 1 Ma and the sundry and asynchronous panorama illustrated by paleo-environmental reconstructions also contribute to the underpinnings of this model.

Thus, the outcome of this work would lend further support to the conclusions of Bräuer, 1984; Clarke, 1990, and Stringer, 2016, but also Scerri et al., 2018. Nevertheless, it should be noted that, in the wider scheme, the presented outcome of the PCA here undertaken does not strongly support the notion that the Neanderthal and sapient lineages constitute discrete entities.

Of course, this inference is clearly and frankly limited by landmark choice, a decision guided by the availability of such craniometric points in the portions preserved in the specimen that constitutes the focus of this work, the Ndutu cranium. Alternative landmark sets or other approaches to the study of hominin cranial morphology may have a better chance of clarifying the affinities of all of the specimens in the sample.

Chapter 5

Conclusions

The Ndutu cranium is a valuable fragmentary fossil specimen excavated from Upper Acheulean strata dated c. 450 Ka BP (Manega, 1993) at the Lake Ndutu site, Tanzania (Mturi, 1976). Prior to its recovery, it was subject to taphonomic distortion, including plastic deformation, but mainly brittle deformation. Hence, it was reconstructed manually in 1976 by Clarke and then again in 1990 after the addition of newly found fragments.

The morphology of the remains has been studied and discussed by various authors (Clarke, 1976; Bräuer, 1984; G. P. Rightmire, 1983; Clarke, 1990; P. G. Rightmire, 1996; Arsuaga et al., 1997; Stringer, 2016; G. P. Rightmire, 2017). Its affinity to the *H. neanderthalensis*, *H. sapiens*, *H. heidelbergensis/rhodesiensis* and *H. erectus* evolutionary lineages has been discussed on the basis of occipital angle and curvature, temporo-mandibular joint, supra-orbital, and zygomaxillary morphology, as well as cranial height and globularity, among other metric and non-metric traits. However, several features like post-orbital constriction, supra-orbital projection, facial projection, prognatism/orthognathism, and cranial flexion remain unclear. The few ventured observations regarding them (G. P. Rightmire, 2017) seem to rely on a reconstruction of the position of the constituting fragments that was performed using a now outdated approach.

In consequence, the goal that I set out to achieve was to twofold. Firstly, to elucidate the most reliable strategy to reconstruct the position of the facial and supra-orbital fragments by determining the data and/or constrains that reduce the error in simulated reconstructions of each fragment in a sample of well preserved Pleistocene hominin crania using said digital alignment tool. Then, to ponder the consequences of the statistically informed reconstruction of the Ndutu specimen in terms of shape in comparison to a the same reference sample. I selected Profico et al.'s (2019) Digital Alignment Tool function (a landmark and template digital reconstruction resource, a.k.a. *dta()*) to estimate the position of the unarticulated fragments of the Ndutu cranium in the R statistical system environment, where I prepared a script (Appendix B) capable of managing the data and executing the tool.

To meet the requirements of this procedure, I prepared three 3D models representing fragment/fragment clusters by segmenting the CT-scans of the original fossil provided by Weber et al. (2005). One of these models, the one documenting the Ndutu cranium's base and vault fragments was reassembled using a well-established approach based on point-based matching of corresponding fragment surfaces and a global energy reduction optimization algorithm (the same process was later used to reassemble a digital version of Clarke's 1990 reconstruction). The process altered the orientation of the frontal bone fragments, rendering a moderately narrower frontal.

Subsequently, I gathered 26 3D models of well-preserved hominin crania. Ten of these were

replicas found at the IPHES Paleoanthropology Laboratory in Tarragona, Catalonia; they were digitized using photogrammetry. The rest were sourced from personal communications and online repositories. Based on the craniometric points observable in the preserved portions of the Ndutu cranium, I afterwards constructed a set of 36 fixed landmarks.

I iteratively registered these landmarks on all of the crania in the sample, each of the Ndutu cranial fragment 3D models, and the digital version of Clarke's reconstruction (missing landmarks were estimated using the TPS following Gunz et al., 2009). I measured the landmark registration accuracy and replicability using commonplace indicators, such as the ICC coefficient and Amqvist and Mårtensson's average repeatability, as well as a Procrustes ANOVA.

I tested the *dta()* function's accuracy when reconstructing the position of the landmarks in the Ndutu fragments by computing the mean landmark displacement per specimen after having superimposed it with its undisturbed self using a GPA - I dubbed this the *reconstruction error*. Upon observation of the results, I ran a series of seven subsequent two- and three-way ANOVA, and estimated marginal means tests to find the data and/or constrains that furthest reduced this error and improved the function's accuracy.

The results of these tests were mixed. Firstly, they varied per fragment, indicating the same approach bore different levels of accuracy for different sets of landmarks. Using semi-landmarks provided better results when aligning the supra-orbital fragment and the cranial base and vault fragment clusters. Employing only the fixed landmark set was best when aligning the facial skeleton fragment cluster with that of the cranial base and vault. In the latter case, more accurate results were obtained when using the sample consensus shape produced by a GPA as the template.

These results confirmed Gunz et al.' (2009) maxim that sanctions that all reconstruction procedures should be grounded on inferences and hypotheses about integration and modularity. They also constitute an example of hominin reconstruction distributions, an approach suggested by Lautenschlager (2016).

Using this information, I elaborated a reconstruction of the Ndutu cranium following a mixed hierarchical approach. I also created three alternative reconstructions ones. Using the resulting landmark coordinate matrices, I analysed the consequences of the procedure in terms of shape in relation to the hominins in the reference sample following well-established GM methods. I performed a GPA aligning the specimens in the sample using the biasterionic chord as a horizontal axis and the line parting from *lambda* that perfectly perpendicularly intersects it as the vertical axis. Then, I executed a PCA.

The analysis confirmed that all of the reconstructions of the Ndutu cranium had a lower positioned, more projected facial skeleton, a more prognate profile and an anteriorly narrower cranial vault than Clarke's 1990 reconstruction - other traits remained undisturbed. It also returned that the newly reconstructed Ndutu cranium was closest in terms of temporo-mandibular joint and occipital morphology, facial projection, level of prognatism, post-orbital constriction, and cranial flexion to the Irhoud 1 cranium. This is independent of the result of the alternative template specimen-based reconstructions.

These results shed light on the morphological affinities of the Ndutu cranium. In terms of what can be described with the landmark set employed in this work, the Ndutu individual possessed a morphology that is within the range of the early *H. sapiens* lineage. However, they also suggest a certain degree of ambiguity. Although this does not preclude the possibility of assigning it to said stock, it is conspicuous that, according solely to the landmarks in the set, this specimen resulted unexpectedly close in shape space to Middle Pleistocene hominins and pre-Neanderthals. Alternative approaches may better discriminate between both lineages and

Ndutu's correspondence to either one of them.

5.1 Future Work

In this thesis I have presented a statistically informed reconstruction hypothesis of the fragmented Ndutu specimen. The articulated fragments have been reassembled and the position of the disarticulated portions of the cranium have been estimated using a template-based methodology. However, in its current state, the Ndutu cranium still suffers from the effects of its troubled taphonomic history.

As noted by Clarke (1976, 1990), the right parietal has been subject to plastic deformation. A recourse to counteract this effect is the application of a retro-deformation algorithm. Still, if favoured, in an ideal setting this option would be preceded by thorough prior modelling (as in Di Vincenzo et al., 2017). The elucidation of a proper strategy to correct this distortion and the execution of such a study deserve a design of their own. A follow-up to this project should further delve into this challenge.

Among the results of the present endeavor, I have also rendered a GM-based morphological comparison of this reconstruction with respect to a sample of well-preserved hominin crania. The associations presented are based largely on the product of the followed virtual reconstruction methodologies, but they also reflect similarities in the relative positions of the landmarks chosen for this procedure between the sample subjects.

As stated previously, the landmarks designated for this project were chosen on the basis of their availability, both on the fragments composing the Ndutu cranium and on most of the reference sample. As explained in Section 2.2.2, to ensure the best conditions for the comparison, each landmark was allowed to be missing from a maximum amount of four sample specimens. Therefore, a considerable number of landmarks had to be excluded from the morphological analysis - for example, *opisthion* was unfortunately missing from most of the reference sample, for which the occipital angle had to be disregarded. Woefully, this implies that it is likely that the unexpected associations are a consequence of this partiality towards certain parts of the full scope of morphological evidence from both the sample and Ndutu her/himself.

Furthermore, it should be noted that the shortcomings of the approach to morphological comparison here followed are not restricted to what has been exposed in the last paragraph. As also noted in Section 1.5, locating discrete points along the surface of fossils bares the unavoidable loss of morphological information contained in the surfaces between them (Bardua et al., 2019). This hindrance is not only limited to the larger, otherwise featureless surfaces of the cranial vault, but can also fail to grasp the nature of smaller, more complex areas.

Slight but meaningful changes in bone surface, such as hyperostosis, hypostosis, accessory foramina, canals, grooves or sutural variations, often escape the reach of single or even multiple landmark coordinates. Such features are intrinsic to non-metric traits, a suite of known complex characteristics with proven relevance when distinguishing between human populations (White et al., 2012). An example of this is Clarke's (1990) observation of an elevated articular tubercule in Ndutu's pre-glenoid plane, a feature associated with *H. sapiens* that was not recorded by the landmark set in this project.

Therefore, it seems reasonable to posit that alternative approaches to morphological study, such a non-metric-based comparison of the crania in the sample, may bear the discriminating power still lacking from this GM-based study. Further work on the present line of research could benefit from the incorporation of these techniques to ascertain the affiliation to distinct

lineages, such as the sapient or Neanderthal ones. Nonetheless, it should be pointed out that non-metric methods have been criticized on the basis of their scoring standards, discrete nature and homology (White et al., 2012). Thus, future work should also tackle these possible drawbacks.

References

Aber, J. S., Marzolff, I., Ries, J. B., & Aber, S. E. (2019). Chapter 3 - principles of photogrammetry. In J. S. Aber, I. Marzolff, J. B. Ries, & S. E. Aber (Eds.), *Small-format aerial photography and uas imagery (second edition)* (Second Edition ed., p. 19-38). Academic Press. Retrieved from https://www.sciencedirect.com/science/article/pii/B9780128129425000033 doi: https://doi.org/10.1016/B978-0-12-812942-5.00003-3

Adams, D., Collyer, M., Kaliontzopoulou, A., & Baken, E. (2021). *Geomorph: Software for geometric morphometric analyses. r package version 4.0.* Retrieved from https://cran.r-project.org/package = geomorph

Agisoft LLC. (2017). *Agisoft photoscan standard (version 1.4.0) (software).* (Preview release)

Andrews, P., & Williams, D. B. (1973). The use of principal components analysis in physical anthropology. *American Journal of Physical Anthropology*, *39*(2), 291-303. Retrieved from https://onlinelibrary.wiley.com/doi/abs/10.1002/ajpa.1330390220 doi: https://doi.org/10.1002/ajpa.1330390220

Arbour, J. H., & Brown, C. M. (2014). Incomplete specimens in geometric morphometric analyses. *Methods in Ecology and Evolution*, *5*(1), 16–26. doi: 10.1111/2041-210x.12128

Arsuaga, J. L., Martınez, I., Gracia, A., & Lorenzo, C. (1997). The sima de los huesos crania (sierra de atapuerca, spain). a comparative study. *Journal of Human Evolution*, *33*(2-3), 219–281.

Autodesk, I. (2010). *Sculpting overview.* Autodesk Inc. Retrieved from https://download.autodesk.com/us/mudbox/help2010/index.html?url = WS1a9193826455f5ff6026605b1181c8f4f2e-1e05.htm,topicNumber (Accessed on 05.5.2021)

Bada, J. L. (1987). Paleoanthropological applications of amino acid racemization dating of fossil bones and teeth. *Anthropologischer Anzeiger*, *45*(1), 1–8. Retrieved from http://www.jstor.org/stable/29539748

Bardua, C., Felice, R. N., Watanabe, A., Fabre, A. C., & Goswami, A. (2019). A practical guide to sliding and surface semilandmarks in morphometric analyses. *Integrative Organismal Biology*, *1*(1). doi: 10.1093/iob/obz016

Bastir, M., Rosas, A., Stringer, C., Cuétara, J. M., Kruszynski, R., Weber, G. W., ... Ravosa, M. J. (2010). Effects of brain and facial size on basicranial form in human and primate evolution. *Journal of Human Evolution*, *58*(5), 424–431.

Bräuer, G. (1984). A craniological approach to the origin of anatomically modern homo sapiens in africa and implications for the appearance of modern europeans. In F. H. Smith & F. Spencer (Eds.), *The origins of modern humans: a world survey of the fossil evidence* (p. 327–410). Alan R. Liss.

Cheverud, J. M. (1982). Phenotypic, genetic, and environmental morphological integration in the cranium. *Evolution*, 499–516.

Cignoni, P., Callieri, M., Corsini, M., Dellepiane, M., Ganovelli, F., & Ranzuglia, G. (2008). MeshLab: an Open-Source Mesh Processing Tool. In V. Scarano, R. D. Chiara, & U. Erra (Eds.), *Eurographics italian chapter conference.* The Eurographics Association. doi: 10.2312/LocalChapterEvents/ItalChap/ItalianChapConf2008/129-136

Clarke, R. J. (1976). New cranium of homo erectus from lake ndutu, tanzania. *Nature*, *262*(5568), 485–487.

Clarke, R. J. (1990). The ndutu cranium and the origin of homo sapiens. *Journal of human evolution*, *19*(6-7), 699–736.

Conde, C. J. C., & Ayala, F. J. (2014). *Evolución humana*. Alianza Editorial.

Daboul, A., Ivanovska, T., Bülow, R., Biffar, R., & Cardini, A. (2018). Procrustes-based geometric morphometrics on mri images: An example of inter-operator bias in 3d landmarks and its impact on big datasets. *PloS one*, *13*(5), e0197675.

Demuro, M., Arnold, L. J., Aranburu, A., Sala, N., & Arsuaga, J.-L. (2019). New bracketing luminescence ages constrain the sima de los huesos hominin fossils (atapuerca, spain) to mis 12. *Journal of Human Evolution*, *131*, 76–95.

Di Vincenzo, F., Profico, A., Bernardini, F., Cerroni, V., Dreossi, D., Schlager, S., … others (2017). Digital reconstruction of the ceprano calvarium (italy), and implications for its interpretation. *Scientific reports*, *7*(1), 1–11.

Eslami, D., Di Angelo, L., Di Stefano, P., & Pane, C. (2020). Review of computer-based methods for archaeological ceramic sherds reconstruction. *Virtual Archaeology Review*, *11*(23), 34. doi: 10.4995/var.2020.13134

Feys, J. (2016). Nonparametric tests for the interaction in two-way factorial designs using r. *The R Journal*, *8*(1), 367–378.

Fruciano, C. (2016). Measurement error in geometric morphometrics. *Development Genes and Evolution*, *226*(3), 139–158. doi: 10.1007/s00427-016-0537-4

Gelfand, N., & Guibas, L. (2004). Shape segmentation using local slippage analysis. In *Sgp '04*.

Godinho, R. M., O'Higgins, P., & Gonçalves, C. (2020). Assessing the reliability of virtual reconstruction of mandibles. *American Journal of Physical Anthropology*, *172*(4), 723–734. doi: 10.1002/ajpa.24095

González-José, R., Escapa, I., Neves, W. A., Cúneo, R., & Pucciarelli, H. M. (2008). Cladistic analysis of continuous modularized traits provides phylogenetic signals in homo evolution. *Nature*, *453*(7196), 775–778.

Goodall, C. (1991). Procrustes methods in the statistical analysis of shape. *Journal of the Royal Statistical Society: Series B (Methodological)*, *53*(2), 285–321.

Grabowski, M., Hatala, K. G., Jungers, W. L., & Richmond, B. G. (2015). Body mass estimates of hominin fossils and the evolution of human body size. *Journal of Human Evolution*, *85*, 75–93. doi: 10.1016/j.jhevol.2015.05.005

Gunz, P., Mitteroecker, P., Neubauer, S., Weber, G. W., & Bookstein, F. L. (2009). Principles for the virtual reconstruction of hominin crania. *Journal of Human Evolution*, *57*(1), 48-62. Retrieved from https://www.sciencedirect.com/science/article/pii/S004724840900058X doi: https://doi.org/10.1016/j.jhevol.2009.04.004

Hawks, J., Elliott, M., Schmid, P., Churchill, S. E., Ruiter, D. J. D., Roberts, E. M., … et al. (2017). New fossil remains of homo naledi from the lesedi chamber, south africa. *eLife*, *6*. doi: 10.7554/elife.24232

Heckert, N. A., Filliben, J. J., Croarkin, C. M., Hembree, B., Guthrie, W. F., Tobias, P., ... others (2002). Handbook 151: Nist/sematech e-handbook of statistical methods.

Hornik, K. (2020). *R FAQ*. Retrieved from https://CRAN.R-project.org/doc/FAQ/R-FAQ.html

Hublin, J.-J. (2002). Northwestern african middle pleistocene hominids and their bearing on the emergence of homo sapiens. *Human roots, Africa and Asia in the middle Pleistocene*, 99–121.

Hublin, J.-J., Ben-Ncer, A., Bailey, S. E., Freidline, S. E., Neubauer, S., Skinner, M. M., ... et al. (2017). New fossils from jebel irhoud, morocco and the pan-african origin of homo sapiens. *Nature*, *546*(7657), 289–292. Retrieved from https://dx.doi.org/10.1038/nature22336 doi: 10.1038/nature22336

Kassambara, A. (2019, Nov). *Anova in r: The ultimate guide.* Retrieved from https://www.datanovia.com/en/lessons/anova-in-r/

Kassambara, A. (2021). rstatix: Pipe-friendly framework for basic statistical tests [Computer software manual]. Retrieved from https://CRAN.R-project.org/package=rstatix (R package version 0.7.0)

Klein, R. G. (2009). *The human career: Human biological and cultural origins*. University of Chicago Press.

Klingenberg, C. P. (2011). Morphoj: an integrated software package for geometric morphometrics. *Molecular ecology resources*, *11*(2), 353–357.

Kotoula, E. (2016). Semiautomatic fragments matching and virtual reconstruction: a case study on ceramics..

Lautenschlager, S. (2016). Reconstructing the past: methods and techniques for the digital restoration of fossils. *Royal Society Open Science*, *3*(10), 160342. Retrieved from https://dx.doi.org/10.1098/rsos.160342 doi: 10.1098/rsos.160342

Lenth, R. V. (2016). Least-squares means: the r package lsmeans. *Journal of statistical software*, *69*(1), 1–33.

Lenth, R. V. (2021). emmeans: Estimated marginal means, aka least-squares means [Computer software manual]. Retrieved from https://CRAN.R-project.org/package=emmeans (R package version 1.6.3)

Lieberman, D. E. (2011). 16. epigenetic integration, complexity, and evolvability of the head: Rethinking the functional matrix hypothesis. In *Epigenetics* (pp. 271–289). University of California Press.

Madrigal, L. (2012). *Statistics for anthropology*. Cambridge University Press.

Mah, K., & Caldwell, C. B. (2008). chapter 4 - biological target volume. In A. C. Paulino & B. S. Teh (Eds.), *Pet-ct in radiotherapy treatment planning* (p. 52-89). Philadelphia: Elsevier. Retrieved from https://www.sciencedirect.com/science/article/pii/B9781416032243500074 doi: https://doi.org/10.1016/B978-1-4160-3224-3.50007-4

Manega, P. C. (1993). *Geochronology, geochemistry and isotopic study of the plio-pleistocene hominid sites and the ngorongoro volcanic highland in northern tanzania* (Unpublished doctoral dissertation). University of Colorado at Boulder.

Martin, R., & Saller, K. (1957). Lehrbuch der anthropologie iii. *Stuttgart: Gustav Fischer*.

Materialise NV. (2017). *Mimics medical (software).*

McNulty, K. P. (2005). A geometric morphometric assessment of the hominoid supraorbital region: affinities of the eurasian miocene hominoids dryopithecus, graecopithecus,

and sivapithecus. In *Modern morphometrics in physical anthropology* (pp. 349–373). Springer.

Mitteroecker, P., & Huttegger, S. M. (2009). The concept of morphospaces in evolutionary and developmental biology: mathematics and metaphors. *Biological Theory*, *4*(1), 54–67.

Mturi, A. (1976). New hominid from lake ndutu, tanzania. *Nature*, *262*(5568), 484–485.

Müller, G. B. (2007). Evo–devo: extending the evolutionary synthesis. *Nature reviews genetics*, *8*(12), 943–949.

Murdoch, D., & Adler, D. (2021). *rgl: 3d visualization using opengl.* Retrieved from `https://CRAN.R-project.org/package = rgl` (R package version 0.106.8)

Neeser, R., Ackermann, R. R., & Gain, J. (2009). Comparing the accuracy and precision of three techniques used for estimating missing landmarks when reconstructing fossil hominin crania. *American Journal of Physical Anthropology*, *140*(1), 1–18. doi: 10.1002/ajpa.21023

Nie, X. (2005). Cranial base in craniofacial development: Developmental features, influence on facial growth, anomaly, and molecular basis. *Acta Odontologica Scandinavica*, *63*(3), 127–135. doi: 10.1080/00016350510019847

Palmas, G., Pietroni, N., Cignoni, P., & Scopigno, R. (2013). A computer-assisted constraint-based system for assembling fragmented objects.. doi: 10.1109/digitalheritage.2013.6743793

Papaioannou, G., Schreck, T., Andreadis, A., Mavridis, P., Gregor, R., Sipiran, I., & Vardis, K. (2017). From reassembly to object completion. *Journal on Computing and Cultural Heritage*, *10*(2), 1–22. doi: 10.1145/3009905

Plavcan, J. M. (2001). Sexual dimorphism in primate evolution. *American Journal of Physical Anthropology*, *116*(S33), 25–53. doi: 10.1002/ajpa.10011

Profico, A., Buzi, C., Davis, C., Melchionna, M., Veneziano, A., Raia, P., & Manzi, G. (2019). A new tool for digital alignment in virtual anthropology. *The Anatomical Record*, *302*(7), 1104–1115. Retrieved from `https://dx.doi.org/10.1002/ar.24077` doi: 10.1002/ar.24077

Profico, A., Schlager, S., Valoriani, V., Buzi, C., Melchionna, M., Veneziano, A., ... Manzi, G. (2018). Reproducing the internal and external anatomy of fossil bones: Two new automatic digital tools. *American Journal of Physical Anthropology*, *166*(4), 979-986. Retrieved from `https://onlinelibrary.wiley.com/doi/abs/10.1002/ajpa.23493` doi: https://doi.org/10.1002/ajpa.23493

R Core Team. (2020). *R: A language and environment for statistical computing.* R Foundation for Statistical Computing. Retrieved from `https://www.R-project.org/`

Raynal, J. P., Mohib, A., & Lefèvre, D. (2016). *Casablanca des origines.* Ministère de la Culture.

Raynal, J.-P., Sbihi-Alaoui, F.-Z., Mohib, A., El Graoui, M., Lefèvre, D., Texier, J.-P., ... others (2010). Hominid cave at thomas quarry i (casablanca, morocco): recent findings and their context. *Quaternary International*, *223*, 369–382.

Reno, P. L., Meindl, R. S., McCollum, M. A., & Lovejoy, C. O. (2003). Sexual dimorphism in australopithecus afarensis was similar to that of modern humans. *Proceedings of the National Academy of Sciences*, *100*(16), 9404–9409.

Rightmire, G. P. (1983). The lake ndutu cranium and early homo sapiens in africa. *American Journal of Physical Anthropology*, *61*(2), 245–254.

Rightmire, G. P. (2008). Homo in the middle pleistocene: hypodigms, variation, and species

recognition. *Evolutionary Anthropology: Issues, News, and Reviews: Issues, News, and Reviews*, *17*(1), 8–21.

Rightmire, G. P. (2017). Middle pleistocene homo crania from broken hill and petralona: morphology, metric comparisons, and evolutionary relationships. In *Human paleontology and prehistory* (pp. 145–159). Springer.

Rightmire, P. G. (1996). The human cranium from bodo, ethiopia: evidence for speciation in the middle pleistocene? *Journal of Human Evolution*, *31*(1), 21–39.

Sardi, M. L., Ventrice, F., & Ramírez Rozzi, F. (2007). Allometries throughout the late prenatal and early postnatal human craniofacial ontogeny. *The Anatomical Record*, *290*(9), 1112–1120. doi: 10.1002/ar.20581

Scerri, E. M., Thomas, M. G., Manica, A., Gunz, P., Stock, J. T., Stringer, C., ... others (2018). Did our species evolve in subdivided populations across africa, and why does it matter? *Trends in ecology & evolution*, *33*(8), 582–594.

Schlager, S. (2017). Morpho and rvcg – shape analysis in R. In G. Zheng, S. Li, & G. Szekely (Eds.), *Statistical shape and deformation analysis* (pp. 217–256). Academic Press.

Schwartz, J. H., & Tattersall, I. (2005). *The human fossil record, craniodental morphology of genus homo (africa and asia)* (Vol. 2). John Wiley & Sons.

Skelton, R. R., & McHenry, H. M. (1992). Evolutionary relationships among early hominids. *Journal of human evolution*, *23*(4), 309–349.

Smith, H. F., Ritzman, T., Otárola-Castillo, E., & Terhune, C. E. (2013). A 3-d geometric morphometric study of intraspecific variation in the ontogeny of the temporal bone in modern homo sapiens. *Journal of human evolution*, *65*(5), 479–489.

Stelzer, S., Neubauer, S., Hublin, J.-J., Spoor, F., & Gunz, P. (2019). Morphological trends in arcade shape and size in middle pleistocene homo. *American journal of physical anthropology*, *168*(1), 70–91.

Stringer, C. (2016). The origin and evolution of homo sapiens. *Philosophical Transactions of the Royal Society B: Biological Sciences*, *371*(1698), 20150237.

Suzuki, H., & Takai, F. (1970). The amud man and his cave site.

Weber, G. W., Seidler, H., Magori, C., Saanane, C., Kamamba, D., Thackeray, F., ... Conroy, G. C. (2005). *Ndutu, cd-rom including data from ct-scans.* Department of Evolutionary Anthropology, University of Vienna - Austria, Department of Antiquities, Dar-es-Salaam - Tanzania.

Wei, L., Yu, W., Li, M., & Li, X. (2011). Skull assembly and completion using template-based surface matching.. doi: 10.1109/3dimpvt.2011.59

White, T. D., Black, M. T., & Folkens, P. A. (2012). *Human osteology*. Academic press.

Wickham, H. (2011). The split-apply-combine strategy for data analysis. *Journal of Statistical Software*, *40*(1), 1–29. Retrieved from `http://www.jstatsoft.org/v40/i01/`

Wickham, H., Averick, M., Bryan, J., Chang, W., McGowan, L. D., François, R., ... Yutani, H. (2019). Welcome to the tidyverse. *Journal of Open Source Software*, *4*(43), 1686. doi: 10.21105/joss.01686

Wickham, H., Hester, J., & Francois, R. (2017). *readr: Read rectangular text data.* Retrieved from `https://CRAN.R-project.org/package = readr` (R package version 1.1.1)

Wolpoff, M. H. (1980). Cranial remains of middle pleistocene european hominids. *Journal of Human Evolution*, *9*(5), 339-358. Retrieved from `https://www.sciencedirect.com/science/article/pii/0047248480900470` doi: https://doi.org/10.1016/0047-2484(80)90047-0

Wood, B., & Lonergan, N. (2008). The hominin fossil record: taxa, grades and clades. *Journal of Anatomy*, *212*(4), 354–376.

Zelditch, M., Swiderski, D., Sheets, H. D., & Fink, W. (2004). *Geometric morphometrics for biologists: A primer*. doi: 10.1016/B978-012778460-1/50003-X

Zollikofer, C. P. (2012). Evolution of hominin cranial ontogeny. *Progress in brain research*, *195*, 273–292.

Appendix A

Fragment Reassembler Constrain Band Tables

Constraint band	Connected fragments	Residual energy
0	Fragment: 06.ply to Fragment: 08.ply.	89.79%
1	Fragment: 09.ply to Fragment: 08.ply.	0.80%
2	Fragment: 06.ply to Fragment: 08.ply.	45.36%
3	Fragment: 06.ply to Fragment: 08.ply.	46.71%
5	Fragment: 07.ply to Fragment: 08.ply.	61.12%
6	Fragment: 06.ply to Fragment: 08.ply.	91.83%
7	Fragment: 07.ply to Fragment: 08.ply.	35.85%
8	Fragment: 07.ply to Fragment: 08.ply.	80.84%
9	Fragment: 07.ply to Fragment: 08.ply.	44.32%
10	Fragment: 07.ply to Fragment: 08.ply.	96.70%
11	Fragment: 06.ply to Fragment: 07.ply.	33.02%
12	Fragment: 07.ply to Fragment: 08.ply.	44.15%
14	Fragment: 07.ply to Fragment: 08.ply.	91.40%
15	Fragment: 06.ply to Fragment: 07.ply.	71.10%
16	Fragment: 06.ply to Fragment: 08.ply.	40.01%
17	Fragment: 06.ply to Fragment: 08.ply.	62.96%
18	Fragment: 06.ply to Fragment: 08.ply.	84.27%
19	Fragment: 05.ply to Fragment: 07.ply.	48.00%
20	Fragment: 06.ply to Fragment: 07.ply.	40.56%
21	Fragment: 09.ply to Fragment: 08.ply.	14.45%
22	Fragment: 09.ply to Fragment: 08.ply.	58.40%
23	Fragment: 09.ply to Fragment: 08.ply.	52.16%
24	Fragment: 09.ply to Fragment: 08.ply.	68.77%
25	Fragment: 09.ply to Fragment: 05.ply.	47.48%
26	Fragment: 05.ply to Fragment: 06.ply.	13.49%
27	Fragment: 05.ply to Fragment: 08.ply.	82.38%
28	Fragment: 05.ply to Fragment: 08.ply.	66.27%
29	Fragment: 09.ply to Fragment: 05.ply.	46.95%
30	Fragment: 05.ply to Fragment: 06.ply.	51.78%
31	Fragment: 09.ply to Fragment: 05.ply.	57.20%
32	Fragment: 05.ply to Fragment: 08.ply.	62.45%

33	Fragment: 05.ply to Fragment: 08.ply.	58.38%
34	Fragment: 05.ply to Fragment: 08.ply.	81.64%
35	Fragment: 09.ply to Fragment: 05.ply.	46.58%
36	Fragment: 10.ply to Fragment: 08.ply.	85.87%
37	Fragment: 10.ply to Fragment: 08.ply.	74.43%
38	Fragment: 10.ply to Fragment: 08.ply.	67.45%
39	Fragment: 10.ply to Fragment: 08.ply.	31.84%
40	Fragment: 05.ply to Fragment: 04.ply.	57.08%
41	Fragment: 08.ply to Fragment: 04.ply.	0.13%
42	Fragment: 08.ply to Fragment: 04.ply.	0.60%
43	Fragment: 10.ply to Fragment: 08.ply.	10.78%
44	Fragment: 08.ply to Fragment: 04.ply.	0.93%
45	Fragment: 05.ply to Fragment: 04.ply.	3.75%
46	Fragment: 08.ply to Fragment: 04.ply.	92.21%
47	Fragment: 08.ply to Fragment: 04.ply.	33.40%
48	Fragment: 03.ply to Fragment: 05.ply.	2.88%
49	Fragment: 08.ply to Fragment: 04.ply.	5.98%
50	Fragment: 05.ply to Fragment: 08.ply.	59.74%
51	Fragment: 05.ply to Fragment: 04.ply.	52.16%
52	Fragment: 05.ply to Fragment: 04.ply.	79.35%
53	Fragment: 05.ply to Fragment: 04.ply.	59.06%
54	Fragment: 03.ply to Fragment: 05.ply.	1.67%
55	Fragment: 09.ply to Fragment: 03.ply.	6.49%
56	Fragment: 09.ply to Fragment: 03.ply.	61.52%
57	Fragment: 03.ply to Fragment: 05.ply.	38.24%
58	Fragment: 03.ply to Fragment: 05.ply.	70.65%

Table A.1: Constrain bands connecting the fragments of the Ndutu cranial vault and base.

Constraint band	Connected fragments	Residual energy
1	Fragment: 09.ply to Fragment: 08.ply.	0.23%
2	Fragment: 06.ply to Fragment: 08.ply.	39.97%
3	Fragment: 06.ply to Fragment: 08.ply.	50.90%
4	Fragment: 01-4.ply to Fragment: 09.ply.	64.58%
5	Fragment: 07.ply to Fragment: 08.ply.	66.21%
6	Fragment: 06.ply to Fragment: 08.ply.	86.39%
7	Fragment: 07.ply to Fragment: 08.ply.	37.09%
8	Fragment: 07.ply to Fragment: 08.ply.	79.67%
9	Fragment: 07.ply to Fragment: 08.ply.	49.22%
10	Fragment: 01-4.ply to Fragment: 08.ply.	94.29%
11	Fragment: 06.ply to Fragment: 07.ply.	32.00%
12	Fragment: 07.ply to Fragment: 08.ply.	66.08%
13	Fragment: 01-4.ply to Fragment: 08.ply.	24.84%
14	Fragment: 07.ply to Fragment: 08.ply.	86.85%

15	Fragment: 06.ply to Fragment: 07.ply.	71.10%
16	Fragment: 06.ply to Fragment: 08.ply.	38.40%
17	Fragment: 06.ply to Fragment: 08.ply.	70.11%
18	Fragment: 06.ply to Fragment: 08.ply.	82.14%
19	Fragment: 05.ply to Fragment: 07.ply.	49.22%
20	Fragment: 06.ply to Fragment: 07.ply.	44.62%
21	Fragment: 09.ply to Fragment: 08.ply.	18.98%
22	Fragment: 09.ply to Fragment: 08.ply.	54.27%
23	Fragment: 09.ply to Fragment: 08.ply.	50.41%
24	Fragment: 09.ply to Fragment: 08.ply.	80.46%
25	Fragment: 09.ply to Fragment: 05.ply.	65.22%
26	Fragment: 05.ply to Fragment: 06.ply.	9.59%
27	Fragment: 01-4.ply to Fragment: 09.ply.	60.02%
28	Fragment: 05.ply to Fragment: 08.ply.	70.15%
29	Fragment: 09.ply to Fragment: 05.ply.	52.60%
30	Fragment: 05.ply to Fragment: 06.ply.	61.11%
31	Fragment: 09.ply to Fragment: 05.ply.	48.80%
32	Fragment: 05.ply to Fragment: 08.ply.	74.27%
33	Fragment: 05.ply to Fragment: 08.ply.	80.23%
34	Fragment: 05.ply to Fragment: 08.ply.	74.05%
35	Fragment: 09.ply to Fragment: 05.ply.	47.93%
36	Fragment: 10.ply to Fragment: 08.ply.	85.96%
37	Fragment: 10.ply to Fragment: 08.ply.	74.46%
38	Fragment: 10.ply to Fragment: 08.ply.	67.50%
39	Fragment: 10.ply to Fragment: 08.ply.	31.84%
40	Fragment: 01-4.ply to Fragment: 08.ply.	38.82%
41	Fragment: 01-4.ply to Fragment: 08.ply.	79.70%
42	Fragment: 05.ply to Fragment: 01-4.ply.	107.87%
43	Fragment: 10.ply to Fragment: 08.ply.	10.78%
44	Fragment: 01-4.ply to Fragment: 09.ply.	83.12%
45	Fragment: 05.ply to Fragment: 01-4.ply.	85.99%
46	Fragment: 05.ply to Fragment: 01-4.ply.	50.24%
47	Fragment: 01-4.ply to Fragment: 08.ply.	100.02%
48	Fragment: 05.ply to Fragment: 01-4.ply.	86.76%
49	Fragment: 01-4.ply to Fragment: 08.ply.	79.09%
50	Fragment: 05.ply to Fragment: 08.ply.	78.82%
51	Fragment: 05.ply to Fragment: 01-4.ply.	100.00%
52	Fragment: 05.ply to Fragment: 01-4.ply.	78.40%
54	Fragment: 01-4.ply to Fragment: 08.ply.	100.93%

Table A.2: Constrain bands connecting the fragments of the Clarke's 1990 reconstruction of the Ndutu cranium.

Appendix B

Blue.R

```
#Start script
print("Initiating script.")
##Load packages
library(Morpho)
library(plyr)
library(readr)
library(geomorph)
library(Arothron)
library(compositions)
library(rgl)
library(Evomorph)
#Create special functions
##"Function to read and write Meshlab picked points (*.pp) with R" (Griffin,
    2017)
    <http://www.randigriffin.com/2017/05/07/read-meshlab-pickedpoints.html>
####Watch out! Do not edit this!
write.pp <- function (mat, file) {
  # create text for each point
  pp <- c()
  for (i in 1:nrow(mat)) {
    point <- paste0(" <point x=\"", mat[i,1],
                    "\" y=\"", mat[i,2],
                    "\" z=\"", mat[i,3],
                    "\" name=\"p", i,
                    "\" active=\"1\"/>")
    pp <- append(pp, point)
  }
  # add supporting markup
  pp <- c("<!DOCTYPE PickedPoints>",
          "<PickedPoints>",
          "  <DocumentData>",
          paste0("   <DataFileName name=\"", tail(strsplit(file,"/")[[1]],1),
              "\"/>"),
          "    <templateName name=\"template.pptpl\"/>",
          "  </DocumentData>",
          pp,
```

```
        "</PickedPoints>")
  # write the file
  write(pp, file=file)
}
####Be careful with this!

#Load data
print("Please locate the desired working directory.")
print("Note that it is absolutely neccessary that the chosen directory
    contains two folders, one called 'Target' and another one called
    'Reference'.")
print("- The 'Target' folder is where the fragmentary specimen's landmark data
    is stored. There must be at least one MeshLab *.pp file per fragment.")
print("- The 'Reference' folder is where the reference sample landmark data is
    stored. It is recommended that the name each file includes the recorded
    specimen's ID.")
print("Within the 'Reference' folder, you should prepare another directory
    called 'Results'.")
setwd(choose.dir(default =
    "C:/Users/Gustavo/OneDrive/Documents/MA/Thesis/Data", caption = "Select
    folder"))
itmeas <- readline(prompt = "Does the selected directory contain repeated
    measurement data? Type 'y' or 'n'.")
if (itmeas == "y"){
  print("Specimen naming will depend on the *.PP file name.")
  print("Please note that it is assumed that iterated measurements are
      numbered and that this number matches the first character(s) in the file
      name.")
  separator <- readline(prompt = "Please enter the character separating the
      number from the specimen name (for example, '-').")
  itmeas.no <- as.numeric(readline("How many times have the specimens been
      measured?"))
  itmeas.no <- c(1:itmeas.no)
  itmeas.choice <- length(itmeas.no) #as.numeric(readline(prompt = "Type the
      number of measurement that you wish to use to create the data frames."))
  print("Using last measurement to create the data frames.")
}
###Set working directory to target specimen directory.
setwd("./Target")
print("Importing target specimen data.")
###Create file list.
if (itmeas == "y"){
  targetfiles = list.files(pattern = paste0(itmeas.choice, separator))
  tvalidation = list.files(pattern = "*.pp")
} else {
  targetfiles = list.files(pattern = "*.pp")
}
###Load files in list to data frame.
target.data <- lapply(targetfiles, read.mpp)
if (itmeas == "y"){
```

```
  target.valid <- lapply(tvalidation, read.mpp)
}
###Delete file extension from list of files
if (itmeas == "y") {
  targetfiles <- gsub(paste0(itmeas.choice, separator), "", targetfiles)
  for (i in 1:length(itmeas.no)){
    tvalidation <- gsub(paste0(i, separator), "", tvalidation)
  }
  tvalidation <- gsub(".pp", "", tvalidation)
}
targetfiles <- gsub(".pp", "", targetfiles)
###Take each name in the list and use it to rename each matrix in the data
    frame accordingly
names(target.data) <- c(targetfiles)
names(target.valid) <- c(tvalidation)
###Replace "0.000..." values with "NA".
for (n in 1:length(target.data)){
  for (k in 1:length(target.data[[n]])){
    if (target.data[[n]][k] == 0){
      target.data[[n]][k] <- NA
    }
  }
}
if (itmeas == "y"){
  for (n in 1:length(target.valid)){
    for (k in 1:length(target.valid[[n]])){
      if (target.valid[[n]][k] == 0){
        target.valid[[n]][k] <- NA
      }
    }
  }
}
print("Done.")
###Change working directory to reference data set directory.
setwd('..')
setwd("./Reference")
print("Importing sample data.")
###Create file list.
if (itmeas == "y"){
  myfiles = list.files(pattern = paste0(itmeas.choice, separator))
  svalidation = list.files(pattern = "*.pp")
} else {
  myfiles = list.files(pattern = "*.pp")
}
###Load files in list to data frame.
sample.data <- lapply(myfiles, read.mpp)
if (itmeas == "y"){
  sample.valid <- lapply(svalidation, read.mpp)
}
###Delete file extension from list of files
```

```
if (itmeas == "y") {
  myfiles <- gsub(paste0(itmeas.choice, separator), "", myfiles)
  for (i in 1:length(itmeas.no)){
    svalidation <- gsub(paste0(i, separator), "", svalidation)
  }
  svalidation <- gsub(".pp", "", svalidation)
}
myfiles <- gsub(".pp", "", myfiles)
###Take the name of each file in the list and use it to rename each matrix in
    the data frame accordingly
names(sample.data) <- c(myfiles)
names(sample.valid) <- c(svalidation)
###Rename columns.
for (n in 1:length(sample.data)){
  colnames(sample.data[[n]]) <- c("x","y","z")
}
###Save landmark names.
varname <- list(row.names(sample.data[[1]]))
###Replace "0.000..." values with "NA".
for (n in 1:length(sample.data)){
  for (k in 1:length(sample.data[[n]])){
    if (sample.data[[n]][k] == 0){
      sample.data[[n]][k] <- NA
    }
  }
}
if (itmeas == "y"){
  for (n in 1:length(sample.valid)){
    for (k in 1:length(sample.valid[[n]])){
      if (sample.valid[[n]][k] == 0){
        sample.valid[[n]][k] <- NA
      }
    }
  }
}
print("Done.")
for (n in 1:length(sample.data)){
  for (k in 1:length(sample.data[[length(sample.data)]][,1])){
    if(is.na(sample.data[[n]][k]) == TRUE){
      miss = 1
    }
  }
}
if(miss == 1){
  ###Create empty list.
  nafreq <- matrix(ncol = 1, nrow = 0)
  ###Count how many times a landmark is missing in sample.
  for (k in 1:length(sample.data[[length(sample.data)]][,1])){
    #Create/revert missing landmark frequency counter.
    count2 = 0
```

```
    for (n in 1:length(sample.data)){
      if(is.na(sample.data[[n]][k]) == TRUE){
        count2 <- count2 + 1
      }
    }
    print(paste0("Warning: Landmark ",
        row.names(sample.data[[length(sample.data)]])[k], " (No. ", k, ") is
        missing from ", count2, " specimens."))
    #Put missing landmark frequency in list.
    nafreq[k] <- count2
  }
}
print("Applying format to data...")
sample <- array(c(NA), dim = c(length(sample.data[[1]][,1]),
    length(sample.data[[1]][1,]), length(sample.data)))
for (n in 1:length(sample.data)){
  for (k in 1:length(sample.data[[n]][,1])){
    for(m in 1:length(sample.data[[n]][k,])){
      sample[,,n][k,m] <- sample.data[[n]][k,m]
    }
  }
}
target <- array(c(NA), dim = c(length(target.data[[1]][,1]),
    length(target.data[[1]][1,]), length(target.data)))
for (n in 1:length(target.data)){
  for (k in 1:length(target.data[[n]][,1])){
    for(m in 1:length(target.data[[n]][k,])){
      target[,,n][k,m] <- target.data[[n]][k,m]
    }
  }
}
print("Done.")

#Estimate missing landmarks
if (miss == 1){
  print("Several landmarks are missing and must be estimated to continue.")
  estimation.method <- 1 #readline(prompt = "Please select an estimation
      method. Type '1' for TPS or '2' for regression.")
  estimate.sample.valid <- array(c(NA), dim = c(length(sample.valid[[1]][,1]),
      length(sample.valid[[1]][1,]), length(sample.valid)))
  if (itmeas == "y")
    for (n in 1:length(sample.valid)){
      for (k in 1:length(sample.valid[[n]][,1])){
        for(m in 1:length(sample.valid[[n]][k,])){
          estimate.sample.valid[,,n][k,m] <- sample.valid[[n]][k,m]
        }
      }
    }
  if (estimation.method == 1){
    sample <- estimate.missing(sample, method = "TPS")
```

```
    if (itmeas == "y"){
      estimate.sample.valid <- estimate.missing(estimate.sample.valid, method =
          "TPS")
    }
    print("Using TPS method.")
  } else {
    sample <- estimate.missing(sample, method = "Reg")
    if (itmeas == "y"){
      estimate.sample.valid <- estimate.missing(estimate.sample.valid, method =
          "Reg")
    }
    print("Using regression method.")
  }
  print("Done.")
}

#Assessment of intraobserver bias
replicability <- readline(prompt = "Do you wish to assess measurement bias?
    Type 'y' or 'n'.")
if (replicability == "y"){
  print("Assessment of reproductibility is not available in this script yet.")
  print("This will create *.TPS and *.TXT files containing data that can be
      used in another software to compute a Procrustes ANOVA.") #######MAKE IT
      SO!
  valid.list <- NULL
  for (i in 1:length(target.data)){
    sink(paste0(i, "_validation.TPS"))
    for (n in 1:length(sample.valid)){
      cat(paste0("LM3=", length(which(complete.cases(target.valid[[i]])))))
      cat("\n")
      cat(write.table(estimate.sample.valid[,,n][(which(complete.cases(target.valid[[i]]))),]
          row.names=F, col.names=F, sep="\t"))
      cat(paste0("ID=", names(sample.valid[n])))
      cat("\n")
      cat("\n")
    }
    for (j in 0:(length(itmeas.no)-1)){
      cat(paste0("LM3=", length(which(complete.cases(target.data[[i]])))))
      cat("\n")
      cat(write.table(target.valid[[i+(length(target.data)*j)]][(which(complete.cases(target
          row.names=F, col.names=F, sep="\t"))
      cat(paste0("ID=", names(target.valid[i])))
      cat("\n")
      cat("\n")
    }
    sink()
    valid.list <- append(valid.list, paste0("./", i, "_validation.TPS"))
  }
  ###Create ind table for MorphoJ
  ind.table <- append("ID", names(sample.data))
```

```
ind.table <- append(ind.table, names(target.data))
jclassifiers <- append("ind", append(c(1:(length(sample.data))),
    rep(length(sample.data)+1, length(target.data))))
ind.table <- cbind(ind.table, jclassifiers)
write.table(ind.table, file = "validclass.txt", quote = FALSE, sep = "\t",
    row.names = FALSE, col.names = FALSE) #Write ind table to .TXT
print("Done. Files are stored in the Reference directory.")
R.save <- NULL
for (i in 1:length(target.data)){
  MS.among <- as.numeric(readline(prompt = "Provide the among-groups ANOVA
      sum of squares."))
  MS.within <- as.numeric(readline(prompt = "Provide the within-groups ANOVA
      sum of squares."))
  S2.among = (MS.among - MS.within)/(length(itmeas.no))
  R = S2.among/(MS.within + S2.among) #From Fleiss, 1977; Sokal and Rohlf,
      1995; Arnqvist and Mrtensson, 1988
  R.save <- append(R.save, R)
  print(paste0("Intra-class correlation coefficient (R) (Fruciano, 2016) =
      ", R))
  Rn = (length(itmeas.no)*R)/(1+((length(itmeas.no)-1)*R))
  print(paste0("Averaged repeatability value (Rn) (Fleiss, 1977; Arnqvist
      and Mrtensson, 1998) = ", Rn))
}
spec.names <- append(names(sample.data), "Ndutu")
print("Computing absolute measurement error.")
for (i in 1:length(valid.list)){
  itmeas.mn <- NULL
  mn.error <- NULL
  error.sample <- lapply(valid.list[i], readland.tps)
  error.sample <- error.sample[[1]] #Incorrect number of dimensions
      workaround.
  spec.meas <- array(dim = c(length(error.sample[,,1][,1]),
      length(error.sample[,,1][1,]), length(itmeas.no)))
  specs <- array(dim = c(length(itmeas.no), 1, length(spec.names)))
  for (j in 1:length(sample.data)){
    for (k in 0:(length(itmeas.no)-1)){
      spec.meas[,,(k+1)] <- error.sample[,,((length(sample.data)*k)+j)]
    }
    spec.msh <- mshape(spec.meas)
    for (k in 1:length(itmeas.no)){
      mn.error <- NULL
      meas.error <- NULL
      for (l in 1:length(spec.meas[,,k][,1])){
        lmdist = sqrt(((spec.msh[l,1] - spec.meas[,,k][l,1])^2) +
            ((spec.msh[l,2] - spec.meas[,,k][l,2])^2) + ((spec.msh[l,3] -
            spec.meas[,,k][l,3])^2))
        meas.error <- append(meas.error, lmdist)
      }
      mn.error <- append(mn.error, mean(meas.error))
      specs[,,j][k] <- mn.error
```

```
    }
  }
  for (k in 1:length(itmeas.no)){
    spec.meas[,,k] <- error.sample[,,(length(sample.valid)+k)]
  }
  spec.msh <- mshape(spec.meas)
  for (k in 1:length(itmeas.no)){
    mn.error <- NULL
    meas.error <- NULL
    for (l in 1:length(spec.meas[,,k][,1])){
      lmdist = sqrt(((spec.msh[l,1] - spec.meas[,,k][l,1])^2) +
          ((spec.msh[l,2] - spec.meas[,,k][l,2])^2) + ((spec.msh[l,3] -
          spec.meas[,,k][l,3])^2))
      meas.error <- append(meas.error, lmdist)
    }
    mn.error <- append(mn.error, mean(meas.error))
    specs[,,length(spec.names)][k] <- mn.error
  }
  it.error <- NULL
  it.error <- cbind(it.error, c(rep(0,length(spec.names))))
  plot(it.error, ylim = c(0, 1.5), main = "Measurement Error", xlab =
      "Sample", ylab = "Mean landmark displacement (Euclidean distance)",
      type = "n", las = 2)
  for (k in 1:length(itmeas.no)){
    for (j in 1:length(spec.names)){
      it.error[j] <- specs[,,j][k]
    }
    lines(it.error)
    axis(1, at = 1:length(it.error), labels = spec.names, las = 2)
    itmeas.mn <- append(itmeas.mn, mean(it.error))
  }
  print(paste0("For fragment No.", i, ", the mean errors per measurement
      were:"))
  print(itmeas.mn)
 }
 print("Done.")
}

#DTA loop.
go <- readline(prompt = "Starting unarticulated fragment alignment procedure.
   Press [enter] to continue or [esc] to abort.")
complete <- NULL
is.complete <- NULL
use.complete <- "n"
is.complete <- list.files(path = "./Results", pattern = "*.pp", full.names =
   TRUE)
if (length(is.complete) > 0){
 use.complete <- readline(prompt = "A .PP file has been found in the Results
     directory. Do you wish to use this? Type 'y' or 'n'.")
 if (use.complete == "y") {
```

```
    ready <- readline(prompt = "Warning: Running this script for a second time
       will re-write several files. Salvage what you need. Press [enter] when
       ready.")
    complete <- read.mpp(is.complete[1], info = FALSE)
  }
}
##Load the disarticulated model files.
print("This process requires a 3D mesh file for each one of the disarticulated
    model (DM) fragments.")
if (is.null(complete) == FALSE){
  print("Warning: The AM landmark data set may no longer be mapped to the DM
      3D meshes. You will need to provide new 3D mesh files for each one of
      the DM fragments.")
  print("Create a new fragment set by disarticulating the AM in a 3D mesh
      processing software again. If there was a previous run, a .PP file would
      have been created to make it possible to verify that the fragment 3D
      meshes are mapped correctly.")
}
targetplys <- list.files(path = choose.dir(default =
    "E:/3D/PjtNARWHAL/Target", caption = "Choose the directory where the 3D
    meshes of the target specimen are stored."), pattern = "*.ply", full.names
    = TRUE)
target.meshes <- lapply(targetplys, file2mesh)
##Tell R in which order to assemble the fragments and what to use.
assembly.order = 1:length(target.data)
first <- as.numeric(readline(prompt = "Select a fragment to begin the
    alignment by typing in the corresponding number."))
assembly.order <- assembly.order[-first]
target_ordr <- array(dim = c(length(target.data[[1]][,1]),
    length(target.data[[1]][1,]), length(assembly.order)))
for (i in 1:length(assembly.order)){
  target_ordr[,,i] <- target[,,(assembly.order[i])]
}
a <- array(dim = c(length(target.data[[1]][,1]), length(target.data[[1]][1,]),
    1))
a <- target[,,first]
Amesh <- target.meshes[[first]]
Bmeshes <- target.meshes[-first]
for (i in 1:length(assembly.order)){
  Bmeshes[[i]] <- target.meshes[[(assembly.order[i])]]
}
##Create some empty vectors for later.
bestrms <- NULL
dtasamples <- NULL
aligned.meshes <- NULL
AMlms <- NULL
phase = 1
alsets <- NULL
Asurf <- NULL
sample.meshes <- NULL
```

```
semiland.use <- "n"
symm.patt <- NULL
###Loop start.
while (phase != length(target.data)){
  for (i in 1:length(assembly.order)){
    for (b in 1:length(assembly.order)){
      print("---")
      print(paste0("Aligning fragment no. ", b, " of ", length(assembly.order),
          " with the selected fragment (phase ", phase, ")."))
      #Define the landmarks belonging to the first and second model.
      if (phase == (length(target.data) -1)){
        bset <- which(complete.cases(target_ordr) == TRUE)
        if (is.null(complete) == FALSE){
          blms <- array(dim = c(length(complete[,1]), length(complete[1,]), 1))
          for (i in 1:length(blms[,,1][,1])){
            blms[,,1][i,] <- complete[i,]
          }
          blms <- blms[,,1]
        } else {
          blms <- target_ordr
        }
      } else {
        bset <- which(complete.cases(target_ordr[,,b]) == TRUE)
        if (is.null(complete) == FALSE){
          blms <- array(dim = c(length(complete[,1]), length(complete[1,]), 1))
          for (i in 1:length(blms[,,1][,1])){
            blms[,,1][i,] <- complete[i,]
          }
          blms <- blms[,,1]
        } else {
          blms <- target_ordr[,,b]
        }
      }
      if (phase == 1){
        alignset <- append(which(complete.cases(a) == TRUE), bset)
        mod_1 <- c(1:length(which(complete.cases(a) == TRUE)))
        mod_2 <- c((length(which(complete.cases(a) ==
            TRUE))+1):length(alignset))
      } else {
        alignset <- append(chosenAMset$x, bset)
        mod_1 <- c(1:length(chosenAMset$x))
        mod_2 <- c((length(chosenAMset$x)+1):length(alignset))
      }
      ##Create a new data subset for the DTA.
      ###Prepare target data set.
      if (phase == 1){
        if (is.null(complete) == FALSE){
          target_dta <- rbind(blms[which(complete.cases(a) == TRUE),],
              blms[bset,])
        } else {
```

```
    target_dta <- rbind(a[which(complete.cases(a) == TRUE),], blms[bset,])
  }
} else {
  target_dta <- rbind(a, blms[bset,])
}
sample_dta <- array(dim = c(length(alignset), length(sample[,,1][1,]),
    length(sample.data)))
for (n in 1:length(sample.data)){
  sample_dta[,,n] <- sample[,,n][alignset,]
}
##Symmetry module
pairs_1 = NULL #Set pair list default values to NULL.
pairs_2 = NULL
symmetrical.use <- readline(prompt = "Do you wish to consider symmetry in
    this alignment? Type 'y' or 'n'.")
if (symmetrical.use == "y"){
  print("Symmetry module active.")
  if (is.null(symm.patt)){
    symm.patt <- list(c(1, 2))
    symm.patt[[1]] <- readline(prompt = "Please enter the characters used
        to distinguish left bilateral landmarks. For example, '_L'.")
    symm.patt[[2]] <- readline(prompt = "Please enter the characters used
        to distinguish right bilateral landmarks. For example, '_R'.")
  }
  symmlmsL.names <- grep(paste0("*", symm.patt[[1]]), varname[[1]], value
      = TRUE) #Get the names of all the left bilateral landmarks that
      were retained in the sample set.
  symmlmsL.names <- gsub(symm.patt[[1]], "", symmlmsL.names) #Delete the
      "left" part of their names.
  symmlmsR = 0 #Create a new empty right bilateral landmark list.
  symmlmsR.names = 0
  for (i in 1:length(symmlmsL.names)){
    symmlmsR <- append(symmlmsR, grep(paste0(symmlmsL.names[i],
        symm.patt[[2]]), varname[[1]])) #Search which of the landmarks
        retained in the sample are the corresponding right bilateral
        landmarks for the left bilateral landmarks in the first list.
    symmlmsR.names <- append(symmlmsR.names,
        grep(paste0(symmlmsL.names[i], symm.patt[[2]]), varname[[1]],
        value = TRUE)) #Get their names.
  }
  symmlmsR.names <- gsub(symm.patt[[2]], "", symmlmsR.names) #Delete the
      "right" part of their names.
  symmlmsR <- symmlmsR[-1] #Get rid of the zeros.
  symmlmsR.names <- symmlmsR.names[-1]
  symmlmsR2L = 0
  symmlmsL.names <- grep(paste0("*", symm.patt[[1]]), varname[[1]], value
      = TRUE) #Put the "left" part of the names of the left bilateral
      landmarks back in the list.
  for (i in 1:length(symmlmsR.names)){
```

```
    symmlmsR2L <- append(symmlmsR2L, grep(symmlmsR.names[i],
        symmlmsL.names, value = TRUE)) #Keep only the left bilateral
        landmark names that have a corresponding right bilateral landmark
        in the second list.
  }
  symmlmsR2L <- symmlmsR2L[-1]
  symmlmsL = 0 #Create a new empty left bilateral landmark list.
  for (i in 1:length(symmlmsR2L)){
    symmlmsL <- append(symmlmsL, grep(paste0(symmlmsR2L[i]),
        varname[[1]]))
  }
  symmlmsL <- symmlmsL[-1]
  symmlms <- cbind(symmlmsL, symmlmsR)
  if ((length(symmlms) != 0) == TRUE){
    for (r in 1:length(symmlms[,1])){
      if (all(symmlms[r,] %in% mod_1) == TRUE){
        pairs_1 <- rbind(pairs_1, symmlms[r,])
      }
    }
    for (r in 1:length(symmlms[,1])){
      if (all(symmlms[r,] %in% mod_2) == TRUE){
        pairs_2 <- rbind(pairs_2, symmlms[r,])
      }
    }
  }
}
##Semilandmarks module.
if (use.complete == "y"){
  semiland.use <- readline(prompt = "Are you trying to correct a previous
      alignment by using surface semilandmarks? Type 'y' or 'n'.")
  if (semiland.use == "y"){
    print("Semilandmarks module active.")
    if (symmetrical.use == "y"){
      print("Warning: Symmetry constrains will not apply to surface
          semilandmarks.")
    }
    ###Load the sample mesh files. Pro tip: Name the 3D model files the
        same as their corresponding Meshlab picked points files.
    if (is.null(sample.meshes)){
      print("You will need to provide 3D mesh files for all of the sample
          specimens.")
      sampleplys <- list.files(path = choose.dir(caption = "Choose the
          directory where the surface 3D meshes of the sample specimens
          are stored."), pattern = "*.ply", full.names = TRUE)
      sample.meshes <- lapply(sampleplys, file2mesh)
    }
    ###Load a surface mesh.
    print("A surface mesh is required to apply semilandmarks. Please,
        prepare and locate the file corresponding to the surface mesh of
        the selected fragment or alignment.")
```

```
if (is.null(Asurf)){
  Asurf <- file2mesh(choose.files(caption = "Select a surface mesh."))
} else if (phase > 1) {
  print("Warning: The landmark data set may no longer be mapped to
      the surface mesh. Every time an alignment is accepted, a new
      surface mesh is required to apply semilandmarks.")
  print("A .PP file of the accepted alignment has been created to
      verify that the landmarks are correctly mapped to the chosen
      previous phase alignment mesh. Delete this file after use!")
  ###Write a .PP file to check if the AM_set is in the same atlas as
      the AM_mesh
  write.pp(target_dta, "./Results/accepted.pp")
  Asurf <- file2mesh(choose.files(caption = "Select a surface mesh."))
}
#print("Determining minimal amount of surface semilandmarks.")
watanabe = 100 ###ADD LASEC FUNCTION
print("Creating template.")
target.surf <- buildtemplate(spec = Asurf, fixed = target_dta, center
    = FALSE, surface.sliders = watanabe)
target.nts <- readland.nts("./Asurf.nts")
target.surf <- array(dim = c((length(alignset) + watanabe),
    length(sample.data[[1]][1,]), 1))
for (k in 1:(length(alignset) + watanabe)){
  target.surf[,,1][k,] <- target.nts[,,k]
}
###Divide the semilandmark set
target.surA <- target.surf[,,1][mod_1,]
target.surB <- target.surf[,,1][mod_2,]
target.surC <- target.surf[,,1][((length(alignset)
    +1):(length(alignset) + watanabe)),]
###Rearrange the landmarks
target.semi <- rbind(target.surA, target.surC)
target.semi <- rbind(target.semi, target.surB)
target_dta <- target.semi
sample.semi <- array(dim = c((length(alignset) + watanabe),
    length(sample.data[[1]][1,]), length(sample.data)))
print("Applying semilandmarks.")
for (n in 1:length(sample.data)){
  Bsurf <- sample.meshes[[n]]
  sample.surf <- digitsurface(spec = Bsurf, fixed = sample_dta[,,n],
      center = FALSE)
  sample.nts <- readland.nts("./Bsurf.nts")
  sample.surf <- array(dim = c((length(alignset) + watanabe),
      length(sample.data[[1]][1,]), 1))
  for (k in 1:(length(alignset) + watanabe)){
    sample.surf[,,1][k,] <- sample.nts[,,k]
  }
  sample.surA <- sample.surf[,,1][mod_1,]
  sample.surB <- sample.surf[,,1][mod_2,]
```

```
      sample.surC <- sample.surf[,,1][((length(alignset)
         +1):(length(alignset) + watanabe)),]
      sample.surD <- rbind(sample.surA, sample.surC)
      sample.surD <- rbind(sample.surD, sample.surB)
      sample.semi[,,n] <- sample.surD
    }
    sample_dta <- sample.semi
    aset <- mod_1 #Save original 'mod_1'.
    mod_1 <- c(1:(length(mod_1) + watanabe))
    mod_2 <- c((length(mod_1)+1):(length(mod_1)+length(mod_2)))
  }
}
##Mean shape module
meansh.use <- "n"
meansh.use <- readline(prompt = "Do you wish to use the sample mean shape
    for the alignment? Type 'y' or 'n'.")
if (meansh.use == "y"){
  print("Using consensus landmark configuration.")
  sample.mean <- gpagen(sample_dta)
  sample.mean <- sample.mean$consensus
  for (n in 1:length(sample.data)){
    sample_dta[,,n] <- sample.mean
  }
}
print("Running digital alignment tool (DTA) by Profico et al (2019).")
sample_dta <- provideDimnames(sample_dta, base = list("v", "c", "s"))
    #Assigning generic names to specimens as a workaround
ex.dta <- dta(RM_sample = sample_dta, mod_1 = mod_1, mod_2 = mod_2,
    pairs_1 = pairs_1, pairs_2 = pairs_2, DM_mesh_1 = Amesh, DM_mesh_2 =
    Bmeshes[[b]], DM_set_1 = target_dta[mod_1,], DM_set_2 =
    target_dta[mod_2,])
#Print the name of the best reference model
if (meansh.use != "y"){
  print("The best reference model for this alignment is:")
  print(names(sample.data[((as.numeric(gsub("s", "", ex.dta$AM_id)))
      +1)])) #Missing names workaround
}
#Save alignment data.
write.csv(alignset, paste0("./Results/alignset_", b, "_", phase, ".csv"),
    row.names = FALSE) #Save 'alignset' to *.csv file.
alsets <- append(alsets, paste0("./Results/alignset_", b, "_", phase,
    ".csv"))
mesh2ply(ex.dta$AM_mesh, paste0("./Results/alignment_", b, "_", phase))
aligned.meshes <- append(aligned.meshes, paste0("./Results/alignment_",
    b, "_", phase, ".ply"))
sink(paste0("./Results/alignment_", b, "_", phase, ".TPS")) #Save aligned
    matrix to TPS file.
if (semiland.use == "y"){
  cat(paste0("LM3=", (length(alignset) + watanabe)))
} else {
```

```
    cat(paste0("LM3=", length(alignset)))
  }
  cat("\n")
  cat(write.table(ex.dta$AM_set, row.names=F, col.names=F, sep="\t"))
  cat(paste0("ID=alignment_", b))
  cat("\n")
  cat("\n")
  sink()
  AMlms <- append(AMlms, paste0("./Results/alignment_", b, "_", phase,
      ".TPS"))
  #Plot the aligned 3D model.
  open3d()
  wire3d(ex.dta$AM_mesh, col="#6e6eff")
  plot3D(ex.dta$AM_set, col="#ff5050", bbox=FALSE, add=TRUE)
  print(paste0("This alignment is plotted in RGL device no. ", .check3d(),
      "."))
}
#Choose an aligned model
if (phase == (length(target.data) -1)){
  finalset <- read.csv(alsets[length(alsets)])
  finalset <- finalset$x
  complete <- array(dim = c(length(finalset), length(ex.dta$AM_set[1,]), 1))
  if (semiland.use == "y"){
    finalsemi <- append(1:(length(finalset) - length(mod_2)), mod_2) #Get
        rid of surface semilandmarks again.
    for (i in 1:length(complete[,,1][,1])){
      complete[,,1][finalset[i],] <- ex.dta$AM_set[finalsemi[i],]
    }
  } else {
    for (i in 1:length(complete[,,1][,1])){
      complete[,,1][finalset[i],] <- ex.dta$AM_set[i,]
    }
  }
  ###Write a .PP file to check if the AM_set is in the same atlas as the
      AM_mesh
  write.pp(complete[,,1], "./Results/complete.pp")
  stop("Alignment complete.", call. = FALSE)
} else {
  a <- NULL
  choice <- as.numeric(readline(prompt = "Choose the best aligned model
      (AM) by typing in the corresponding sequence number."))
  chosenAMset <- c(read.csv(alsets[choice]))
  a <- readland.tps(AMlms[choice], specID = "ID")
  a <- a[,,1]
  if (semiland.use == "y"){ #Get rid of the semilandmarks.
    a.wo.semi <- rbind(a[aset,], a[(length(aset) + watanabe +
        1):length(a[,1]),])
    a <- a.wo.semi
  }
  Amesh <- file2mesh(aligned.meshes[choice])
```

```
      assembly.order <- assembly.order[-choice]
      Bmeshes <- Bmeshes[-choice]
      target_ordr <- target_ordr[,,-choice]
      phase = phase +1
    }
  }
}
```

Appendix C

Bottlenose.R

```
print("Executing testing script.")
print("This script will test the effect of the selected active module(s) on a
    sample of specimens.")
print("Please activate the desired module(s) by typing 'y' or 'n'.")

#Module activation
meansh.use <- "n"
meansh.use <- readline(prompt = "Mean shape module:")
symmetrical.use <- "n"
symmetrical.use <- readline(prompt = "Symmetry module:")
semiland.use <- "n"
semiland.use <- readline(prompt = "Semilandmarks module:")

#Test
mn.disp <- NULL
symm.patt <- NULL
sample.meshes <- NULL
meshes.bkup <- NULL
for (g in 1:length(sample.data)){
  sample.bkup <- sample
  data.bkup <- sample.data
  #DTA loop.
  complete <- NULL
  is.complete <- NULL
  use.complete <- "n"
  is.complete <- 1
  if (length(is.complete) > 0){
    use.complete <- "y"
    if (use.complete == "y") {
      complete <- sample[,,g]
    }
  }
  sample <- sample[,,-g]
  sample.data <- sample.data[-g]
  target.meshes <- file2mesh("C:/Users/Gustavo/3D Objects/KNMER1813.ply")
  ##Tell R in which order to assemble the fragments and what to use.
```

```
assembly.order = 1:length(target.data)
first <- 2 #as.numeric(readline(prompt = "Select a fragment to begin the
    alignment by typing in the corresponding number."))
print("Selected fragment is fixed to 2.")
assembly.order <- assembly.order[-first]
target_ordr <- array(dim = c(length(target.data[[1]][,1]),
    length(target.data[[1]][1,]), length(assembly.order)))
for (i in 1:length(assembly.order)){
  target_ordr[,,i] <- target[,,(assembly.order[i])]
}
a <- array(dim = c(length(target.data[[1]][,1]),
    length(target.data[[1]][1,]), 1))
a <- target[,,first]
Amesh <- target.meshes
##Create some empty vectors for later.
bestrms <- NULL
dtasamples <- NULL
aligned.meshes <- NULL
AMlms <- NULL
phase = 1
alsets <- NULL
###Loop start.
for (b in 1:length(assembly.order)){
  Asurf <- NULL
  if (is.null(meshes.bkup) == FALSE){
    sample.meshes <- meshes.bkup
  }
  print("---")
  print(paste0("Aligning fragment no. ", b, " of ", length(assembly.order),
      " with the selected fragment (specimen ", g, ")."))
  #Define the landmarks belonging to the first and second model.
  if (phase == (length(target.data) -1)){
    bset <- which(complete.cases(target_ordr) == TRUE)
    if (is.null(complete) == FALSE){
      blms <- array(dim = c(length(complete[,1]), length(complete[1,]), 1))
      for (i in 1:length(blms[,,1][,1])){
        blms[,,1][i,] <- complete[i,]
      }
      blms <- blms[,,1]
    } else {
      blms <- target_ordr
    }
  } else {
    bset <- which(complete.cases(target_ordr[,,b]) == TRUE)
    if (is.null(complete) == FALSE){
      blms <- array(dim = c(length(complete[,1]), length(complete[1,]), 1))
      for (i in 1:length(blms[,,1][,1])){
        blms[,,1][i,] <- complete[i,]
      }
      blms <- blms[,,1]
```

```
  } else {
    blms <- target_ordr[,,b]
  }
}
if (phase == 1){
  alignset <- append(which(complete.cases(a) == TRUE), bset)
  mod_1 <- c(1:length(which(complete.cases(a) == TRUE)))
  mod_2 <- c((length(which(complete.cases(a) == TRUE))+1):length(alignset))
} else {
  alignset <- append(chosenAMset$x, bset)
  mod_1 <- c(1:length(chosenAMset$x))
  mod_2 <- c((length(chosenAMset$x)+1):length(alignset))
}
##Create a new data subset for the DTA.
###Prepare target data set.
if (phase == 1){
  if (is.null(complete) == FALSE){
    target_dta <- rbind(blms[which(complete.cases(a) == TRUE),],
       blms[bset,])
  } else {
    target_dta <- rbind(a[which(complete.cases(a) == TRUE),], blms[bset,])
  }
} else {
  target_dta <- rbind(a, blms[bset,])
}
sample_dta <- array(dim = c(length(alignset), length(sample[,,1][1,]),
    length(sample.data)))
for (n in 1:length(sample.data)){
  sample_dta[,,n] <- sample[,,n][alignset,]
}
##Symmetry module
pairs_1 = NULL #Set pair list default values to NULL.
pairs_2 = NULL
if (symmetrical.use == "y"){
  print("Symmetry module active.")
  if (is.null(symm.patt)){
    symm.patt <- list(c(1, 2))
    symm.patt[[1]] <- readline(prompt = "Please enter the characters used
       to distinguish left bilateral landmarks. For example, '_L'.")
    symm.patt[[2]] <- readline(prompt = "Please enter the characters used
       to distinguish right bilateral landmarks. For example, '_R'.")
  }
  symmlmsL.names <- grep(paste0("*", symm.patt[[1]]), varname[[1]], value =
     TRUE) #Get the names of all the left bilateral landmarks that were
     retained in the sample set.
  symmlmsL.names <- gsub("_L", "", symmlmsL.names) #Delete the "left" part
     of their names.
  symmlmsR = 0 #Create a new empty right bilateral landmark list.
  symmlmsR.names = 0
  for (i in 1:length(symmlmsL.names)){
```

```
    symmlmsR <- append(symmlmsR, grep(paste0(symmlmsL.names[i],
        symm.patt[[2]]), varname[[1]])) #Search which of the landmarks
        retained in the sample are the corresponding right bilateral
        landmarks for the left bilateral landmarks in the first list.
    symmlmsR.names <- append(symmlmsR.names, grep(paste0(symmlmsL.names[i],
        symm.patt[[2]]), varname[[1]], value = TRUE)) #Get their names.
  }
  symmlmsR.names <- gsub(symm.patt[[2]], "", symmlmsR.names) #Delete the
      "right" part of their names.
  symmlmsR <- symmlmsR[-1] #Get rid of the zeros.
  symmlmsR.names <- symmlmsR.names[-1]
  symmlmsR2L = 0
  symmlmsL.names <- grep(paste0("*", symm.patt[[1]]), varname[[1]], value =
      TRUE) #Put the "left" part of the names of the left bilateral
      landmarks back in the list.
  for (i in 1:length(symmlmsR.names)){
    symmlmsR2L <- append(symmlmsR2L, grep(symmlmsR.names[i],
        symmlmsL.names, value = TRUE)) #Keep only the left bilateral
        landmark names that have a corresponding right bilateral landmark
        in the second list.
  }
  symmlmsR2L <- symmlmsR2L[-1]
  symmlmsL = 0 #Create a new empty left bilateral landmark list.
  for (i in 1:length(symmlmsR2L)){
    symmlmsL <- append(symmlmsL, grep(paste0(symmlmsR2L[i]), varname[[1]]))
  }
  symmlmsL <- symmlmsL[-1]
  symmlms <- cbind(symmlmsL, symmlmsR)
  if ((length(symmlms) != 0) == TRUE){
    for (r in 1:length(symmlms[,1])){
      if (all(symmlms[r,] %in% mod_1) == TRUE){
        pairs_1 <- rbind(pairs_1, symmlms[r,])
      }
    }
    for (r in 1:length(symmlms[,1])){
      if (all(symmlms[r,] %in% mod_2) == TRUE){
        pairs_2 <- rbind(pairs_2, symmlms[r,])
      }
    }
  }
}
##Semilandmarks module.
if (use.complete == "y"){
  if (semiland.use == "y"){
    print("Semilandmarks module active.")
    if (symmetrical.use == "y"){
      print("Warning: Symmetry constrains will not apply to surface
          semilandmarks.")
    }
```

```
###Load the sample mesh files. Pro tip: Name the 3D model files the
    same as their corresponding Meshlab picked points files.
if (is.null(sample.meshes)){
  print("You will need to provide 3D mesh files for all of the sample
      specimens.")
  sampleplys <- list.files(path = choose.dir(caption = "Choose the
      directory where the surface 3D meshes of the sample specimens are
      stored."), pattern = "*.ply", full.names = TRUE)
  sample.meshes <- lapply(sampleplys, file2mesh)
  meshes.bkup <- sample.meshes
}
###Load a surface mesh.
print("A surface mesh is required to apply semilandmarks. Please,
    prepare and locate the file corresponding to the surface mesh of
    the selected fragment or alignment.")
if (is.null(Asurf)){
  Asurf <- sample.meshes[[g]]
} else if (phase > 1) {
  print("Warning: The landmark data set may no longer be mapped to the
      surface mesh. Every time an alignment is accepted, a new surface
      mesh is required to apply semilandmarks.")
  print("A .PP file of the accepted alignment has been created to
      verify that the landmarks are correctly mapped to the chosen
      previous phase alignment mesh. Delete this file after use!")
  ###Write a .PP file to check if the AM_set is in the same atlas as
      the AM_mesh
  write.pp(target_dta, "./Results/accepted.pp")
  Asurf <- file2mesh(choose.files(caption = "Select a surface mesh."))
}
sample.meshes <- sample.meshes[-g]
#print("Determining minimal amount of surface semilandmarks.")
watanabe = 100 ###ADD LASEC FUNCTION
print("Creating template.")
target.surf <- buildtemplate(spec = Asurf, fixed = target_dta, center =
    FALSE, surface.sliders = watanabe)
target.nts <- readland.nts("./Asurf.nts")
target.surf <- array(dim = c((length(alignset) + watanabe),
    length(sample.data[[1]][1,]), 1))
for (k in 1:(length(alignset) + watanabe)){
  target.surf[,,1][k,] <- target.nts[,,k]
}
###Divide the semilandmark set
target.surA <- target.surf[,,1][mod_1,]
target.surB <- target.surf[,,1][mod_2,]
target.surC <- target.surf[,,1][((length(alignset)
    +1):(length(alignset) + watanabe)),]
###Rearrange the landmarks
target.semi <- rbind(target.surA, target.surC)
target.semi <- rbind(target.semi, target.surB)
target_dta <- target.semi
```

```
    sample.semi <- array(dim = c((length(alignset) + watanabe),
       length(sample.data[[1]][1,]), length(sample.data)))
    print("Applying semilandmarks.")
    for (n in 1:length(sample.data)){
      Bsurf <- sample.meshes[[n]]
      sample.surf <- digitsurface(spec = Bsurf, fixed = sample_dta[,,n],
         center = FALSE)
      sample.nts <- readland.nts("./Bsurf.nts")
      sample.surf <- array(dim = c((length(alignset) + watanabe),
         length(sample.data[[1]][1,]), 1))
      for (k in 1:(length(alignset) + watanabe)){
        sample.surf[,,1][k,] <- sample.nts[,k]
      }
      sample.surA <- sample.surf[,,1][mod_1,]
      sample.surB <- sample.surf[,,1][mod_2,]
      sample.surC <- sample.surf[,,1][((length(alignset)
         +1):(length(alignset) + watanabe)),]
      sample.surD <- rbind(sample.surA, sample.surC)
      sample.surD <- rbind(sample.surD, sample.surB)
      sample.semi[,,n] <- sample.surD
    }
    sample_dta <- sample.semi
    aset <- mod_1 #Save original 'mod_1'.
    mod_1 <- c(1:(length(mod_1) + watanabe))
    mod_2 <- c((length(mod_1)+1):(length(mod_1)+length(mod_2)))
  }
}
##Mean shape module
if (meansh.use == "y"){
  print("Using consensus landmark configuration.")
  sample.mean <- gpagen(sample_dta)
  sample.mean <- sample.mean$consensus
  for (n in 1:length(sample.data)){
    sample_dta[,,n] <- sample.mean
  }
}
print("Running digital alignment tool (DTA) by Profico et al (2019).")
#sample_dta <- provideDimnames(sample_dta, base = list("v", "c", "s"))
    #Assigning generic names to specimens as a workaround
ex.dta <- dta(RM_sample = sample_dta, mod_1 = mod_1, mod_2 = mod_2,
    pairs_1 = pairs_1, pairs_2 = pairs_2, DM_mesh_1 = Amesh, DM_mesh_2 =
    Amesh, DM_set_1 = target_dta[mod_1,], DM_set_2 = target_dta[mod_2,])
#Plot the "reconstructed" landmarks
#plot3D(ex.dta$AM_set, size = 4)
#Print the name of the best reference model
if (meansh.use != "y"){
  print("The best reference model for this alignment is:")
  print(names(sample.data[((as.numeric(gsub("s", "", ex.dta$AM_id))) +1)]))
      #Missing names workaround
}
```

```
    #Save alignment data.
    test.data <- array(dim = c(length(ex.dta$AM_set[,1]),
        length(ex.dta$AM_set[1,]), 2))
    test.data[,,1] <- ex.dta$AM_set
    test.data[,,2] <- target_dta
    test.data <- ProcGPA(test.data, scale = FALSE)
    test.data <- test.data$rotated
    displacement <- NULL
    for (l in 1:length(test.data[,,1][,1])){
      lmdist = sqrt(((test.data[,,2][l,1] - test.data[,,1][l,1])^2) +
          ((test.data[,,2][l,2] - test.data[,,1][l,2])^2) +
          ((test.data[,,2][l,3] - test.data[,,1][l,3])^2))
      displacement <- append(displacement, lmdist)
    }
    mn.disp <- append(mn.disp, mean(displacement))
  }
  sample <- sample.bkup
  sample.data <- data.bkup
}
omn.disp <- NULL
fmn.disp <- NULL
for (i in seq(1, length(mn.disp), 2)){
  omn.disp <- append(omn.disp, as.numeric(mn.disp[i]))
}
for (j in seq(2, length(mn.disp), 2)){
  fmn.disp <- append(fmn.disp, as.numeric(mn.disp[j]))
}
plot(omn.disp, ylim = c(0, 3), main = "Restoration Error", xlab = "", ylab =
    "Mean landmark displacement (Euclidean distance)", type = "l", las = 2)
axis(1, at = 1:length(omn.disp), labels = names(sample.data), las = 2)
ready <- readline(prompt = "Press [enter] for next plot")
plot(fmn.disp, ylim = c(0, 1), main = "Restoration Error", xlab = "", ylab =
    "Mean landmark displacement (Euclidean distance)", type = "l", las = 2)
axis(1, at = 1:length(fmn.disp), labels = names(sample.data), las = 2)
meanerror <- mean(mn.disp)
omeanerror <- mean(omn.disp)
fmeanerror <- mean(fmn.disp)
print("Restoration of fragment No. 1. Landmark displacement (Euclidean
    distance) between Procrustes superimposed original and reconstructed
    configurations.")
print(omn.disp)
print(paste0("Mean error for fragment No. 1 is ", omeanerror))
print("Restoration of fragment No. 2. Landmark displacement (Euclidean
    distance) between Procrustes superimposed original and reconstructed
    configurations.")
print(fmn.disp)
print(paste0("Mean error for fragment No. 2 is ", fmeanerror))
print(paste0("Mean error for this module configuration is ", meanerror))
```